The Astrophysical Journal, 941:106 (27pp), 2022 December 20 https://doi.org/10.3847/1538-4357/ac9626

The X–shooter/ALMA Sample of Quasars in the Epoch of Reionization. II. Black Hole Masses, Eddington Ratios, and the Formation of the First Quasars

Emanuele Paolo Farina[1,2,3], Jan-Torge Schindler[2,4], Fabian Walter[2], Eduardo Bañados[2], Frederick B. Davies[2], Roberto Decarli[5], Anna-Christina Eilers[6,19], Xiaohui Fan[7], Joseph F. Hennawi[4,8], Chiara Mazzucchelli[9,10], Romain A. Meyer[2], Benny Trakhtenbrot[11], Marta Volonteri[12], Feige Wang[7,19], Gábor Worseck[13], Jinyi Yang[7,20], Thales A. Gutcke[14,19], Bram P. Venemans[4], Sarah E. I. Bosman[2], Tiago Costa[3], Gisella De Rosa[15], Alyssa B. Drake[2,16], and Masafusa Onoue[2,17,18]

[1] Gemini Observatory, NSF's NOIRLab, 670 N A'ohoku Place, HI-96720, Hilo, HI, USA; emanuele.paolo.farina@gmail.com
[2] Max Planck Institut für Astronomie, Königstuhl 17, D-69117, Heidelberg, Germany
[3] Max Planck Institut für Astrophysik, Karl–Schwarzschild–Straße 1, D-85748, Garching bei München, Germany
[4] Leiden Observatory, Leiden University, Niels Bohrweg 2, NL-2333 CA Leiden, The Netherlands
[5] INAF—Osservatorio di Astrofisica e Scienza dello Spazio di Bologna, via Gobetti 93/3, I-40129, Bologna, Italy
[6] MIT Kavli Institute for Astrophysics and Space Research, 77 Massachusetts Avenue, Cambridge, MA 02139, USA
[7] Steward Observatory, University of Arizona, 933 N Cherry Avenue, Tucson, AZ 85721, USA
[8] Department of Physics, University of California, Santa Barbara, CA 93106-9530, USA
[9] European Southern Observatory, Alonso de Córdova 3107, Vitacura, Región Metropolitana, Chile
[10] Núcleo de Astronomía de la Facultad de Ingeniería, Universidad Diego Portales, Av. Ejército Libertador 441, Santiago, Chile
[11] School of Physics and Astronomy, Tel Aviv University, Tel Aviv, 69978, Israel
[12] Institut d'Astrophysique de Paris, Sorbonne Université, CNRS, UMR 7095, 98 bis bd Arago, F-75014, Paris, France
[13] Institut für Physik und Astronomie, Universität Potsdam, Karl-Liebknecht-Str. 24/25, D-14476 Potsdam, Germany
[14] Department of Astrophysical Sciences, Princeton University, Peyton Hall, Princeton, NJ 08544, USA
[15] Space Telescope Science Institute, 3700 San Martin Drive, Baltimore, MD 21218, USA
[16] Centre for Astrophysics Research, Department of Physics, Astronomy and Mathematics, University of Hertfordshire, Hatfield AL10 9AB, UK
[17] Kavli Institute for Astronomy and Astrophysics, Peking University, Beijing 100871, People's Republic of China
[18] Kavli Institute for the Physics and Mathematics of the Universe (Kavli IPMU, WPI), The University of Tokyo, Chiba 277-8583, Japan
Received 2022 June 8; revised 2022 September 8; accepted 2022 September 14; published 2022 December 15

Abstract

We present measurements of black hole masses and Eddington ratios ($\lambda_{\rm Edd}$) for a sample of 38 bright ($M_{1450} < -24.4$ mag) quasars at $5.8 \lesssim z \lesssim 7.5$, derived from Very Large Telescope/X–shooter near–IR spectroscopy of their broad C IV and Mg II emission lines. The black hole masses (on average, $M_{\rm BH} \sim 4.6 \times 10^9\,M_\odot$) and accretion rates ($0.1 \lesssim \lambda_{\rm Edd} \lesssim 1.0$) are broadly consistent with that of similarly luminous $0.3 \lesssim z \lesssim 2.3$ quasars, but there is evidence for a mild increase in the Eddington ratio above $z \gtrsim 6$. Combined with deep Atacama Large Millimeter/submillimeter Array (ALMA) observations of the [C II] 158 μm line from the host galaxies and VLT/MUSE investigations of the extended Lyα halos, this study provides fundamental clues to models of the formation and growth of the first massive galaxies and black holes. Compared to local scaling relations, $z \gtrsim 5.7$ black holes appear to be over-massive relative to their hosts, with accretion properties that do not change with host galaxy morphologies. Assuming that the kinematics of the $T \sim 10^4$ K gas, traced by the extended Lyα halos, are dominated by the gravitational potential of the dark matter halo, we observe a similar relation between black hole mass and circular velocity as reported for $z \sim 0$ galaxies. These results paint a picture where the first supermassive black holes reside in massive halos at $z \gtrsim 6$ and lead the first stages of galaxy formation by rapidly growing in mass with a duty cycle of order unity. The duty cycle needs to drastically drop toward lower redshifts, while the host galaxies continue forming stars at a rate of hundreds of solar masses per year, sustained by the large reservoirs of cool gas surrounding them.

Unified Astronomy Thesaurus concepts: Quasars (1319); Reionization (1383); Supermassive black holes (1663)

Supporting material: machine-readable table

1. Introduction

One year after the first identification of a quasar at high redshift (3C 273 at $z = 0.158$; Schmidt 1963), it was already clear that the observed luminosities (and variability timescales) require the presence of a supermassive black hole (SMBH) located at the center of the galaxy (Salpeter 1964; Zel'dovich & Novikov 1964). This argument was refined a few years later by Lynden-Bell (1969). It is now well established that virtually all massive galaxies in the (local) universe host an SMBH (e.g., Kormendy & Richstone 1995; Richstone et al. 1998; Kormendy & Gebhardt 2001; Kormendy & Ho 2013). If, during an active phase, a fraction of their energy and/or momentum output couples with the gas in the galaxy, the SMBHs will affect both their own growth and the star formation history of their hosts, at scales much larger than the black hole sphere of influence (e.g., Silk & Rees 1998; Di Matteo et al. 2005). This coevolutionary scenario is supported by the observed correlations between the mass of the black hole and host properties such as mass/luminosity

[19] NASA Hubble Fellow.
[20] Strittmatter Fellow.

(e.g., Dressler 1989; McLure & Dunlop 2002; Marconi & Hunt 2003; Häring & Rix 2004; McConnell & Ma 2013), velocity dispersion (e.g., Ferrarese & Merritt 2000; Gebhardt et al. 2000; Tremaine et al. 2002), and even with the circular velocity or dynamical mass of the dark matter halo (e.g., Ferrarese 2002; Volonteri et al. 2011). (The interested reader can refer to Kormendy & Ho 2013 for a review on the different correlations and to Jahnke & Macciò 2011 for concerns on correlations versus causation.)

Intriguingly, some of these correlations evolve with cosmic time (but see, e.g., Shen et al. 2015; Suh et al. 2020). In particular, the mass ratios between black holes and host galaxies and that between black holes and bulges increase with redshift, potentially following different evolutionary paths (e.g., Kormendy & Ho 2013; Ding et al. 2020). Albeit biases in the study of flux-limited samples can contribute to the observed evolution (e.g., Lauer et al. 2007; Schulze & Wisotzki 2011, 2014; Izumi et al. 2021), black holes at higher redshift are generally more massive with respect to their host than they are in the local universe (e.g., Walter et al. 2004; Peng et al. 2006; Decarli et al. 2010a, 2010b; Merloni et al. 2010; Bennert et al. 2011; Targett et al. 2012; Trakhtenbrot et al. 2015; Venemans et al. 2016; Willott et al. 2017; Pensabene et al. 2020; Neeleman et al. 2021). This suggests that, in the initial stages, black holes may have dominated the symbiotic evolution with their host galaxies (see Volonteri 2012, for a review on the topic). A detailed characterization of the general physical properties of the first quasars is thus fundamental to shedding light on massive galaxy formation in the early universe.

Recent years have seen a surge in the number of quasars known at $z > 5.5$ (e.g., Fan et al. 2001, 2003, 2006; Venemans et al. 2007, 2013; Willott et al. 2007, 2010a; Mortlock et al. 2011; Wu et al. 2015; Bañados et al. 2016, 2019; Jiang et al. 2016; Matsuoka et al. 2016, 2018a, 2019, 2022; Mazzucchelli et al. 2017; Pons et al. 2019; Reed et al. 2019; Yang et al. 2019a; Wang et al. 2020a, 2021a; Onoue et al. 2021; Wenzl et al. 2021; Wagenveld et al. 2022). This large sample opens a new era for statistical studies of the population of SMBHs emerging from the reionization epoch.

Deep near-IR spectroscopy campaigns revealed that, already at $z > 7$, luminous quasars are powered by massive black holes (with $\sim 10^9\,M_\odot$; Bañados et al. 2018b; Yang et al. 2020; Wang et al. 2021a) with metal-enriched (solar metallicity) broad-line regions (BLRs; e.g., Onoue et al. 2020; Yang et al. 2021, see also Wang et al. 2021b; Lai et al. 2022). Furthermore, there is no apparent redshift evolution in the continuum slope or in the shape of low-ionization broad emission lines at this redshift when comparing the composite spectra of typical Sloan Digital Sky Survey (SDSS) quasars (at $0.04 < z < 4.79$; Vanden Berk et al. 2001) to bright $z \sim 6$ quasars (Shen et al. 2019; Yang et al. 2021). This suggests that, to first order, the same physical mechanisms are powering the quasar emission at different redshifts. Yet, the observed increase in the average blueshift of the C IV–Mg II velocity difference (e.g., Venemans et al. 2016; Mazzucchelli et al. 2017; Meyer et al. 2019; Schindler et al. 2020; Yang et al. 2021) and in the fraction of broad absorption lines (BAL; e.g., Yang et al. 2021; Bischetti et al. 2022) and weak line quasars (e.g., Shen et al. 2019) may imply, barring selection effects, a change in the BLR's physical status and/or that strong outflows may have a more relevant role toward the highest redshifts.

Despite our expansion in knowledge about the SMBHs powering the first quasars, still little is known about the rest-frame UV emission of their host galaxies. Indeed, given the extreme brightness of the quasar emission at these wavelengths, the detection of the stellar component has proven to be prohibitive with large aperture ground-based telescopes (e.g., Targett et al. 2012) and even with HST (e.g., Mechtley et al. 2012; Marshall et al. 2020a). On the other hand, the interstellar medium (ISM) of tens of quasar host galaxies has been detected at millimeter-wavelengths in the dust continuum and in the [C II] 158 μm emission line (e.g., Wang et al. 2016b, 2019c; Decarli et al. 2017, 2018; Venemans et al. 2018; Wang et al. 2019a; Rojas-Ruiz et al. 2021; Khusanova et al. 2022) and, in some cases, also in the [O III] 88 μm, [O I] 146 μm, [C I] 369 μm, CO, and water lines (e.g., Wang et al. 2011a, 2011b, 2016b; Venemans et al. 2017a; Walter et al. 2018; Novak et al. 2019; Shao et al. 2019; Yang et al. 2019b; Wang et al. 2019a; Pensabene et al. 2021; Decarli et al. 2022; Li et al. 2022; Meyer et al. 2022a; Pensabene et al. 2022). In particular, Atacama Large Millimeter/submillimeter Array (ALMA) [C II] 158 μm observations at a resolution of $\lesssim$1 kpc are providing detailed information on star formation rates, the presence of molecular outflows, dynamical masses, and morphology of early massive galaxies hosting SMBHs (Venemans et al. 2019, 2020; Novak et al. 2020; Neeleman et al. 2021; Walter et al. 2022).

To investigate the link between SMBHs and their hosts at $z \gtrsim 6$, we thus started a VLT/X–shooter program targeting quasars already observed with ALMA. The first results from this program were presented in Schindler et al. (2020, hereafter Paper I), in which we introduced the sample of 38 $5.78 < z < 7.54$ quasars and analyzed the properties of their broad emission lines. To summarize, the main results of Paper I are: (i) the BLR of early quasars is already enriched, with iron at levels comparable to lower-redshift systems; (ii) both the Mg II and the C IV emission lines are blueshifted with respect to the host galaxy systemic redshift (traced by the [C II] 158 μm emission line); (iii) these Mg II and the C IV blueshifts strongly correlate with each other, implying a common physical origin of the velocity displacement; and (iv) the median velocity blueshift between C IV and Mg II broad lines is increased by a factor $\sim$2.3$\times$ with respect to similarly luminous quasars at lower redshifts.

In this paper, we will focus on black hole masses and accretion rates and connect these with the host galaxy properties (see also, Neeleman et al. 2021). In addition, we will link the characteristics of the first SMBHs with their large-scale ($\gtrsim$10 kpc) cool gas reservoirs probed by VLT/MUSE observations of the extended Lyα nebulae surrounding them (namely, the REQUIEM survey; Farina et al. 2019). These halos show quiescent kinematics and contain a sufficient supply of cool gas ($>10^9\,M_\odot$) to fuel the future star formation and black hole mass growth (e.g., Farina et al. 2019; Drake et al. 2022). By linking the SMBHs with the ISM properties of their hosts and with the cool gas in the circumgalactic medium (CGM), this study aims to provide a comprehensive view of massive galaxy formation at the epoch of reionization.

Throughout this paper, we assume a concordance cosmology with $H_0 = 70\,\mathrm{km\,s^{-1}\,Mpc^{-1}}$, $\Omega_\mathrm{M} = 0.3$, and $\Omega_\Lambda = 1 - \Omega_\mathrm{M} = 0.7$, in broad agreement with the Planck cosmological parameters (Planck Collaboration et al. 2020). In this cosmology, at $z = 6.3$ (the average redshift of our sample), the universe is 0.859 Gyr old, and an angular scale $\theta = 1''$ corresponds to a proper transverse

separation of 5.6 kpc. All quoted magnitudes are in the standard AB photometric system (Oke 1974; Oke & Gunn 1983).

2. Sample

Our sample consists of 38 bright quasars in the redshift range $5.78 < z < 7.54$ with an average redshift of $\langle z \rangle = 6.3$ (see Table 1 and Figure 1). For all quasars in our sample we will report *systemic* redshifts ($z_{\rm sys}$), mainly derived from the [C II] 158 μm emission from the host galaxy. Wherever this line has not been detected, we consider as *systemic* the redshift of the extended Lyα emission or of the Mg II line. These are considered good tracers of systemic redshifts, with an average displacement between the Lyα halo and the [C II] 158 μm redshifts of $\sim$70 km s^{-1} (Farina et al. 2019) and between the Mg II and the [O III] redshifts of roughly -100 km s^{-1} (Richards et al. 2002; Hewett & Wild 2010).

The absolute magnitudes of the considered quasars vary from $M_{1450} = -24.4$ mag to -29.0 mag (see Table 1 and Figure 1). For comparison, current constraints on the $z \gtrsim 6$ quasar luminosity function suggest a characteristic magnitude of $M^{\star}_{1450} \sim -25.2$ mag (e.g., Willott et al. 2010a; Kashikawa et al. 2015; Jiang et al. 2016; Matsuoka et al. 2018b; Wang et al. 2019b; see Kulkarni et al. 2019 and Shen et al. 2020 for an extensive discussion on the evolution of the quasar luminosity function at high redshift). This is a factor of $\sim$4$\times$ fainter than the average absolute magnitude of our sample: $\langle M_{1450} \rangle = -26.8$ mag. The considered targets are, thus, sampling the bright end of the highest-redshift quasar population.

Eight out of the 38 objects in our sample are classified as BAL quasars (i.e., P009−10, P065−26, J1044−0125, P239−07, J2211−3206, J2310+1855, J2318−3029, and J2348−3054; see De Rosa et al. 2014; Shen et al. 2019; Eilers et al. 2020; Bischetti et al. 2022; Paper I). The fraction of BAL quasars in our sample (21^{+10}_{-7}%) is higher, but nevertheless consistent, with the incidence of such systems reported in lower-redshift studies. Indeed, the fraction of bright ($M_i[z = 2] < -27$ mag, corresponding to $M_{1450} \lesssim 25.3$ mag) BAL quasars in the 14th data release of the SDSS quasar catalog is $\sim$12% (Pâris et al. 2018; see also, e.g., Maddox et al. 2008; Knigge et al. 2008; Allen et al. 2011).

3. Observations, Data Reduction, and Fitting Procedure

We refer the interested reader to Paper I for an exhaustive description of the data collection and reduction, and of the quasar fitting procedure. For the sake of completeness, we provide a brief summary of the followed steps in the next sections.

3.1. Observations

Near-IR spectra of the quasars in our sample were collected with the medium-resolution spectrograph X–shooter (Vernet et al. 2011), currently mounted on the Cassegrain focus of the ESO/VLT Telescope Melipal. Observations were taken with the 0.″6, 0.″9, or 1.″2 slit (delivering a resolution $R = \lambda/\Delta\lambda \sim$ 8100–4300 in the near-IR) and following the typical ABBA or ABAB dither pattern. Exposure times range from 40 minutes to 22.3 hr per target, with a median of 2 hr (see Table 1 in Paper I, for further details).

The data was collected as part of the following observing programs: 60.A-9418(A, PI: Ryan–Weber), 084.A-0360(A, PI: Hjorth), 084.A-0390(A, PI: Ryan–Weber), 085.A-0299(A, PI: D'Odorico), 086.A-0162(A, PI: D'Odorico), 087.A-0890(A, PI: De Rosa), 088.A-0897(A, PI: De Rosa), 089.A-0814(A, PI: Becker), 091.C-0934(B, PI: Kaper), 093.A-0707(A, PI: Becker), 096.A-0095(A, PI: Pettini), 096.A-0418(A, PI: Shanks), 096.A-0418(B, PI: Shanks), 097.B-1070(A, PI: Farina), 098.B-0537(A, PI: Farina), 0100.A-0625(A, PI: D'Odorico), 0100.A-0898(A, PI: Venemans), 0101.B-0272(A, PI: Eilers), 0102.A-0154(A, PI: D'Odorico), and 286.A-5025(A, PI: Venemans).

3.2. Data Reduction

The data reduction was performed with the open-source software PYPEIT (Prochaska et al. 2019a, 2019b, 2020) following standard procedures for near-IR spectroscopy:

1. single exposures are corrected for instrumental signatures (e.g., flat-field);
2. the wavelength solution for each exposure is obtained by comparing the sky-spectrum with the location, in vacuum, of OH (from Rousselot et al. 2000) and water lines;[21]
3. cosmic rays are removed with the L. A. COSMIC algorithm (van Dokkum 2001);
4. sky subtraction is performed on the 2D images both by differencing the AB exposures and by iteratively removing residuals with a 2D b-spline fit that follows the curvature of the spectral features (e.g., Kelson 2003);
5. the quasar's trace is automatically detected and optimally extracted (Horne 1986);
6. single 1D spectra are flux calibrated using X–shooter standard stars[22] (Moehler et al. 2014);
7. all 1D flux-calibrated spectra of each object are combined, after re-scaling them to the same flux level;
8. telluric absorption features are removed from the stacked spectrum using telluric grids created from the LINE-BY-LINE RADIATIVE TRANSFER MODEL (Clough et al. 2005, 2014) and a principal component analysis model of the quasar emission (Davies et al. 2018);
9. absolute flux calibration is reached by re-scaling the spectrum to the published *J*- (or *K*-) band magnitude of the objects (see Table 1).

The reduced spectra have a median signal-to-noise ratio (S/N) per pixel in the *J* band of S/N $\sim$ 6.

3.3. Fit of the Spectra

To characterize the C IV ($\lambda_{\rm rest} = 1549.06$ Å) and Mg II ($\lambda_{\rm rest} = 2798.75$ Å) broad emission-line properties of our quasars, we followed the standard procedure of fitting the spectra of high-redshift quasars with a global continuum plus a model of the emission lines (e.g., De Rosa et al. 2014; Mazzucchelli et al. 2017; Shen et al. 2019; Onoue et al. 2020; Yang et al. 2021; Paper I). The fitting procedure was handled using the PYTHON package SCULPTOR (Schindler 2022) after binning each spectrum by a factor of 4 in wavelength.

[21] https://hitran.org/

[22] https://www.eso.org/sci/facilities/paranal/instruments/xshooter/tools/specphot_list.html

Table 1
Properties of the Quasars Observed with X–shooter

Quasar Name	ID	R.A. (J2000)	Decl. (J2000)	z_{sys}	z_{sys} Method	z_{sys} Reference	J (mag)	M_{1450} (mag)	Disk Ref.	Notes
PSO J004.3936+17.0862	P004+17	00:17:34.467	+17:05:10.70	5.8165 ± 0.0023	[C II] 158 μm	E20	20.67 ± 0.16	$-25.95^{-0.05}_{+0.04}$	B16	
PSO J007.0273+04.9571	P007+04	00:28:06.560	+04:57:25.68	6.0015 ± 0.0002	[C II] 158 μm	V20	19.77 ± 0.11	$-26.51^{-0.05}_{+0.06}$	B14, J15	pDLA
PSO J009.7355−10.4316	P009−10	00:38:56.522	−10:25:53.90	6.0040 ± 0.0003	[C II] 158 μm	V20	19.93 ± 0.07	$-26.03^{-0.04}_{+0.04}$	B16	BAL
PSO J011.3898+09.0324	P011+09	00:45:33.568	+09:01:56.96	6.4694 ± 0.0025	[C II] 158 μm	E20	20.80 ± 0.13	$-25.87^{-0.02}_{+0.02}$	M17	
VIK J0046−2837	J0046−2837	00:46:23.645	−28:37:47.34	5.9926 ± 0.0028	Mg II	Paper I	20.96 ± 0.09	$-25.09^{-0.19}_{+0.24}$	D18	
SDSS J0100+2802	J0100+2802	01:00:13.027	+28:02:25.84	6.3269 ± 0.0002	[C II] 158 μm	V20	17.64 ± 0.02	$-29.02^{-0.00}_{+0.00}$	W15	
VIK J0109−3047	J0109−3047	01:09:53.131	−30:47:26.31	6.7904 ± 0.0003	[C II] 158 μm	V20	21.27 ± 0.16	$-25.41^{-0.03}_{+0.03}$	V13	
PSO J036.5078+03.0498	P036+03	02:26:01.875	+03:02:59.40	6.5405 ± 0.0001	[C II] 158 μm	V20	19.51 ± 0.03	$-27.15^{-0.01}_{+0.01}$	V15	
VIK J0305−3150	J0305−3150	03:05:16.916	−31:50:55.90	6.6139 ± 0.0001	[C II] 158 μm	V19	20.68 ± 0.07	$-25.91^{-0.01}_{+0.01}$	V13	
PSO J056.7168−16.4769	P056−16	03:46:52.044	−16:28:36.88	5.9670 ± 0.0023	[C II] 158 μm	E20	20.25 ± 0.10	$-26.26^{-0.02}_{+0.02}$	B16	pDLA
PSO J065.4085−26.9543	P065−26	04:21:38.049	−26:57:15.61	6.1871 ± 0.0003	[C II] 158 μm	V20	19.36 ± 0.02	$-26.94^{-0.01}_{+0.01}$	B16	pDLA
PSO J065.5041−19.4579	P065−19	04:22:00.995	−19:27:28.69	6.1247 ± 0.0006	[C II] 158 μm	D18	19.90 ± 0.15	$-26.11^{-0.03}_{+0.03}$	B16	BAL
SDSS J0842+1218	J0842+1218	08:42:29.430	+12:18:50.50	6.0754 ± 0.0005	[C II] 158 μm	V20	19.78 ± 0.03	$-26.69^{-0.01}_{+0.01}$	D11,J15	BAL?
SDSS J1030+0524	J1030+0524	10:30:27.098	+05:24:55.00	6.3048 ± 0.0012	Lyα	F19	19.79 ± 0.08	$-26.76^{-0.02}_{+0.02}$	F01	
PSO J158.69378−14.421	P158−14	10:34:46.509	−14:25:15.89	6.0681 ± 0.0024	[C II] 158 μm	E20	19.19 ± 0.06	$-27.07^{-0.03}_{+0.03}$	C18	
PSO J159.2257−02.5438	P159−02	10:36:54.190	−02:32:37.94	6.3809 ± 0.0005	[C II] 158 μm	D18	20.00 ± 0.10	$-26.47^{-0.02}_{+0.02}$	B16	
SDSS J1044−0125	J1044−0125	10:44:33.041	−01:25:02.20	5.7846 ± 0.0005	[C II] 158 μm	V20	19.25 ± 0.05	$-27.16^{-0.03}_{+0.03}$	F00	BAL
VIK J1048−0109	J1048−0109	10:48:19.082	−01:09:40.29	6.6759 ± 0.0002	[C II] 158 μm	V20	20.65 ± 0.17	$-26.20^{-0.03}_{+0.03}$	W17	
ULAS J1120+0641	J1120+0641	11:20:01.478	+06:41:24.30	7.0848 ± 0.0004	[C II] 158 μm	V20	20.36 ± 0.05	$-26.40^{-0.00}_{+0.00}$	M11	
ULAS J1148+0702	J1148+0702	11:48:03.286	+07:02:08.33	6.3337 ± 0.0028	Mg II	Paper I	20.30 ± 0.11	$-26.31^{-0.01}_{+0.02}$	J16	
PSO J183.1124+05.0926	P183+05	12:12:26.984	+05:05:33.49	6.4386 ± 0.0002	[C II] 158 μm	V20	19.77 ± 0.08	$-26.87^{-0.01}_{+0.02}$	M17	pDLA
SDSS J1306+0356	J1306+0356	13:06:08.258	+03:56:26.30	6.0330 ± 0.0002	[C II] 158 μm	V20	19.71 ± 0.10	$-26.70^{-0.01}_{+0.01}$	F01	
ULAS J1319+0950	J1319+0950	13:19:11.302	+09:50:51.49	6.1347 ± 0.0005	[C II] 158 μm	V20	19.70 ± 0.03	$-26.80^{-0.00}_{+0.00}$	M09	
ULAS J1342+0928	J1342+0928	13:42:08.105	+09:28:38.61	7.5400 ± 0.0003	[C II] 158 μm	B19	20.30 ± 0.02	$-26.64^{-0.00}_{+0.00}$	B18	
CFHQS J1509−1749	J1509−1749	15:09:41.779	−17:49:26.80	6.1225 ± 0.0007	[C II] 158 μm	D18	19.80 ± 0.08	$-26.56^{-0.01}_{+0.01}$	W07	
PSO J231.6576−20.8335	P231−20	15:26:37.838	−20:50:00.66	6.5869 ± 0.0004	[C II] 158 μm	V20	19.66 ± 0.05	$-27.07^{-0.03}_{+0.03}$	M17	BAL?
PSO J239.7124−07.4026	P239−07	15:58:50.991	−07:24:09.59	6.1097 ± 0.0024	[C II] 158 μm	E20	19.35 ± 0.08	$-27.07^{-0.01}_{+0.02}$	B16	BAL
PSO J308.0416−21.2339	P308−21	20:32:09.994	−21:14:02.31	6.2355 ± 0.0003	[C II] 158 μm	V20	20.17 ± 0.11	$-26.27^{-0.01}_{+0.01}$	B16	
SDSS J2054−0005	J2054−0005	20:54:06.490	−00:05:14.80	6.0389 ± 0.0001	[C II] 158 μm	V20	20.12 ± 0.06	$-26.15^{-0.04}_{+0.05}$	J08	
CFHQS J2100−1715	J2100−1715	21:00:54.619	−17:15:22.50	6.0807 ± 0.0004	[C II] 158 μm	V20	21.42 ± 0.10	$-24.63^{-0.05}_{+0.05}$	W10	
PSO J323.1382+12.2986	P323+12	21:32:33.189	+12:17:55.26	6.5872 ± 0.0004	[C II] 158 μm	V20	19.74 ± 0.03	$-26.89^{-0.01}_{+0.01}$	M17	
VIK J2211−3206	J2211−3206	22:11:12.391	−32:06:12.95	6.3394 ± 0.0010	[C II] 158 μm	D18	19.62 ± 0.03	$-27.09^{-0.03}_{+0.03}$	D18	BAL
CFHQS J2229+1457	J2229+1457	22:29:01.649	+14:57:09.00	6.1517 ± 0.0005	[C II] 158 μm	W15	21.95 ± 0.07	$-24.43^{-0.07}_{+0.08}$	W10	
PSO J340.2041−18.6621	P340−18	22:40:49.001	−18:39:43.81	6.0007 ± 0.0020	Lyα	F19	20.28 ± 0.08	$-26.23^{-0.02}_{+0.02}$	B14	BAL
SDSS J2310+1855	J2310+1855	23:10:38.880	+18:55:19.70	6.0031 ± 0.0002	[C II] 158 μm	W13	18.88 ± 0.05	$-27.22^{-0.02}_{+0.02}$	W13, J16	BAL/pDLA
VIK J2318−3029	J2318−3029	23:18:33.103	−30:29:33.36	6.1456 ± 0.0002	[C II] 158 μm	V20	20.20 ± 0.06	$-26.11^{-0.02}_{+0.02}$	D18	BAL?
VIK J2348−3054	J2348−3054	23:48:33.336	−30:54:10.24	6.9007 ± 0.0005	[C II] 158 μm	V20	21.14 ± 0.08	$-25.79^{-0.03}_{+0.03}$	V13	BAL
PSO J359.1352−06.3831	P359−06	23:56:32.452	−06:22:59.26	6.1719 ± 0.0002	[C II] 158 μm	V20	19.85 ± 0.10	$-26.62^{-0.02}_{+0.02}$	B16, W16	

Note. References for z_{sys} and discovery are: B14—Bañados et al. (2014); B16—Bañados et al. (2016); B18—Bañados et al. (2018b); B19—Bañados et al. (2019); C18—Chehade et al. (2018); D18—Decarli et al. (2018); D11—De Rosa et al. (2011); E20—Eilers et al. (2020); F00—Fan et al. (2000); F01—Fan et al. (2001); F19—Farina et al. (2019); J08—Jiang et al. (2008); J15—Jiang et al. (2015); J16—Jiang et al. (2016); M17—Mazzucchelli et al. (2017); M09—Mortlock et al. (2009); M11—Mortlock et al. (2011); V13—Venemans et al. (2013); V15—Venemans et al. (2015); V19—Venemans et al. (2019); V20—Venemans et al. (2020); W16—Wang et al. (2016a); W17—Wang et al. (2017); W13—Wang et al. (2013); W07—Willott et al. (2007); W10—Willott et al. (2010a); W15—Willott et al. (2015); and W15—Wu et al. (2015).

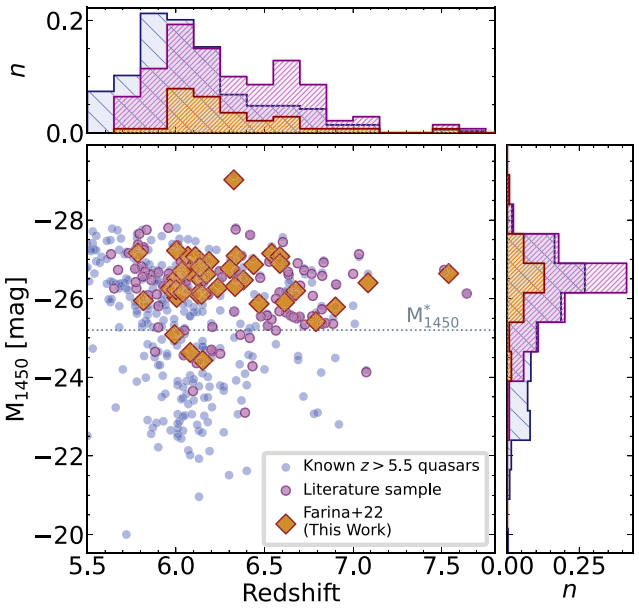

Figure 1. Distribution, in the redshift vs. absolute magnitude plane, of the 38 $z \gtrsim 5.7$ quasars in our sample (orange diamonds) and of the 97 quasars for which black hole masses and Eddington ratios have been presented in the literature (violet circles; see Section 5 for details). For comparison, pale blue circles indicate all high-redshift quasars published at the time of writing (2022 May). Data for the quasar J0439+1634 ($z = 6.51$), that is lensed by a foreground galaxy, has been corrected by the magnification factor of ∼51 calculated by Fan et al. (2019). The horizontal dotted line marks the characteristic magnitude of $z \gtrsim 6$ quasars ($M^*_{1450} \sim -25.2$ mag). Histograms on the top and right panels follow the same color scheme as the central panel and are normalized by the total number of objects (histograms of the quasars part of our sample and from the literature are stacked one above the other with normalization given by the total 38+97 number of objects). Most of the targets from our sample and from the literature have $M_{1450} \lesssim -26$ mag. Thus, we are probing the bright end of the underlying $z \gtrsim 6$ quasar population.

3.3.1. The Quasar's Continuum

The global continuum is constructed considering the following components:

1. accretion disk related emission is reproduced with a power law normalized at 2500 Å with slope α_λ;
2. the Balmer continuum at $\lambda_{\rm rest} < 3646$ Å is modeled by assuming the presence of gas clouds with uniform electron temperature ($T_e = 1.5 \times 10^4$ K), which are partially optically thick (e.g., Dietrich et al. 2003) and by fixing the normalization to be 30% of the power-law flux at the Balmer edge (see, e.g., Onoue et al. 2020, for further details);
3. the iron pseudo-continuum beneath the Mg II broad emission line is modeled with a template derived from the narrow-line Seyfert 1 galaxy I Zwicky-1 (Vestergaard & Wilkes 2001) with redshift and FWHM anchored to the fit of the Mg II line (see below for details).

The continuum emission of five quasars in our sample (P009−10,[23] J0046−2837, P065−26, P065−19, and J2100−1715) show at wavelengths $\lambda_{\rm rest} \lesssim 2000$ Å an apparent drop with respect to the fitted power law plus Balmer continuum emission. This is likely due to absorbing material located in front of the accretion disk (e.g., Gallerani et al. 2010). For these objects, the fit was performed separately for spectral regions around the C IV and around the Mg II emission lines.

[23] See also Farina et al. (2019) for peculiarities on the optical part of the spectrum of P009-10.

3.3.2. Quasar Broad-line Emission

The ultraviolet C IV and Mg II broad emission lines were fitted to derive single-epoch black hole masses and Eddington ratios for our sample of quasars (see Sections 4.2 and 4.3).

C IV—The broad C IV line is modeled with two Gaussian components in the rest-frame wavelength range $\lambda_{\rm rest} =$ 1470–1600 Å. If the resultant two components fit appears indistinguishable from a single Gaussian due to the S/N of a spectrum and/or to the symmetry of the line, the model of the line is reduced to a single Gaussian. BAL and other absorption features present close to the line are identified and excluded from the fit.

Mg II—The Mg II emission is modeled with a single Gaussian profile in the wavelength range 2700 Å $< \lambda_{\rm rest} <$ 2900 Å. The fits to the Mg II line and to the iron pseudo-continuum are connected. This means that, for each iteration, the redshifts and the FWHMs of the Mg II line are used as proxies for the corresponding values in the iron emission fit, until convergence is reached.

As discussed in Paper I, the adoption of an iron template that takes the iron contribution beneath the broad Mg II line into account (e.g., Tsuzuki et al. 2006) causes a *narrowing* of the measured line FWHM by ∼20% with respect to fit which use the Vestergaard & Wilkes (2001) model (Woo et al. 2018; Onoue et al. 2020; see also Trakhtenbrot & Netzer 2012 for the use of a different iron template). To estimate the black hole masses from the Mg II line, however, we will adopt the estimators of Vestergaard & Osmer (2009) and Shen et al. (2011; see Section 4.2), which are based on the Vestergaard & Wilkes (2001) iron template. To maximize consistency, the Mg II line properties reported in this paper will thus be determined employing the Vestergaard & Wilkes (2001) model.

4. Bolometric Luminosities, Black Hole Masses, and Eddington Ratios

We successfully fitted the Mg II broad emission line of 32 quasars and the C IV line of 34 quasars in our sample (see Figures 2 and 3, respectively). The broad-line emission has not been modeled in case it was redshifted in proximity of strong telluric absorption bands and/or in spectral regions with relatively low S/Ns. The derived continuum luminosities, line redshifts, integrated line luminosities, and FWHMs are listed in Table 2 for Mg II and in Table 3 for C IV. The quoted values are 50th (median), 16th, and 84th percentiles obtained by re-fitting each spectrum 1000 times after adding a Gaussian perturbation generated from the error vector to the observed flux. These quantities will be used to derive the physical properties of the central SMBHs.

4.1. Bolometric Luminosities

We estimate the bolometric luminosities ($L_{\rm bol}$) from the monochromatic luminosities at 3000 Å following the relation:

$$L_{\rm bol} = 5.15 \times 3000\ \text{Å}\ L_{\lambda,3000\text{Å}} \quad (1)$$

originally derived from a compilation of 259 bright SDSS quasars by Richards et al. (2006a) and then updated by Shen et al. (2011). This conversion is commonly used in high-redshift quasars studies (e.g., De Rosa et al. 2011;

Figure 2. Atlas of the Mg II emission for the 32 quasars in our sample for which the line was successfully fitted. Quasars are ordered by redshift, from low redshift on the top left to the highest redshift on the bottom right. In the top panel, we show the spectrum (in different shades of purple) and the corresponding 1–σ error for each object. The fits to the Mg II broad line and the iron pseudo-continuum are shown in pink and green dashed lines, respectively. The combined best fit of the continuum and the broad-line emission (see Section 3.3) is plotted as a solid yellow line. Residuals are displayed in gray in the bottom panel. In each panel, the spectrum is displayed in a $\pm$14,000 km s^{-1} range around the expected position of the Mg II line at the systemic redshift ($z_{\rm sys}$).

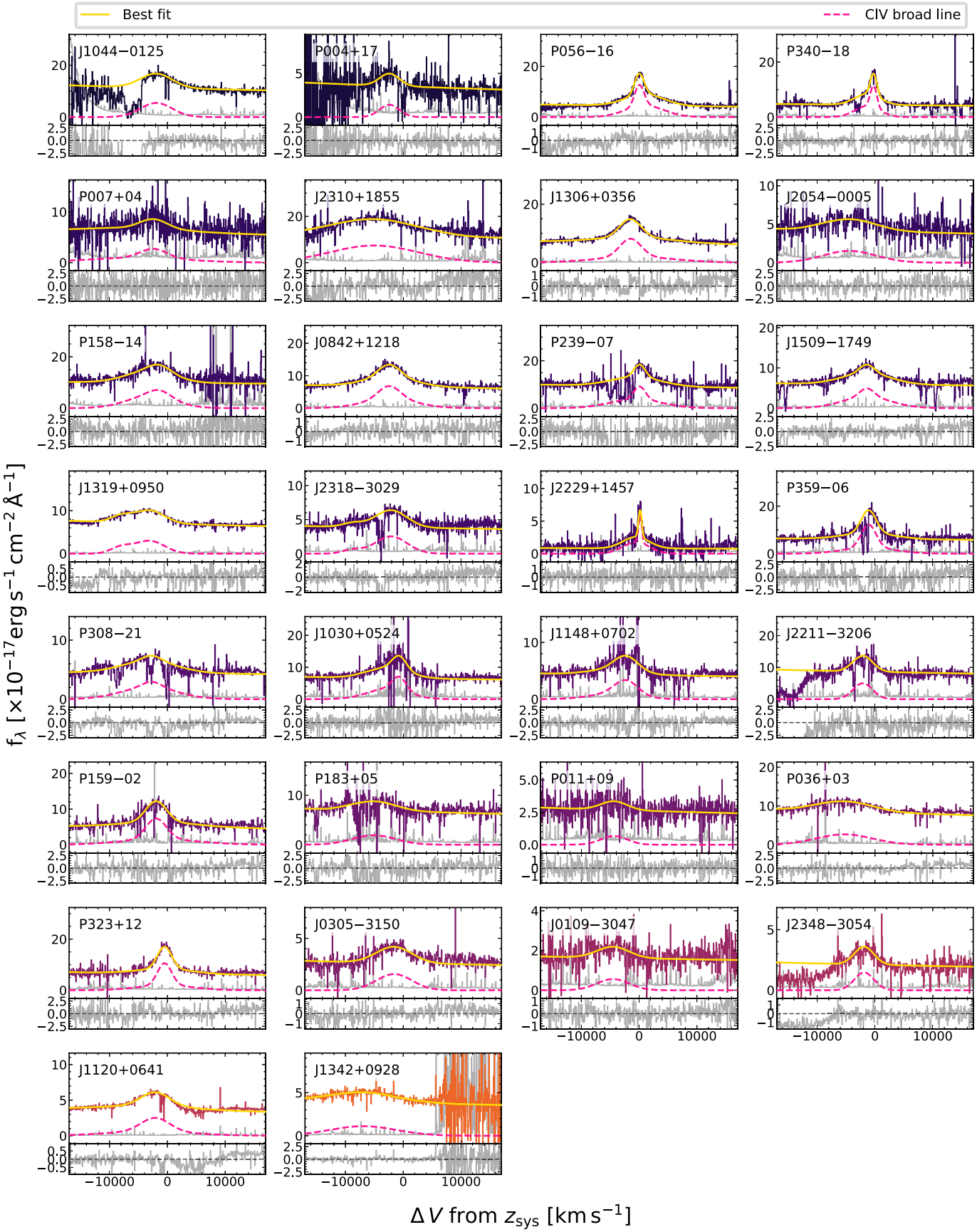

Figure 3. Same as Figure 2, but showing the C IV emission for the subsample of 34 quasars for which the line was successfully fitted. Each panel plots a region ±17,000 km s^{-1} around the systemic redshift reported in Table 1.

Table 2
Properties of the Mg II Broad-line Emission and of the Continuum at $\lambda_{\rm rest} = 3000$ Å

ID	3000 Å $f_{\lambda,3000\text{Å}}$ (10^{-13} erg s^{-1} cm^{-2})	3000 Å $L_{\lambda,3000\text{Å}}$ (10^{46} erg s^{-1})	$\lambda_{\rm MgII}$ (Å)	$z_{\rm MgII}$	FWHM$_{\rm MgII}$ (km s^{-1})	$f_{\rm MgII}$ (10^{-16} erg s^{-1} cm^{-2})	$L_{\rm MgII}$ (10^{44} erg s^{-1})
P004+17	$0.325^{+0.010}_{-0.011}$	$1.21^{+0.04}_{-0.04}$	…	…	…	…	…
P007+04	$0.980^{+0.033}_{-0.039}$	$3.91^{+0.13}_{-0.16}$	$19576.6^{+14.9}_{-13.1}$	$5.9946^{+0.0053}_{-0.0047}$	3203^{+1925}_{-591}	$6.0^{+0.9}_{-0.9}$	$2.4^{+0.4}_{-0.3}$
P009−10	$0.940^{+0.010}_{-0.010}$	$3.75^{+0.04}_{-0.04}$	…	…	…	…	…
P011+09	$0.336^{+0.007}_{-0.007}$	$1.60^{+0.03}_{-0.03}$	$20835.5^{+8.0}_{-14.1}$	$6.4444^{+0.0029}_{-0.0050}$	2238^{+744}_{-373}	$1.8^{+0.4}_{-0.2}$	$0.9^{+0.2}_{-0.1}$
J0046−2837	$0.390^{+0.017}_{-0.017}$	$1.55^{+0.07}_{-0.07}$	$19566.2^{+4.5}_{-4.6}$	$5.9910^{+0.0016}_{-0.0016}$	1974^{+134}_{-133}	$4.0^{+0.4}_{-0.4}$	$1.6^{+0.2}_{-0.2}$
J0100+2802	$6.608^{+0.007}_{-0.007}$	$29.78^{+0.03}_{-0.03}$	$20425.9^{+1.7}_{-1.7}$	$6.2981^{+0.0006}_{-0.0006}$	4962^{+65}_{-62}	$24.5^{+0.3}_{-0.3}$	$11.0^{+0.1}_{-0.1}$
J0109−3047	$0.281^{+0.007}_{-0.007}$	$1.49^{+0.04}_{-0.04}$	$21710.3^{+26.6}_{-27.2}$	$6.7570^{+0.0095}_{-0.0097}$	3530^{+590}_{-620}	$1.7^{+0.3}_{-0.3}$	$0.9^{+0.2}_{-0.2}$
P036+03	$0.996^{+0.006}_{-0.006}$	$4.85^{+0.03}_{-0.03}$	$21039.7^{+8.1}_{-9.4}$	$6.5174^{+0.0029}_{-0.0034}$	4840^{+364}_{-341}	$6.1^{+0.3}_{-0.3}$	$3.0^{+0.2}_{-0.1}$
J0305−3150	$0.366^{+0.004}_{-0.005}$	$1.83^{+0.02}_{-0.02}$	$21277.7^{+6.4}_{-7.1}$	$6.6024^{+0.0023}_{-0.0025}$	2347^{+239}_{-280}	$2.0^{+0.2}_{-0.2}$	$1.0^{+0.1}_{-0.1}$
P056−16	$0.523^{+0.006}_{-0.006}$	$2.06^{+0.02}_{-0.02}$	$19522.6^{+2.2}_{-2.3}$	$5.9754^{+0.0008}_{-0.0008}$	3049^{+121}_{-118}	$7.8^{+0.2}_{-0.2}$	$3.1^{+0.1}_{-0.1}$
P065−26	$0.984^{+0.021}_{-0.020}$	$4.21^{+0.09}_{-0.09}$	$19993.5^{+7.9}_{-8.8}$	$6.1436^{+0.0028}_{-0.0032}$	5558^{+352}_{-303}	$11.3^{+0.7}_{-0.8}$	$4.8^{+0.3}_{-0.3}$
P065−19	$0.889^{+0.018}_{-0.018}$	$3.72^{+0.07}_{-0.08}$	$19905.3^{+2.1}_{-2.0}$	$6.1121^{+0.0008}_{-0.0007}$	3861^{+109}_{-103}	$22.9^{+0.6}_{-0.6}$	$9.6^{+0.3}_{-0.3}$
J0842+1218	$0.917^{+0.009}_{-0.009}$	$3.76^{+0.04}_{-0.04}$	$19768.3^{+3.8}_{-4.1}$	$6.0632^{+0.0014}_{-0.0015}$	3422^{+153}_{-135}	$9.0^{+0.4}_{-0.4}$	$3.7^{+0.2}_{-0.2}$
J1030+0524	$1.041^{+0.016}_{-0.016}$	$4.65^{+0.07}_{-0.07}$	$20440.7^{+4.9}_{-4.4}$	$6.3034^{+0.0017}_{-0.0016}$	3511^{+209}_{-192}	$10.4^{+0.5}_{-0.5}$	$4.7^{+0.2}_{-0.2}$
P158−14	$2.219^{+0.051}_{-0.049}$	$9.08^{+0.21}_{-0.20}$	$19745.6^{+6.1}_{-7.7}$	$6.0550^{+0.0022}_{-0.0027}$	2794^{+208}_{-194}	$9.7^{+0.9}_{-1.0}$	$4.0^{+0.4}_{-0.4}$
P159−02	$0.769^{+0.014}_{-0.013}$	$3.53^{+0.06}_{-0.06}$	$20573.2^{+7.0}_{-7.2}$	$6.3507^{+0.0025}_{-0.0026}$	4798^{+286}_{-252}	$10.2^{+0.4}_{-0.5}$	$4.7^{+0.2}_{-0.2}$
J1044−0125	$1.384^{+0.024}_{-0.023}$	$5.07^{+0.09}_{-0.08}$	…	…	…	…	…
J1048−0109	$0.401^{+0.012}_{-0.011}$	$2.05^{+0.06}_{-0.06}$	$21382.9^{+24.1}_{-20.5}$	$6.6400^{+0.0086}_{-0.0073}$	4703^{+620}_{-635}	$4.4^{+0.6}_{-0.6}$	$2.2^{+0.3}_{-0.3}$
J1120+0641	$0.565^{+0.002}_{-0.002}$	$3.31^{+0.01}_{-0.01}$	…	…	…	…	…
J1148+0702	$0.721^{+0.009}_{-0.008}$	$3.24^{+0.04}_{-0.04}$	$20499.0^{+5.2}_{-6.0}$	$6.3242^{+0.0019}_{-0.0022}$	4895^{+165}_{-154}	$7.4^{+0.3}_{-0.3}$	$3.3^{+0.1}_{-0.1}$
P183+05	$0.928^{+0.012}_{-0.012}$	$4.36^{+0.06}_{-0.06}$	$20682.5^{+11.4}_{-10.5}$	$6.3898^{+0.0041}_{-0.0037}$	4459^{+311}_{-334}	$7.9^{+0.6}_{-0.5}$	$3.7^{+0.3}_{-0.2}$
J1306+0356	$0.902^{+0.006}_{-0.006}$	$3.64^{+0.02}_{-0.02}$	$19633.8^{+1.7}_{-1.7}$	$6.0151^{+0.0006}_{-0.0006}$	3895^{+69}_{-58}	$10.8^{+0.2}_{-0.2}$	$4.3^{+0.1}_{-0.1}$
J1319+0950	$0.818^{+0.003}_{-0.003}$	$3.43^{+0.01}_{-0.01}$	$19936.2^{+2.9}_{-3.1}$	$6.1231^{+0.0010}_{-0.0011}$	3747^{+112}_{-113}	$5.5^{+0.2}_{-0.2}$	$2.3^{+0.1}_{-0.1}$
J1342+0928	$0.558^{+0.004}_{-0.001}$	$3.77^{+0.03}_{-0.01}$	…	…	…	…	…
J1509−1749	$1.166^{+0.010}_{-0.011}$	$4.87^{+0.04}_{-0.05}$	$19922.9^{+3.3}_{-3.4}$	$6.1184^{+0.0012}_{-0.0012}$	4067^{+156}_{-153}	$9.3^{+0.4}_{-0.4}$	$3.9^{+0.2}_{-0.1}$
P231−20	$0.877^{+0.021}_{-0.021}$	$4.34^{+0.10}_{-0.10}$	$21152.8^{+15.0}_{-17.8}$	$6.5578^{+0.0054}_{-0.0063}$	5196^{+588}_{-493}	$9.7^{+0.9}_{-0.9}$	$4.8^{+0.5}_{-0.4}$
P239−07	$1.419^{+0.018}_{-0.020}$	$5.90^{+0.07}_{-0.08}$	$19906.3^{+2.8}_{-2.7}$	$6.1124^{+0.0010}_{-0.0010}$	3611^{+135}_{-150}	$15.4^{+0.6}_{-0.6}$	$6.4^{+0.2}_{-0.3}$
P308−21	$0.975^{+0.009}_{-0.009}$	$4.25^{+0.04}_{-0.04}$	$20195.9^{+16.4}_{-9.5}$	$6.2159^{+0.0059}_{-0.0034}$	3355^{+203}_{-361}	$7.0^{+0.6}_{-1.0}$	$3.1^{+0.3}_{-0.4}$
J2054−0005	$0.594^{+0.018}_{-0.015}$	$2.40^{+0.07}_{-0.06}$	$19628.7^{+7.4}_{-7.3}$	$6.0133^{+0.0026}_{-0.0026}$	3633^{+215}_{-230}	$7.5^{+0.5}_{-0.5}$	$3.1^{+0.2}_{-0.2}$
J2100−1715	$0.227^{+0.005}_{-0.005}$	$0.93^{+0.02}_{-0.02}$	$19851.9^{+18.6}_{-22.3}$	$6.0930^{+0.0066}_{-0.0080}$	8012^{+814}_{-1466}	$3.3^{+0.3}_{-0.5}$	$1.4^{+0.1}_{-0.2}$
P323+12	$0.786^{+0.008}_{-0.008}$	$3.89^{+0.04}_{-0.04}$	$21219.3^{+4.4}_{-4.6}$	$6.5816^{+0.0016}_{-0.0016}$	2803^{+174}_{-184}	$8.8^{+0.4}_{-0.4}$	$4.4^{+0.2}_{-0.2}$
J2211−3206	$1.285^{+0.025}_{-0.026}$	$5.82^{+0.11}_{-0.12}$	$20505.1^{+3.8}_{-4.1}$	$6.3264^{+0.0014}_{-0.0014}$	4666^{+196}_{-156}	$16.4^{+0.7}_{-0.6}$	$7.4^{+0.3}_{-0.3}$
J2229+1457	$0.131^{+0.008}_{-0.007}$	$0.55^{+0.03}_{-0.03}$	…	…	…	…	…
P340−18	$0.647^{+0.008}_{-0.007}$	$2.58^{+0.03}_{-0.03}$	$19578.8^{+3.2}_{-3.2}$	$5.9954^{+0.0012}_{-0.0012}$	2468^{+190}_{-144}	$6.3^{+0.3}_{-0.3}$	$2.5^{+0.1}_{-0.1}$
J2310+1855	$1.905^{+0.023}_{-0.021}$	$7.60^{+0.09}_{-0.09}$	$19580.6^{+6.6}_{-6.8}$	$5.9961^{+0.0024}_{-0.0024}$	3312^{+238}_{-213}	$14.3^{+0.9}_{-1.0}$	$5.7^{+0.4}_{-0.4}$
J2318−3029	$0.669^{+0.009}_{-0.010}$	$2.82^{+0.04}_{-0.04}$	$19987.2^{+5.6}_{-5.2}$	$6.1413^{+0.0020}_{-0.0018}$	3460^{+177}_{-160}	$5.2^{+0.3}_{-0.3}$	$2.2^{+0.1}_{-0.1}$
J2348−3054	$0.265^{+0.007}_{-0.007}$	$1.46^{+0.04}_{-0.04}$	$22063.2^{+23.0}_{-26.7}$	$6.8831^{+0.0082}_{-0.0095}$	5182^{+843}_{-811}	$3.0^{+0.4}_{-0.4}$	$1.7^{+0.2}_{-0.2}$
P359−06	$1.170^{+0.013}_{-0.014}$	$4.98^{+0.06}_{-0.06}$	$20013.2^{+12.0}_{-14.7}$	$6.1507^{+0.0043}_{-0.0053}$	3825^{+427}_{-370}	$5.9^{+0.7}_{-0.6}$	$2.5^{+0.3}_{-0.2}$

Mazzucchelli et al. 2017; Shen et al. 2019; Eilers et al. 2020; Onoue et al. 2020; Wang et al. 2021a). Given the ∼0.3 dex uncertainties in the determination of $L_{\rm bol}$ (e.g., Richards et al. 2006a; Shen et al. 2011), the choice of a different conversion has little impact on the general results of this paper. For instance, if we use the correction provided by Runnoe et al. (2012), the bolometric luminosity of sources in our sample would be, on average, ∼20% higher, while using the one from Trakhtenbrot & Netzer (2012) would result in bolometric luminosities that are ∼20% lower. Bolometric luminosities for all quasars in our sample are listed in Table 4.

4.2. Single-epoch Virial Black Hole Masses

Under the assumption that the clouds in the BLR orbit around an SMBH purely following gravitational dynamics, the mass of the central black hole can be estimated from the virial theorem: $M_{\rm BH} = G^{-1}\, R_{\rm BLR}\, v^2_{\rm BLR}$, where $R_{\rm BLR}$ is the radius of the BLR, and $v_{\rm BLR}$ is the cloud velocity.

Both $R_{\rm BLR}$ and $v_{\rm BLR}$ can be directly derived from a quasar spectrum by considering that: (i) broad emission-line reverberation-mapping of local active galactic nuclei (AGNs; e.g., Peterson et al. 2004) has revealed a tight correlation between the $R_{\rm BLR}$ and the AGN luminosity (e.g., Kaspi et al. 2005; Bentz et al. 2006, 2009); and (ii) $v_{\rm BLR}$ and the FWHM of a broad emission-line are related through a deprojection factor f of order unity (e.g., GRAVITY Collaboration et al. 2018, 2020). Thus, despite some potential biases (see, e.g., Shen & Liu 2012 and Shen 2013), the so-called single-epoch virial black hole masses can be calculated as:

$$\frac{M_{\rm BH}}{M_\odot} = 10^a \left(\frac{\rm FWHM}{10^3\ {\rm km\ s^{-1}}}\right)^2 \left(\frac{\lambda_{\rm rest}\, L_{\lambda,\lambda_{\rm rest}}}{10^{44}\ {\rm erg\ s^{-1}}}\right)^b, \qquad (2)$$

Table 3
Properties of the C IV Broad-line Emission and of the Continuum at $\lambda_{\rm rest} = 1350$ Å

ID	1350 Å $f_{\lambda,1350\text{Å}}$ (10^{-13} erg s^{-1} cm^{-2})	1350 Å $L_{\lambda,1350\text{Å}}$ (10^{46} erg s^{-1})	$\lambda_{\rm CIV}$ (Å)	$z_{\rm CIV}$	FWHM$_{\rm CIV}$ (km s^{-1})	$f_{\rm CIV}$ (10^{-16} erg s^{-1} cm^{-2})	$L_{\rm CIV}$ (10^{44} erg s^{-1})
P004+17	$0.623^{+0.032}_{-0.029}$	$2.31^{+0.12}_{-0.11}$	$10474.9^{+6.9}_{-6.7}$	$5.7620^{+0.0045}_{-0.0043}$	4071^{+451}_{-462}	$3.1^{+0.7}_{-0.6}$	$1.2^{+0.2}_{-0.2}$
P007+04	$0.911^{+0.053}_{-0.052}$	$3.63^{+0.21}_{-0.21}$	$10757.3^{+10.6}_{-11.5}$	$5.9442^{+0.0068}_{-0.0074}$	7278^{+1332}_{-1090}	$16.0^{+6.6}_{-5.2}$	$6.4^{+2.6}_{-2.1}$
P009−10	$0.482^{+0.028}_{-0.025}$	$1.92^{+0.11}_{-0.10}$	$10646.1^{+13.7}_{-17.1}$	$5.8725^{+0.0088}_{-0.0111}$	15746^{+2315}_{-2274}	$9.4^{+2.0}_{-1.9}$	$3.8^{+0.8}_{-0.7}$
P011+09	$0.437^{+0.011}_{-0.011}$	$2.07^{+0.05}_{-0.05}$	$11403.1^{+14.3}_{-13.8}$	$6.3611^{+0.0092}_{-0.0089}$	5378^{+994}_{-807}	$2.0^{+0.4}_{-0.4}$	$0.9^{+0.2}_{-0.2}$
J0046−2837	$0.210^{+0.061}_{-0.058}$	$0.83^{+0.24}_{-0.23}$	…	…	…	…	…
J0100+2802	$8.389^{+0.010}_{-0.010}$	$37.81^{+0.05}_{-0.05}$	…	…	…	…	…
J0109−3047	$0.248^{+0.008}_{-0.008}$	$1.32^{+0.04}_{-0.04}$	$11885.4^{+12.0}_{-11.6}$	$6.6725^{+0.0078}_{-0.0075}$	6636^{+799}_{-798}	$2.0^{+0.3}_{-0.3}$	$1.1^{+0.2}_{-0.2}$
P036+03	$1.396^{+0.009}_{-0.009}$	$6.79^{+0.04}_{-0.04}$	$11473.9^{+4.0}_{-4.0}$	$6.4068^{+0.0026}_{-0.0026}$	11640^{+557}_{-496}	$16.8^{+0.7}_{-0.7}$	$8.2^{+0.4}_{-0.3}$
J0305−3150	$0.425^{+0.006}_{-0.006}$	$2.12^{+0.03}_{-0.03}$	$11732.5^{+3.5}_{-3.6}$	$6.5737^{+0.0022}_{-0.0023}$	7277^{+301}_{-282}	$6.2^{+0.3}_{-0.3}$	$3.1^{+0.1}_{-0.1}$
P056−16	$0.762^{+0.013}_{-0.014}$	$3.00^{+0.05}_{-0.05}$	$10794.7^{+0.5}_{-0.5}$	$5.9684^{+0.0003}_{-0.0003}$	2642^{+57}_{-50}	$28.4^{+0.5}_{-0.6}$	$11.2^{+0.2}_{-0.2}$
P065−26	$1.097^{+0.018}_{-0.017}$	$4.70^{+0.08}_{-0.07}$	$10920.2^{+6.2}_{-5.9}$	$6.0494^{+0.0040}_{-0.0038}$	7766^{+268}_{-283}	$11.6^{+0.7}_{-0.7}$	$5.0^{+0.3}_{-0.3}$
P065−19	$0.499^{+0.021}_{-0.021}$	$2.09^{+0.09}_{-0.09}$	$10953.2^{+3.2}_{-3.6}$	$6.0707^{+0.0021}_{-0.0023}$	5638^{+245}_{-215}	$35.1^{+1.6}_{-1.5}$	$14.7^{+0.7}_{-0.6}$
J0842+1218	$1.067^{+0.014}_{-0.014}$	$4.38^{+0.06}_{-0.06}$	$10872.3^{+2.0}_{-1.8}$	$6.0185^{+0.0013}_{-0.0011}$	6027^{+135}_{-137}	$26.4^{+1.1}_{-1.0}$	$10.8^{+0.4}_{-0.4}$
J1030+0524	$1.034^{+0.019}_{-0.020}$	$4.62^{+0.09}_{-0.09}$	$11284.7^{+14.0}_{-15.7}$	$6.2847^{+0.0091}_{-0.0101}$	4733^{+517}_{-679}	$21.6^{+1.2}_{-1.2}$	$9.6^{+0.6}_{-0.5}$
P158−14	$1.443^{+0.045}_{-0.042}$	$5.90^{+0.18}_{-0.17}$	$10886.4^{+21.6}_{-15.5}$	$6.0276^{+0.0140}_{-0.0100}$	7703^{+369}_{-339}	$32.0^{+5.2}_{-2.8}$	$13.1^{+2.1}_{-1.2}$
P159−02	$0.768^{+0.016}_{-0.018}$	$3.53^{+0.07}_{-0.08}$	$11359.3^{+2.5}_{-2.3}$	$6.3329^{+0.0016}_{-0.0015}$	4921^{+210}_{-183}	$26.6^{+1.5}_{-1.4}$	$12.2^{+0.7}_{-0.6}$
J1044−0125	$1.872^{+0.067}_{-0.068}$	$6.85^{+0.25}_{-0.25}$	$10443.2^{+20.1}_{-30.2}$	$5.7415^{+0.0130}_{-0.0195}$	6478^{+1363}_{-1090}	$19.5^{+6.7}_{-4.8}$	$7.1^{+2.4}_{-1.8}$
J1048−0109	$0.553^{+0.019}_{-0.020}$	$2.82^{+0.10}_{-0.10}$	…	…	…	…	…
J1120+0641	$0.566^{+0.002}_{-0.003}$	$3.31^{+0.01}_{-0.02}$	$12435.2^{+1.3}_{-1.1}$	$7.0274^{+0.0009}_{-0.0007}$	6952^{+91}_{-86}	$11.9^{+0.3}_{-0.3}$	$7.0^{+0.2}_{-0.2}$
J1148+0702	$0.666^{+0.010}_{-0.011}$	$3.01^{+0.05}_{-0.05}$	$11267.3^{+9.0}_{-8.9}$	$6.2734^{+0.0058}_{-0.0057}$	5734^{+295}_{-295}	$11.8^{+1.0}_{-0.7}$	$5.3^{+0.4}_{-0.3}$
P183+05	$1.097^{+0.017}_{-0.019}$	$5.15^{+0.08}_{-0.09}$	$11328.2^{+11.5}_{-10.5}$	$6.3128^{+0.0074}_{-0.0067}$	8927^{+768}_{-649}	$9.2^{+1.0}_{-0.9}$	$4.3^{+0.5}_{-0.4}$
J1306+0356	$1.097^{+0.011}_{-0.010}$	$4.43^{+0.04}_{-0.04}$	$10840.5^{+0.7}_{-0.7}$	$5.9979^{+0.0005}_{-0.0004}$	5236^{+83}_{-99}	$32.1^{+0.9}_{-1.0}$	$13.0^{+0.4}_{-0.4}$
J1319+0950	$1.175^{+0.005}_{-0.005}$	$4.93^{+0.02}_{-0.02}$	$10932.8^{+2.5}_{-2.8}$	$6.0575^{+0.0016}_{-0.0018}$	8933^{+118}_{-110}	$13.3^{+0.2}_{-0.2}$	$5.6^{+0.1}_{-0.1}$
J1342+0928	$0.614^{+0.003}_{-0.002}$	$4.15^{+0.02}_{-0.01}$	$12921.3^{+4.4}_{-4.1}$	$7.3412^{+0.0029}_{-0.0026}$	13969^{+263}_{-334}	$8.3^{+0.2}_{-0.3}$	$5.6^{+0.1}_{-0.2}$
J1509−1749	$0.890^{+0.011}_{-0.012}$	$3.72^{+0.04}_{-0.05}$	$10981.3^{+1.8}_{-1.9}$	$6.0888^{+0.0012}_{-0.0012}$	5537^{+183}_{-175}	$18.7^{+0.9}_{-0.7}$	$7.8^{+0.4}_{-0.3}$
P231−20	$1.284^{+0.036}_{-0.035}$	$6.35^{+0.18}_{-0.17}$	…	…	…	…	…
P239−07	$1.481^{+0.023}_{-0.024}$	$6.15^{+0.09}_{-0.10}$	$11016.1^{+6.3}_{-16.6}$	$6.1113^{+0.0041}_{-0.0107}$	3633^{+827}_{-481}	$28.8^{+3.8}_{-2.1}$	$12.0^{+1.6}_{-0.9}$
P308−21	$0.648^{+0.006}_{-0.006}$	$2.82^{+0.03}_{-0.03}$	$11103.4^{+7.4}_{-6.9}$	$6.1677^{+0.0048}_{-0.0045}$	8035^{+749}_{-861}	$14.7^{+0.6}_{-0.6}$	$6.4^{+0.3}_{-0.2}$
J2054−0005	$0.657^{+0.025}_{-0.030}$	$2.66^{+0.10}_{-0.12}$	$10744.1^{+11.3}_{-10.6}$	$5.9357^{+0.0073}_{-0.0068}$	10795^{+2049}_{-1669}	$8.9^{+2.2}_{-1.6}$	$3.6^{+0.9}_{-0.6}$
J2100−1715	$0.126^{+0.010}_{-0.008}$	$0.52^{+0.04}_{-0.03}$	$10937.1^{+12.4}_{-15.8}$	$6.0603^{+0.0080}_{-0.0102}$	7433^{+2324}_{-999}	$1.6^{+0.5}_{-0.3}$	$0.7^{+0.2}_{-0.1}$
P323+12	$1.084^{+0.012}_{-0.012}$	$5.37^{+0.06}_{-0.06}$	$11734.0^{+0.8}_{-1.0}$	$6.5747^{+0.0005}_{-0.0007}$	3286^{+93}_{-83}	$25.4^{+0.8}_{-0.8}$	$12.6^{+0.4}_{-0.4}$
J2211−3206	$1.386^{+0.048}_{-0.042}$	$6.28^{+0.22}_{-0.19}$	$11289.0^{+3.8}_{-3.3}$	$6.2875^{+0.0024}_{-0.0021}$	3996^{+250}_{-246}	$10.9^{+1.1}_{-1.0}$	$4.9^{+0.5}_{-0.5}$
J2229+1457	$0.127^{+0.010}_{-0.010}$	$0.53^{+0.04}_{-0.04}$	$11084.8^{+0.5}_{-0.6}$	$6.1556^{+0.0003}_{-0.0004}$	886^{+51}_{-49}	$6.8^{+0.4}_{-0.3}$	$2.9^{+0.2}_{-0.1}$
P340−18	$0.712^{+0.013}_{-0.014}$	$2.84^{+0.05}_{-0.06}$	$10834.8^{+0.4}_{-0.4}$	$5.9943^{+0.0002}_{-0.0003}$	1767^{+44}_{-42}	$16.9^{+0.4}_{-0.4}$	$6.7^{+0.2}_{-0.2}$
J2310+1855	$1.749^{+0.040}_{-0.041}$	$6.98^{+0.16}_{-0.16}$	$10665.4^{+4.0}_{-3.9}$	$5.8849^{+0.0026}_{-0.0025}$	18297^{+651}_{-708}	$72.9^{+4.2}_{-4.0}$	$29.1^{+1.7}_{-1.6}$
J2318−3029	$0.592^{+0.010}_{-0.011}$	$2.49^{+0.04}_{-0.04}$	$10990.9^{+3.8}_{-4.0}$	$6.0950^{+0.0024}_{-0.0026}$	6733^{+397}_{-339}	$10.3^{+0.6}_{-0.6}$	$4.3^{+0.3}_{-0.2}$
J2348−3054	$0.350^{+0.010}_{-0.011}$	$1.93^{+0.06}_{-0.06}$	$12162.0^{+4.4}_{-5.0}$	$6.8510^{+0.0028}_{-0.0032}$	3982^{+272}_{-256}	$3.2^{+0.3}_{-0.3}$	$1.8^{+0.1}_{-0.1}$
P359−06	$0.929^{+0.015}_{-0.015}$	$3.95^{+0.06}_{-0.06}$	$11069.3^{+1.4}_{-1.0}$	$6.1456^{+0.0009}_{-0.0007}$	3520^{+123}_{-117}	$30.6^{+1.2}_{-1.3}$	$13.0^{+0.5}_{-0.5}$

where $L_{\lambda,\lambda_{\rm rest}}$ is the monochromatic continuum luminosity of the quasar at the rest-frame wavelength $\lambda_{\rm rest}$, and the coefficients a and b are empirically derived either directly against reverberation-mapping masses or by cross-correlating measurements from different broad lines. In Table 4 we report black hole masses obtained from the following estimators: ($a = 6.86$, $b = 0.5$, $x = 3000$ Å) from Vestergaard & Osmer (2009) and ($a = 6.74$, $b = 0.62$, $x = 3000$ Å) from Shen et al. (2011) for the Mg II broad line and ($a = 6.66$, $b = 0.53$, $x = 1350$ Å) from Vestergaard & Peterson (2006) for the C IV broad line.

We stress that individual black hole masses inferred with this approach are afflicted by systematic errors of $\sim 0.3 - 0.5$ dex (e.g., Vestergaard & Osmer 2009; Shen & Liu 2012). These are much larger than the statistical uncertainties associated with the fitting of the broad lines, which are reported in Table 4.

4.2.1. Which Black Hole Mass Estimator?

Given their extensive use in reverberation-mapping investigations (e.g., Kaspi et al. 2000; Bentz et al. 2006, 2009, 2013; De Rosa et al. 2018), the Balmer Hα and Hβ lines are typically considered the most reliable indicators for black hole mass estimates. At $z \gtrsim 4$, however, these lines move out of the K band and are, thus, virtually inaccessible from the ground. Hence, for high-redshift quasar studies, the Mg II and C IV lines are commonly used as surrogates.

In the last two decades, the number of AGNs with measured time lags between continuum and Mg II and C IV line flux fluctuations has been drastically increased (e.g., Peterson et al. 2004; Kaspi et al. 2007; Woo 2008; De Rosa et al. 2015; Sun et al. 2015; Lira et al. 2018; Kaspi et al. 2021). Nevertheless, the derived radius–luminosity relations are still poorly constrained and/or show significantly larger scatter with

Table 4
Properties of the Quasars Observed with X–shooter

ID	$L_{\rm bol}$ (10^{46} erg s^{-1})	$M_{\rm BH}^{\rm VO09}$ ($10^9\,M_\odot$)	$\lambda_{\rm Edd}^{\rm VO09}$	$M_{\rm BH}^{\rm S+11}$ ($10^9\,M_\odot$)	$\lambda_{\rm Edd}^{\rm S+11}$	$M_{\rm BH}^{\rm VP06}$ ($10^9\,M_\odot$)	$\lambda_{\rm Edd}^{\rm VP06}$	$M_{\rm BH}^{\rm C+17}$ ($10^9\,M_\odot$)	$\lambda_{\rm Edd}^{\rm C+17}$
P004+17	$6.21^{+0.20}_{-0.21}$	…	…	…	…	$1.35^{+0.28}_{-0.27}$	$0.36^{+0.08}_{-0.06}$	$0.59^{+0.12}_{-0.11}$	$0.84^{+0.17}_{-0.13}$
P007+04	$20.13^{+0.67}_{-0.81}$	$1.46^{+2.31}_{-0.49}$	$1.08^{+0.57}_{-0.66}$	$2.27^{+3.58}_{-0.75}$	$0.70^{+0.36}_{-0.42}$	$5.51^{+2.01}_{-1.48}$	$0.29^{+0.11}_{-0.08}$	$2.34^{+0.90}_{-0.63}$	$0.68^{+0.26}_{-0.20}$
P009−10	$19.32^{+0.21}_{-0.21}$	…	…	…	…	$18.44^{+5.32}_{-4.68}$	$0.36^{+0.10}_{-0.08}$	$2.35^{+0.61}_{-0.54}$	$2.81^{+0.80}_{-0.65}$
P011+09	$8.22^{+0.16}_{-0.16}$	$0.46^{+0.36}_{-0.14}$	$1.42^{+0.64}_{-0.62}$	$0.64^{+0.49}_{-0.19}$	$1.02^{+0.46}_{-0.45}$	$2.24^{+0.87}_{-0.62}$	$0.29^{+0.11}_{-0.08}$	$0.43^{+0.14}_{-0.10}$	$1.52^{+0.46}_{-0.36}$
J0046−2837	$7.98^{+0.34}_{-0.34}$	$0.35^{+0.04}_{-0.04}$	$1.80^{+0.30}_{-0.24}$	$0.49^{+0.06}_{-0.06}$	$1.30^{+0.21}_{-0.17}$	…	…	…	…
J0100+2802	$153.39^{+0.16}_{-0.15}$	$9.73^{+0.26}_{-0.24}$	$1.25^{+0.03}_{-0.03}$	$19.28^{+0.51}_{-0.47}$	$0.63^{+0.02}_{-0.02}$	…	…	…	…
J0109−3047	$7.69^{+0.20}_{-0.20}$	$1.11^{+0.40}_{-0.36}$	$0.55^{+0.26}_{-0.14}$	$1.53^{+0.56}_{-0.49}$	$0.40^{+0.19}_{-0.10}$	$2.68^{+0.64}_{-0.58}$	$0.23^{+0.06}_{-0.04}$	$0.48^{+0.11}_{-0.09}$	$1.27^{+0.27}_{-0.22}$
P036+03	$24.96^{+0.14}_{-0.15}$	$3.74^{+0.59}_{-0.51}$	$0.53^{+0.08}_{-0.07}$	$5.96^{+0.93}_{-0.81}$	$0.33^{+0.05}_{-0.04}$	$19.64^{+1.86}_{-1.63}$	$0.10^{+0.01}_{-0.01}$	$2.77^{+0.30}_{-0.24}$	$0.72^{+0.07}_{-0.07}$
J0305−3150	$9.42^{+0.10}_{-0.12}$	$0.54^{+0.11}_{-0.12}$	$1.39^{+0.40}_{-0.25}$	$0.77^{+0.16}_{-0.18}$	$0.98^{+0.29}_{-0.17}$	$4.14^{+0.34}_{-0.30}$	$0.18^{+0.01}_{-0.01}$	$2.87^{+0.35}_{-0.27}$	$0.26^{+0.03}_{-0.03}$
P056−16	$10.59^{+0.11}_{-0.11}$	$0.96^{+0.08}_{-0.07}$	$0.87^{+0.08}_{-0.07}$	$1.39^{+0.11}_{-0.10}$	$0.61^{+0.05}_{-0.05}$	$0.66^{+0.03}_{-0.02}$	$1.28^{+0.05}_{-0.05}$	…	…
P065−26	$21.69^{+0.46}_{-0.45}$	$4.60^{+0.57}_{-0.48}$	$0.38^{+0.05}_{-0.05}$	$7.20^{+0.88}_{-0.75}$	$0.24^{+0.03}_{-0.03}$	$7.19^{+0.47}_{-0.49}$	$1.23^{+0.14}_{-0.12}$	$0.90^{+0.06}_{-0.05}$	$9.85^{+1.15}_{-1.05}$
P065−19	$19.14^{+0.38}_{-0.39}$	$2.08^{+0.12}_{-0.10}$	$0.73^{+0.04}_{-0.04}$	$3.21^{+0.19}_{-0.16}$	$0.47^{+0.03}_{-0.03}$	$2.46^{+0.21}_{-0.17}$	$2.66^{+0.65}_{-0.52}$	$1.14^{+0.05}_{-0.05}$	$5.77^{+1.27}_{-1.08}$
J0842+1218	$19.37^{+0.20}_{-0.20}$	$1.64^{+0.15}_{-0.12}$	$0.94^{+0.08}_{-0.08}$	$2.54^{+0.23}_{-0.18}$	$0.61^{+0.05}_{-0.05}$	$4.17^{+0.18}_{-0.18}$	$0.37^{+0.02}_{-0.02}$	$1.80^{+0.08}_{-0.07}$	$0.85^{+0.04}_{-0.04}$
J1030+0524	$23.97^{+0.37}_{-0.36}$	$1.93^{+0.23}_{-0.20}$	$0.99^{+0.12}_{-0.11}$	$3.06^{+0.37}_{-0.31}$	$0.62^{+0.08}_{-0.07}$	$2.65^{+0.60}_{-0.71}$	$0.71^{+0.26}_{-0.13}$	$2.79^{+1.87}_{-0.44}$	$0.68^{+0.12}_{-0.27}$
P158−14	$46.75^{+1.08}_{-1.04}$	$1.70^{+0.25}_{-0.22}$	$2.18^{+0.34}_{-0.31}$	$2.93^{+0.43}_{-0.38}$	$1.27^{+0.20}_{-0.18}$	$7.99^{+0.70}_{-0.65}$	$0.46^{+0.04}_{-0.04}$	$4.97^{+2.83}_{-1.14}$	$0.75^{+0.23}_{-0.28}$
P159−02	$18.21^{+0.32}_{-0.32}$	$3.14^{+0.38}_{-0.31}$	$0.46^{+0.05}_{-0.05}$	$4.82^{+0.58}_{-0.48}$	$0.30^{+0.03}_{-0.03}$	$2.48^{+0.20}_{-0.17}$	$0.57^{+0.05}_{-0.04}$	$1.38^{+0.12}_{-0.10}$	$1.03^{+0.08}_{-0.08}$
J1044−0125	$26.09^{+0.45}_{-0.43}$	…	…	…	…	$6.12^{+2.73}_{-1.85}$	$0.34^{+0.14}_{-0.10}$	$3.37^{+0.52}_{-0.47}$	$0.61^{+0.10}_{-0.08}$
J1048−0109	$10.55^{+0.30}_{-0.30}$	$2.29^{+0.64}_{-0.57}$	$0.37^{+0.13}_{-0.08}$	$3.29^{+0.93}_{-0.82}$	$0.26^{+0.09}_{-0.06}$	…	…	…	…
J1120+0641	$17.05^{+0.07}_{-0.07}$	…	…	…	…	$4.79^{+0.12}_{-0.11}$	$0.28^{+0.01}_{-0.01}$	$2.40^{+0.06}_{-0.05}$	$0.57^{+0.01}_{-0.01}$
J1148+0702	$16.71^{+0.22}_{-0.19}$	$3.13^{+0.21}_{-0.19}$	$0.42^{+0.03}_{-0.03}$	$4.75^{+0.31}_{-0.28}$	$0.28^{+0.02}_{-0.02}$	$3.10^{+0.32}_{-0.31}$	$0.43^{+0.05}_{-0.04}$	$1.18^{+0.11}_{-0.09}$	$1.11^{+0.09}_{-0.10}$
P183+05	$22.43^{+0.30}_{-0.30}$	$3.00^{+0.43}_{-0.43}$	$0.59^{+0.10}_{-0.08}$	$4.72^{+0.68}_{-0.67}$	$0.38^{+0.06}_{-0.05}$	$9.97^{+1.71}_{-1.36}$	$0.18^{+0.03}_{-0.02}$	$1.51^{+0.37}_{-0.25}$	$1.18^{+0.23}_{-0.23}$
J1306+0356	$18.74^{+0.12}_{-0.12}$	$2.10^{+0.07}_{-0.06}$	$0.71^{+0.02}_{-0.02}$	$3.23^{+0.11}_{-0.10}$	$0.46^{+0.01}_{-0.02}$	$3.16^{+0.10}_{-0.11}$	$0.46^{+0.02}_{-0.01}$	$2.33^{+0.06}_{-0.06}$	$0.63^{+0.02}_{-0.02}$
J1319+0950	$17.67^{+0.06}_{-0.06}$	$1.89^{+0.11}_{-0.11}$	$0.75^{+0.05}_{-0.04}$	$2.88^{+0.17}_{-0.17}$	$0.49^{+0.03}_{-0.03}$	$9.76^{+0.24}_{-0.23}$	$0.14^{+0.00}_{-0.00}$	$2.86^{+0.11}_{-0.10}$	$0.49^{+0.02}_{-0.02}$
J1342+0928	$19.43^{+0.13}_{-0.01}$	…	…	…	…	$21.78^{+0.80}_{-1.00}$	$0.07^{+0.00}_{-0.00}$	$1.97^{+0.09}_{-0.08}$	$0.79^{+0.03}_{-0.03}$
J1509−1749	$25.09^{+0.22}_{-0.24}$	$2.65^{+0.21}_{-0.19}$	$0.76^{+0.06}_{-0.06}$	$4.22^{+0.33}_{-0.30}$	$0.47^{+0.04}_{-0.03}$	$3.23^{+0.21}_{-0.20}$	$0.61^{+0.04}_{-0.04}$	$2.49^{+0.18}_{-0.16}$	$0.80^{+0.06}_{-0.06}$
P231−20	$22.34^{+0.54}_{-0.52}$	$4.06^{+1.00}_{-0.74}$	$0.43^{+0.10}_{-0.08}$	$6.40^{+1.56}_{-1.18}$	$0.28^{+0.06}_{-0.05}$	…	…	…	…
P239−07	$30.37^{+0.38}_{-0.43}$	$2.29^{+0.17}_{-0.18}$	$1.05^{+0.10}_{-0.08}$	$3.73^{+0.28}_{-0.29}$	$0.65^{+0.06}_{-0.05}$	$1.82^{+0.91}_{-0.45}$	$1.30^{+0.42}_{-0.43}$	…	…
P308−21	$21.89^{+0.19}_{-0.19}$	$1.69^{+0.20}_{-0.35}$	$1.03^{+0.27}_{-0.11}$	$2.65^{+0.32}_{-0.56}$	$0.66^{+0.17}_{-0.07}$	$5.87^{+1.14}_{-1.19}$	$0.29^{+0.07}_{-0.05}$	$2.09^{+0.52}_{-0.49}$	$0.82^{+0.25}_{-0.16}$
J2054−0005	$12.37^{+0.37}_{-0.31}$	$1.48^{+0.18}_{-0.17}$	$0.66^{+0.10}_{-0.07}$	$2.17^{+0.27}_{-0.25}$	$0.45^{+0.06}_{-0.05}$	$10.24^{+3.95}_{-2.79}$	$0.10^{+0.04}_{-0.03}$	$1.92^{+0.83}_{-0.52}$	$0.51^{+0.19}_{-0.15}$
J2100−1715	$4.80^{+0.10}_{-0.11}$	$4.49^{+0.92}_{-1.51}$	$0.08^{+0.04}_{-0.01}$	$5.88^{+1.18}_{-1.96}$	$0.06^{+0.03}_{-0.01}$	$2.04^{+1.44}_{-0.46}$	$1.00^{+0.42}_{-0.40}$	$2.55^{+1.33}_{-0.71}$	$0.82^{+0.45}_{-0.30}$
P323+12	$20.04^{+0.20}_{-0.21}$	$1.13^{+0.14}_{-0.14}$	$1.42^{+0.21}_{-0.16}$	$1.75^{+0.22}_{-0.22}$	$0.92^{+0.13}_{-0.11}$	$1.38^{+0.08}_{-0.07}$	$1.14^{+0.06}_{-0.06}$	$2.29^{+0.10}_{-0.10}$	$0.69^{+0.03}_{-0.03}$
J2211−3206	$29.97^{+0.58}_{-0.61}$	$3.82^{+0.30}_{-0.25}$	$0.63^{+0.05}_{-0.05}$	$6.21^{+0.48}_{-0.41}$	$0.38^{+0.03}_{-0.03}$	$2.22^{+0.25}_{-0.24}$	$1.05^{+0.11}_{-0.09}$	$1.12^{+0.10}_{-0.10}$	$2.10^{+0.17}_{-0.16}$
J2229+1457	$2.86^{+0.17}_{-0.15}$	…	…	…	…	$0.03^{+0.00}_{-0.00}$	$7.71^{+1.10}_{-0.96}$	…	…
P340−18	$13.28^{+0.16}_{-0.15}$	$0.71^{+0.11}_{-0.08}$	$1.49^{+0.19}_{-0.20}$	$1.05^{+0.16}_{-0.12}$	$1.01^{+0.13}_{-0.14}$	$0.29^{+0.01}_{-0.01}$	$3.71^{+0.19}_{-0.18}$	$0.59^{+0.03}_{-0.03}$	$1.78^{+0.08}_{-0.09}$
J2310+1855	$39.13^{+0.47}_{-0.44}$	$2.19^{+0.33}_{-0.27}$	$1.42^{+0.20}_{-0.19}$	$3.68^{+0.55}_{-0.46}$	$0.85^{+0.12}_{-0.11}$	$49.23^{+3.13}_{-3.27}$	$0.06^{+0.00}_{-0.00}$	$7.51^{+0.47}_{-0.52}$	$0.41^{+0.03}_{-0.02}$
J2318−3029	$14.53^{+0.20}_{-0.21}$	$1.45^{+0.15}_{-0.13}$	$0.79^{+0.08}_{-0.08}$	$2.17^{+0.23}_{-0.19}$	$0.53^{+0.05}_{-0.05}$	$3.87^{+0.44}_{-0.37}$	$0.30^{+0.03}_{-0.03}$	$1.94^{+0.23}_{-0.19}$	$0.59^{+0.06}_{-0.06}$
J2348−3054	$7.51^{+0.20}_{-0.19}$	$2.35^{+0.85}_{-0.67}$	$0.25^{+0.10}_{-0.07}$	$3.25^{+1.17}_{-0.93}$	$0.18^{+0.08}_{-0.05}$	$1.18^{+0.15}_{-0.14}$	$0.50^{+0.06}_{-0.05}$	$0.68^{+0.08}_{-0.07}$	$0.87^{+0.10}_{-0.08}$
P359−06	$25.65^{+0.29}_{-0.31}$	$2.36^{+0.56}_{-0.44}$	$0.86^{+0.20}_{-0.17}$	$3.78^{+0.89}_{-0.70}$	$0.54^{+0.12}_{-0.10}$	$1.35^{+0.09}_{-0.09}$	$1.49^{+0.10}_{-0.09}$	$1.32^{+0.10}_{-0.09}$	$1.52^{+0.12}_{-0.11}$

respect to the ones based on Hβ (e.g., Grier et al. 2019; Homayouni et al. 2020, and references therein). A strong correlation between the width of the Mg II and the Hβ lines has been observed (e.g., Trakhtenbrot & Netzer 2012; Shen & Liu 2012), suggesting that estimators relying on this low-ionization line deliver trustworthy black hole masses for high-redshift quasars. On the other hand, the frequent occurrence of prominent blueshifts and asymmetric line shapes, and the poor correlation with the width of the Hβ (or Mg II) line imply that the high-ionization C IV line is more affected by nonvirial components and, thus, generates more biased mass estimates (e.g., Baskin & Laor 2005; Richards et al. 2011; Marziani & Sulentic 2012; Shen & Liu 2012; Shen 2013; Trakhtenbrot & Netzer 2012; Coatman et al. 2016, 2017; Marziani et al. 2019; Wang et al. 2020b; Zuo et al. 2020). In addition, the frequent presence of strong absorption systems makes the reconstruction of the intrinsic C IV line profile arduous. This is particularly relevant at $z \gtrsim 6.5$, when bright quasars experience a sharp increase in the mean C IV blueshift (e.g., De Rosa et al. 2014; Mazzucchelli et al. 2017; Meyer et al. 2019; Reed et al. 2019; Shen et al. 2019; Yang et al. 2021; Paper I) and an increase in the frequency of BAL features (e.g., Yang et al. 2021; Bischetti et al. 2022). To reduce the influence of the nonvirial contributions on the C IV emission, we also estimate black hole masses employing the empirical C IV-blueshift dependent correction to the Vestergaard & Peterson (2006) relation provided by Coatman et al. (2017; but see Mejía-Restrepo et al. 2018, for limitations of this approach).[24] C IV–based black hole masses and Eddington ratios calculated using the

[24] For the majority of our sample, the systemic redshift of the quasar host galaxies is measured from the [C II] 158 μm line (see Table 1 and Paper I) while Coatman et al. (2017) used systemic redshifts derived from the Hα (and Hβ) Balmer lines. Fortunately, redshifts determined from these Hydrogen lines are typically similar to the systemic ones (e.g., Bonning et al. 2007). The difference between these two approaches has only a marginal effect on the derived black hole masses.

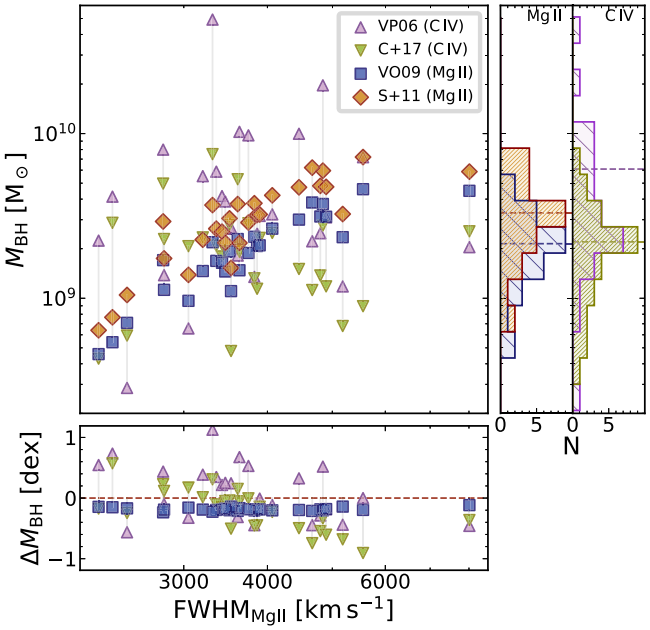

Figure 4. Black hole mass vs. FWHM of the Mg II line for the 28 quasars in our sample for which both the Mg II and C IV lines were successfully fitted (see Section 3.3). Pink triangles, green triangles, blue squares, and orange diamonds mark masses obtained with the Vestergaard & Peterson (2006), Coatman et al. (2017), Vestergaard & Osmer (2009), and Shen et al. (2011) estimators, respectively (see Table 4). Pale gray lines connect different mass estimates of the same object. The histograms on the right illustrate how the different recipes affect the mass distribution (the color scheme is the same as in the main panel). Horizontal dashed lines locate the corresponding averages. The average (median) masses of this subsample are 3.3×, 2.1×, 6.1×, and $2.2 \times 10^9\,M_\odot$ (3.1×, 2.0×, 3.1×, and $2.0 \times 10^9\,M_\odot$) if calculated with the Shen et al. (2011), Vestergaard & Osmer (2009), Vestergaard & Peterson (2006), and Coatman et al. (2017) estimators, respectively. The scatter plot on the bottom displays mass differences with respect to the Shen et al. (2011) estimator (see Section 4.2).

Coatman et al. (2017) correction are listed in Table 4). The quasars P056−16, P239−07, and J2229+1457 present a redshift of the C IV line with respect to the systemic redshift (see Paper I). For these, the Coatman et al. (2017) correction has not been applied.

Henceforth we will consider as *fiducial* the black hole masses derived from the Mg II line using the Shen et al. (2011) estimator. This is selected mainly to remain consistent with previous studies of large samples of intermediate-redshift quasars (in particular the one from SDSS; e.g., York et al. 2000; Shen et al. 2011) that we will compare our results with. For objects that only have a successful C IV line fit (see Section 3.3), we will instead adopt the masses calculated using the Vestergaard & Peterson (2006) estimator.

These choices will have an impact on our result. To quantify this, in Figure 4 we compare black hole mass estimates for the subsample of 28 quasars for which we have both the Mg II and the C IV line fits. In general, due to different zero-points, the Mg II–based estimator from Vestergaard & Osmer (2009) predicts masses that are systematically offset by ∼0.2 dex with respect to that of Shen et al. (2011). Consequently, if we had used the Vestergaard & Osmer recipe as our fiducial one, all Eddington ratios (see Section 4.3) would be a factor ∼1.5 × higher. Masses derived from the C IV line with the Vestergaard & Peterson (2006) estimator are consistent within ∼0.4 dex with those calculated using the Shen et al. (2011) calibration. The Coatman et al. (2017) correction consistently reduces the scatter between the Vestergaard & Peterson (2006) and the Shen et al. (2011) black hole masses for quasars with $\mathrm{FWHM_{MgII}} \lesssim 4000\,\mathrm{km\,s^{-1}}$. Yet, it systematically underestimates masses for quasars with a broader Mg II line. This causes the masses derived with the Coatman et al. (2017) correction to be, typically, ∼0.2 dex lower than those of Shen et al. (2011) for the entire subsample, and ∼0.5 dex lower if we limit the comparison to quasars with $\mathrm{FWHM_{MgII}} > 4000\,\mathrm{km\,s^{-1}}$. To avoid the introduction of biases in the masses of the most-massive objects, we therefore opt not to use the Coatman et al. (2017) correction for the measured C IV FWHMs.

4.3. Eddington Ratios

The so-called Eddington ratio ($\lambda_{\rm Edd}$) measures the ratio of the bolometric luminosity of a quasar (see Section 4.1) to its Eddington luminosity ($L_{\rm Edd}$); i.e., the theoretical maximum luminosity that can be emitted when radiation pressure and gravity are in equilibrium in a spherical geometry (Eddington 1926). While the exact limit depends on the chemical composition of the gas surrounding the SMBH, the Eddington luminosity that is typically reported assumes hydrostatic equilibrium of pure ionized hydrogen:

$$L_{\rm Edd} = \frac{4\pi G M_{\rm BH} m_{\rm p} c}{\sigma_{\rm T}} = 1.257 \times 10^{38}\,\mathrm{erg\,s^{-1}} \left(\frac{M_{\rm BH}}{M_\odot}\right), \quad (3)$$

where G is the gravitational constant, $m_{\rm p}$ is the mass of a proton, c is the speed of light, and $\sigma_{\rm T}$ is the Thomson scattering cross section. Eddington ratios ($\lambda_{\rm Edd} = L_{\rm bol}/L_{\rm Edd}$) calculated for different mass estimators (see Section 4.2) are reported in Table 4.

5. Results and Discussion

To summarize our findings: our sample of 38 bright (with $L_{\rm bol} \gtrsim 2.9 \times 10^{46}\,\mathrm{erg\,s^{-1}}$) $z > 5.7$ quasars have black hole masses ranging from $\sim 3.0 \times 10^7\,M_\odot$ to $\sim 2.2 \times 10^{10}\,M_\odot$ (with an average of $\sim 4.6 \times 10^9\,M_\odot$ and a median of $\sim 3.2 \times 10^9\,M_\odot$) and typically have accretion rates between 0.1 and 1 Eddington (see Figure 5, orange diamonds).

Our results are complemented by all of the $z \gtrsim 5.7$ quasars for which deep optical-to-near-IR spectroscopic observations are available in the literature (see Figure 1). This literature sample consists of 97 quasars from Willott et al. (2010b), De Rosa et al. (2011), Mazzucchelli et al. (2017), Chehade et al. (2018), Onoue et al. (2019), Reed et al. (2019), Pons et al. (2019), Shen et al. (2019), Matsuoka et al. (2019), Andika et al. (2020), Eilers et al. (2021), Wang et al. (2020a, 2021a), Bañados et al. (2021), and Yang et al. (2020, 2021; pink circles in Figure 5). All of these measurements have been homogenized to the same cosmological parameter and to the same bolometric luminosity and black hole mass estimators used in this paper (see Section 4 for details). Quasars duplicated among these samples are removed, and only the most recent measurement is taken into account. The Mg II emission line of the $z \gtrsim 7.1$ quasars in our sample is redshifted into the order 11 of the X–shooter near–IR arm. At these wavelengths, the efficiency of the instrument is hampered by the rise of the thermal background. Instead of the values derived from the C IV line listed in Table 4, we will recalculate black hole masses and Eddington ratios of the two quasars J1120+0641

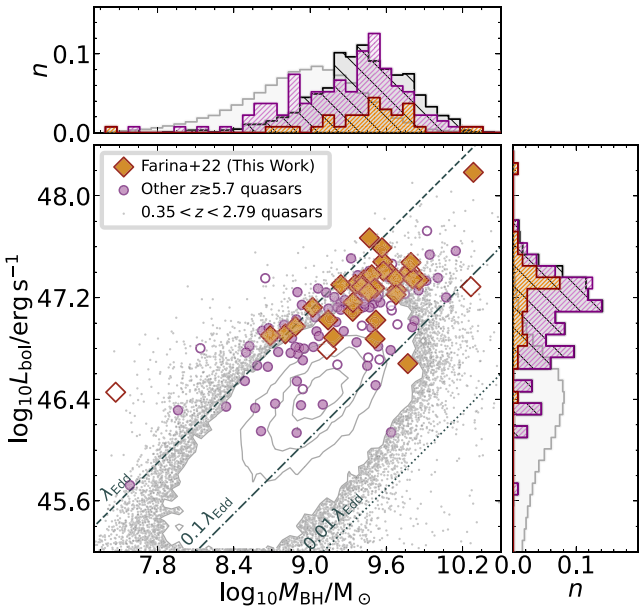

Figure 5. Distribution of our X–shooter/ALMA sample (orange diamonds) and from other $z \gtrsim 5.7$ studies (violet circles) in the black hole mass vs. bolometric luminosity plane. Filled symbols indicate that the Mg II line was used to derive the black hole mass, while empty symbols indicate the use of the C IV line. Gray contours and gray points indicate the location of SDSS DR7 $0.35 < z < 2.79$ quasars for which either Mg II or C IV lines were fitted by Shen et al. (2011). Diagonal gray lines mark lines of constant Eddington ratio, with dotted, dashed–dotted, and dashed lines indicating $0.01\times$, $0.1\times$, and $1\times$ the Eddington limit, respectively. Histograms in the right and top panels are normalized to the total number of objects and follow the same color scheme as the main panel. The top and right panels also show the distribution of $0.6 \lesssim z \lesssim 2.3$ luminosity-matched quasars as black hatched histograms.

($z = 7.08$) and J1342+0928 ($z = 7.54$) using the measurements of the Mg II line (based on Gemini/GNIRS spectra) reported in Yang et al. (2021).

In the following sections, we will refer to the 38 quasars studied here as the X–shooter /ALMA sample, while to the $38 + 97 = 135$ $z \gtrsim 5.7$ quasars with black hole mass estimates as the *full sample*. In all of the figures, quasars part of the X–shooter /ALMA sample will be plotted as orange diamonds (filled in case the black hole mass is derived from the Mg II line and empty if from the C IV line), while measurements from the literature will be shown as pink circles (with the same convention for black hole mass estimators). Histograms will follow the same color scheme, and the X–shooter /ALMA sample and the literature sample will be stacked one on the top of the other to represent the distribution of the *full sample*. Both of their normalizations will be set by the relevant number of objects in the *full sample*. Box plots above the histograms will indicate the median and the 25th and 75th percentiles, while the whiskers will mark the 16th and 84th percentiles.

In Figure 5 we also show the location of lower-redshift ($0.35 < z < 2.79$) SDSS DR7 quasars that have either Mg II or C IV black hole mass estimates by Shen et al. (2011; gray contours and points). The entirety of the full sample of $z \gtrsim 5.7$ quasars, spanning ~2.5 orders of magnitude in $L_{\rm bol}$, appears to inhabit the same locus of similarly luminous objects at lower redshifts. To quantify this, we constructed a bolometric luminosity-matched control sample of $0.56 < z < 2.30$ quasars. Given that we calculate bolometric luminosities following Equation (1), this choice corresponds to matching the monochromatic luminosities at 3000 Å of high- and low-redshift quasars. The redshift range was selected to ensure a good spectral coverage of the Mg II and of the C IV broad emission lines, to avoid potential contamination from host galaxies (e.g., Shen et al. 2011), and to reduce the impact of biases introduced due to the low efficiency in the SDSS color selection of $2.7 \lesssim z \lesssim 3.5$ quasars (e.g., Richards et al. 2006a, 2006b; Worseck & Prochaska 2011). Specifically, starting from the SDSS DR7 sample, we first removed all sources for which the Mg II and the C IV lines were too narrow or poorly measured; i.e., for both lines we required: FWHM_LINE $>$ 2 $\times$ FWHM_LINE_ERR, EW_LINE $>$ 2 $\times$ EW_LINE_ERR, and FWHM_LINE $>$ 1000 km s^{-1} (see, e.g., Richards et al. 2006a). For each of the $z \gtrsim 5.7$ quasars, we then selected 10 radio-quiet sources with bolometric luminosities closest to the luminosity of the quasar. In addition, consistency in the black hole mass estimators is accomplished by making sure that each high-redshift quasar and its 10 low-redshift analogs have masses calculated with the same estimator (black histograms in Figure 5).

A 2D Kolmogorov–Smirnov test (Kolmogorov 1933; Smirnov 1948; Fasano & Franceschini 1987) comparing the distribution in the black hole masses versus bolometric luminosity plane of the *full sample* and the luminosity-matched control sample returns a p-value $\sim 3.6 \times 10^{-2}$. Thus, the difference between the two is not significant enough (at the $\sim 2.1\sigma$ level) to imply that they are drawn from distinct parent populations. However, while the distributions of bolometric luminosities of the two samples are consistent by construction, the control sample appears to have, on average, slightly larger black hole masses with respect to the population of $z \gtrsim 5.7$ quasars (top panel of Figure 5). A two-sample Kolmogorov–Smirnov test performed with bootstrap resampling over the black hole mass distributions of the *full sample* and of the luminosity-matched control sample results in a p-value $\sim 1.9 \times 10^{-3}$, implying that the two distribution are different at the $\sim 3.1\sigma$ level ($\sim 3.2\sigma$ if only black hole masses derived from the Mg II are considered). In the following sections we will quantify this difference in terms of Eddington ratios. Note that we excluded from these comparisons the ultraluminous quasar J0100+2802. While the known number of such bright quasars is increasing (e.g., Schindler et al. 2017, 2018, 2019; Calderone et al. 2019), they are still underrepresented in the SDSS sample. Its inclusion would otherwise bias the control sample toward lower luminosities.

5.1. The Eddington Ratio Distribution

Our analysis shows that the bright quasars in our X–shooter/ALMA sample are accreting at a moderately high Eddington ratio with a median of $\lambda_{\rm Edd} = 0.48^{+0.06}_{-0.02}$ (with errors derived from bootstrap resampling of the distributions) with 16th and 84th percentiles equal to $p_{16\rm th} = 0.29$ and $p_{84\rm th} = 0.94$. More generally, $z \gtrsim 5.7$ quasars in the *full sample* have Eddington ratios within the fairly narrow range with $p_{16\rm th} = 0.23$ and $p_{84\rm th} = 0.97$ (with a median of $\lambda_{\rm Edd} = 0.47^{+0.05}_{-0.01}$). For comparison, Shen et al. (2019) reported a median Eddington ratio of ~0.31. While Mazzucchelli et al. (2019) and Yang et al. (2021), using the Vestergaard & Osmer (2009) black hole mass estimator, reported median values of ~0.31 and ~0.85, respectively.

Intriguingly, despite the large systematics in the black hole mass and bolometric luminosity estimates (of the order of 0.3−0.5 dex; see Section 4), only three quasars appear to have

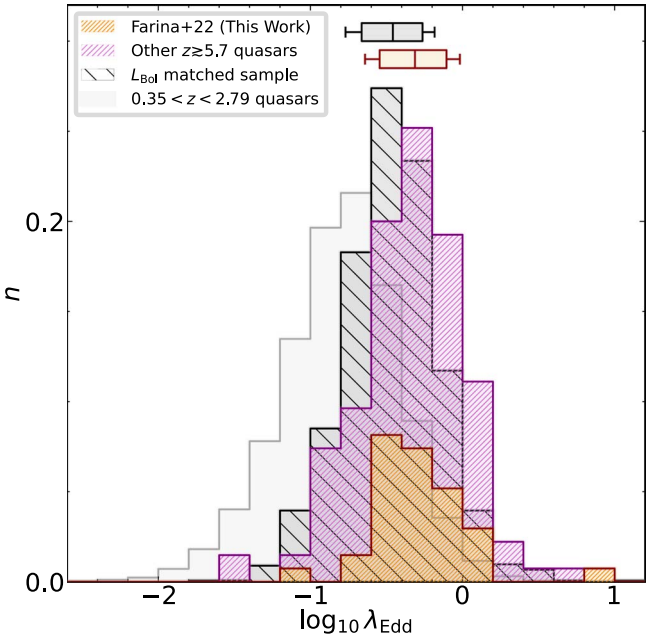

Figure 6. Logarithmic Eddington ratio distributions for the full sample of $z\gtrsim5.7$ quasars (orange for our X–shooter sample and violet for other studies) and for the bolometric luminosity-matched sample described in Section 5 (black hatched histogram). The high- and low-redshift distributions have similar dispersions ($\sim$0.3), but $z\gtrsim5.7$ quasars have a median Eddington ratio (top red rectangle) that is higher than their lower-redshift counterparts (top black rectangle). For the sake of comparison, we also show the sample of $0.35<z<2.79$ SDSS quasars as a pale gray histogram.

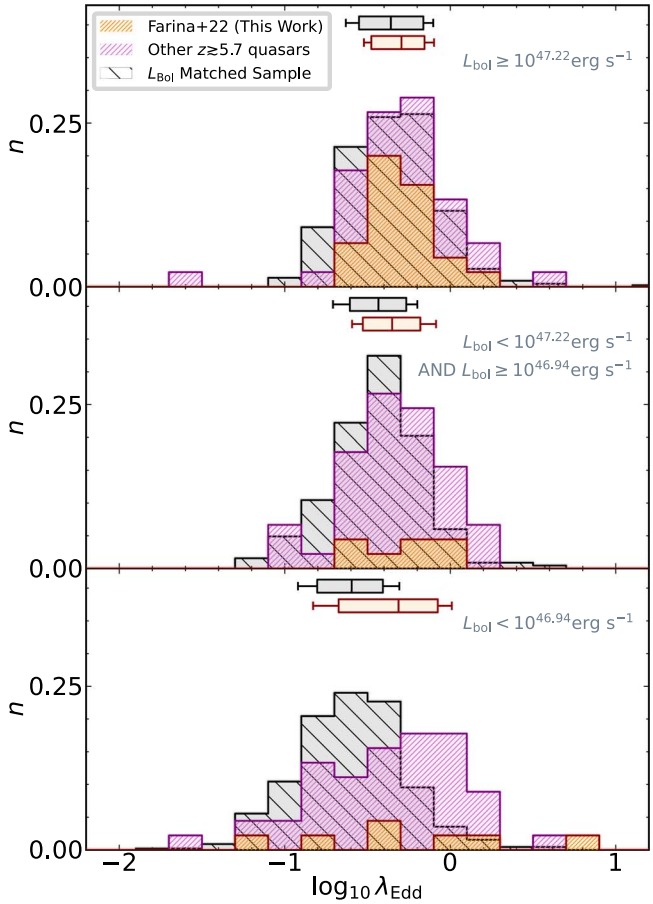

Figure 7. Eddington ratio distribution for the bright (top), intermediate (middle), and faint (bottom) samples of $z\gtrsim5.7$ quasars in this study. For comparison, the Eddington ratios of the luminosity-matched samples are also shown. The rectangles on the top of each panel mark the median values of the different distributions and show that high-redshift quasars have higher median accretion rates than the lower-redshift ones for all luminosity ranges. The color code is the same as in Figure 6.

$\lambda_{\rm Edd}>2.0$. All three have masses derived from the C IV line that are intrinsically less accurate[25] (see Section 4.2). Therefore, there is no clear evidence for a significant population of $5.7\lesssim z\lesssim7.6$ quasars accreting at super-Eddington rates. However, one should keep mind that accretion disk models predict that, at luminosities approaching Eddington, advective energy transport dominates over radiative cooling, causing the Eddington ratio to *saturate* at $\lambda_{\rm Edd}\gtrsim3$ (Abramowicz et al. 1988; Watarai et al. 2000; Sadowski 2009, 2011; Madau et al. 2014; Kubota & Done 2019; see also Jiang et al. 2019).

These findings are summarized in Figure 6, where we compare the Eddington ratio distribution of our *full sample* to the one of the bolometric luminosity-matched low-redshift quasars (excluding the ultraluminous quasar J0100+2802; see Section 5). In logarithmic space, both distributions are well fitted by a Gaussian function with a logarithmic dispersion of $\sim$0.3 (consistent with values reported by Mazzucchelli et al. 2017 and Shen et al. 2019). However, the median Eddington ratio of the control sample ($\lambda_{\rm Edd}=0.35^{+0.01}_{-0.01}$ with $p_{16\rm th}=0.17$ and $p_{84\rm th}=0.66$) is lower than the high-redshift value. We test the significance of this difference by performing a Kolmogorov–Smirnov test with bootstrap resampling over the two distributions. The derived p-value is 5.2×10^{-6} (8.1×10^{-8}, if we consider only masses derived from the Mg II line); this allows us to reject the null hypothesis that the two samples are drawn from the same distribution at the $\sim4.6\sigma$ ($\sim5.4\sigma$) level.

This difference could be driven by the intrinsic flux limit of high-redshift quasar searches (e.g., Malmquist 1922, 1925), which can translate into selecting more-massive black holes at fixed galaxy mass (e.g., Lauer et al. 2007) and into a bias toward objects with higher bolometric luminosities and, thus, higher Eddington ratios.[26] Given that quasars in the *full sample* come from different surveys with different depths (for instance the 5σ z-band magnitude limit of the Subaru High-z Exploration of Low-Luminosity Quasars survey is $z_{5\sigma}\sim25.1$ mag; Matsuoka et al. 2016, while that of Pan-STARRS1 is $z_{5\sigma}\sim22.1$ mag Bañados et al. 2016), one can naively expect that brighter quasars are impacted by this bias more. Figure 7 compares the logarithmic distributions of Eddington ratios of our full sample of high-redshift quasars split into three bins of bolometric luminosity, each containing the same number of objects. The median Eddington ratios of high-redshift quasars in these bins are: $\lambda_{\rm Edd}=0.47^{+0.13}_{-0.11}$ for the low-luminosity bin ($L_{\rm bol}<10^{46.94}$ erg s^{-1}), $0.45^{+0.08}_{-0.03}$ for the intermediate-luminosity bin ($10^{46.94}$ erg s$^{-1}\leqslant L_{\rm bol}<10^{47.22}$ erg s^{-1}), and $0.51^{+0.03}_{-0.05}$ for the high-luminosity bin ($L_{\rm bol}\geqslant10^{47.22}$ erg s^{-1}). The distribution of $\log_{10}\lambda_{\rm Edd}$ for low-luminosity quasars is slightly wider ($\sigma\sim0.45$) than for brighter quasars ($\sigma\sim0.29$ and ~0.26 for intermediate and bright objects, respectively). But the width

[25] A detailed discussion on J2229+1457, the quasar in the X–shooter /ALMA sample with the highest Eddington ration ($\lambda_{\rm Edd}\sim7.7$), is presented in Appendix A.

[26] This bias is, however, mitigated by the fact that both $L_{\rm bol}$ and $M_{\rm BH}$ are linearly proportional to the monochromatic luminosity of the quasar's $L_{\lambda,3000\text{Å}}$ (see Equations (1) and (2)).

of these distributions is broadly consistent with their corresponding low-redshift luminosity-matched samples ($\sigma \sim 0.31$, $\sigma \sim 0.25$, and $\sigma \sim 0.28$, for low-, intermediate-, and high-luminosity quasars, respectively). The broader distribution observed for in the high-redshift low-luminosity bin could be, partially, associated to intrinsically lower S/N of the spectra of faint quasars (e.g., Denney et al. 2009). It is however beyond the scope of the current study to fully settle this issue. In general, the median values of the Eddington ratios of the control samples ($\lambda_{\rm Edd} = 0.26^{+0.01}_{-0.01}$, $0.37^{+0.01}_{-0.02}$, and $0.44^{+0.02}_{-0.02}$ for the faint-, intermediate-, and high-luminosity-matched control samples, respectively) are consistently lower than the high-redshift ratios, independent of the luminosity bin, with the largest difference observed in the low-luminosity bin. This suggests that selection biases should not play a major role, and that $z \sim 6$ quasars at a given luminosity are actually accreting faster than their lower-redshift counterparts or that a nonvirial component contributes to the broadening of the BLR.

5.2. Is There an Evolution of Intrinsic Quasar Properties at z > 6.5?

The X-ray emission of luminous quasars is thought to originate from inverse Compton scattering of UV/optical photons produced by the accretion disk on a compact, hot corona surrounding the inner parts of the disk (e.g., Galeev et al. 1979; Haardt & Maraschi 1991; Svensson & Zdziarski 1994). Recent XMM-Newton, Chandra, Swift, and eRosita investigations of $z \sim 6$ quasars are providing insights into black hole accretion physics, complementing the UV emission-line observations (e.g., Ai et al. 2017; Nanni et al. 2017, 2018; Connor et al. 2019, 2020, 2021b; Pons et al. 2020; Medvedev et al. 2020, 2021; Khorunzhev et al. 2021).

Particular interest has been given to the intrinsic photon index of the ∼0.5–10 keV power-law continuum (Γ), because of its correlation with the Eddington ratio (e.g., Shemmer et al. 2008; Risaliti et al. 2009; Fanali et al. 2013). Studies of $z > 6.5$ quasars (e.g., Moretti et al. 2014; Page et al. 2014; Bañados et al. 2018a; Vito et al. 2019; Connor et al. 2021a) revealed an average photon index of $\Gamma = 2.32^{+0.31}_{-0.30}$ (Wang et al. 2021a). This is steeper than what is reported for bright quasars in the redshift range $1.5 \lesssim z \lesssim 4.5$ ($\Gamma = 1.92^{+0.09}_{-0.08}$; Just et al. 2007) and up to $z \sim 6$ ($\Gamma = 1.92^{+0.28}_{-0.27}$; Nanni et al. 2017). This steepening suggests that $z > 6.5$ quasars should be accreting faster (by a factor ∼20, if we take the face values of the steepening and the relation between hard X-ray spectral slope and the Eddington ratio derived by Risaliti et al. 2009, or by Brightman et al. 2013) than lower-redshift analogs (Wang et al. 2021a).

In Figure 8, we test if this evolutionary trend also appears in our sample of bright quasars. To ensure a uniform luminosity selection in the entire redshift range $5.7 \lesssim z \lesssim 7.6$, we consider only quasars brighter than $M_{1450} = -25.2$ mag (i.e., the characteristic magnitude of $z \sim 6$ quasars; e.g., Jiang et al. 2016; see Figure 1), and we exclude the hyperluminous quasar J0100+2802. The median properties are calculated in three, uniformly spaced, redshift bins centered at $z = 6.0$, 6.7, and 7.3 containing 60, 50, and 6 quasars, respectively. The median bolometric luminosities in these three bins all fall in the small range $L_{\rm bol} \sim 10^{47.1}$–$10^{47.2}$ erg s^{-1}, confirming that we are probing similarly luminous quasars at different redshifts. The median Eddington ratios in the three redshift bins ($\lambda_{\rm Edd} = 0.44^{+0.04}_{-0.06}$, $0.56^{+0.09}_{-0.07}$, and, $0.59^{+0.06}_{-0.12}$, at $z = 6.0$, 6.7, and 7.3, respectively) are marginally increased above $z \sim 6.5$ and are significantly higher than the median value in the $z \sim 2$ luminosity-matched sample ($\lambda_{\rm Edd} = 0.37^{+0.01}_{-0.01}$).

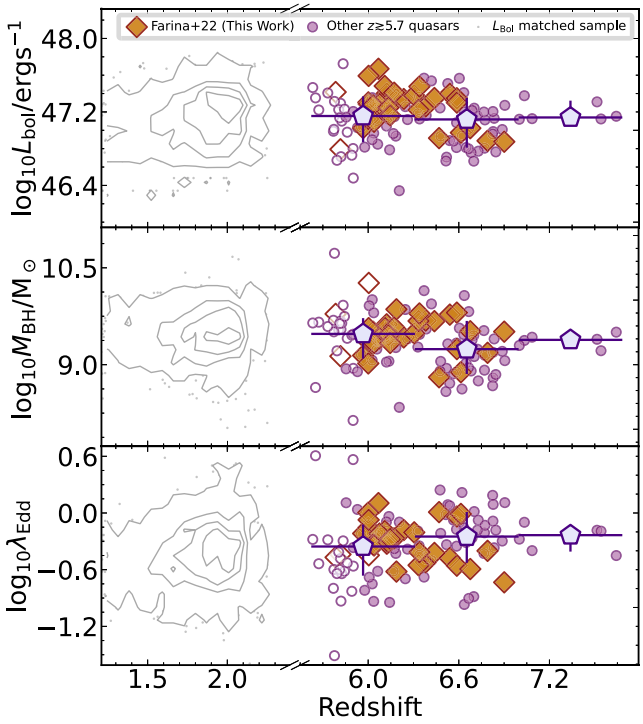

Figure 8. Redshift distribution of (from top to bottom) bolometric luminosities, black hole masses, and Eddington ratios for bright ($M_{1450} < -25.2$ mag) $z \gtrsim 5.7$ quasars (color coded as in Figure 5). Blue pentagons mark median values in three redshift bins. Error bars on the *y*-axis represent the 16th and the 84th percentiles of the distribution, while on the *x*-axis they indicate the size of the redshift bin. For comparison, the distribution of the luminosity-matched sample is also shown by gray contours.

Despite the different black hole mass estimators and fitting procedures used by Shen et al. (2019) and Yang et al. (2021), our findings are qualitatively compatible with their results. Using a sample of 50 quasars at $5.6 < z < 6.5$, Shen et al. (2019) reported Eddington ratios consistent with those of their luminosity-matched low-redshift sample, while Yang et al. (2021) showed an increase in accretion rates in a sample of 37 quasars at $6.3 < z < 7.7$ with respect to $0.4 < z < 2.1$ quasars with similar luminosity.

It is important to note that other properties of the luminous quasar population also evolve above $z \sim 6.5$. For instance, the number density of $M_{1450} < -26.0$ mag objects drops twice as fast from $z \sim 6$ to $z \sim 6.7$ than across the range $3 \lesssim z \lesssim 5$ (Wang et al. 2019b). The average blueshift of the broad C IV emission line relative to low-ionization lines rises significantly above $z \sim 6$ (Meyer et al. 2019; Yang et al. 2021, Paper I). The fraction of $z > 6.5$ BAL quasars increases to ∼24% compared to ∼15% at lower redshifts (Yang et al. 2021; Bischetti et al. 2022). Lastly, the fraction of $z \sim 6$ quasars showing weak emission lines (i.e., those with C IV rest-frame equivalent widths of $W_{\rm r}^{\rm CIV} < 10$ Å) appears to be higher than in bright SDSS quasars (e.g., Bañados et al. 2014; Shen et al. 2019).

These general evolutionary trends, however, are only marginally reflected in the changes in the accretion rate of reionization-era quasars, which merely increase by ∼0.1 dex from $z \sim 6$ to $z \sim 7$. This suggests that the steep Γ reported by Wang et al. (2021a), from the joint analysis of the X-ray spectra

of six $z \gtrsim 6.5$ quasars, cannot be explained by higher Eddington ratios alone.[27] Indeed, while the link between the X-ray spectral properties of quasars and the underlying accretion physics is now accepted, the details of these processes are still not well understood (e.g., Trakhtenbrot et al. 2017b). A larger sample of $z > 6.5$ quasars observed in the X-ray will be necessary to pin down the different actors contributing to the observed evolution of Γ at these high redshifts.

5.3. Constraints on the Formation of the First Massive Black Holes

The fiducial timescale of SMBH growth is the so-called Salpeter timescale ($t_{\rm Sal}$, Salpeter 1964). This is calculated by considering that the bolometric luminosity of a quasar's accretion disk can be related to the total mass inflow rate ($\dot{M}$) and, thus, the growth rate of the black hole ($\dot{M}_{\rm BH}$), following:

$$L_{\rm bol} = \epsilon \dot{M} c^2 = \frac{\epsilon}{1-\eta} \dot{M}_{\rm BH} c^2, \quad (4)$$

where η is the accretion *inefficiency* (i.e., the fraction of the total accreted mass/energy that is lost during the process) and ϵ is the radiative efficiency of black hole accretion. In the following, we will consider the case of radiatively efficient accretion events, so we will assume $\epsilon = \eta$. Combining Equation (1) with Equation (4) and taking the quasar's duty cycle ($f_{\rm duty}$) into account, one obtains:

$$\frac{M_{\rm BH}(t - t_0)}{M_{\rm BH}(t_0)} = \exp\left[f_{\rm duty} (1 - \epsilon) \lambda_{\rm Edd} \frac{t - t_0}{t_{\rm Sal}} \right], \quad (5)$$

where the Salpeter time is defined as:

$$t_{\rm Sal} = \epsilon \frac{\sigma_{\rm T} c}{4\pi G m_{\rm p}} \approx \epsilon \ 450 \ {\rm Myr}. \quad (6)$$

This value is calculated in the idealized case of pure hydrogen accretion. However, we can consider a more realistic case where the accreting gas has primordial abundances of hydrogen ($X = 0.75$) and helium ($Y = 0.25$; see, e.g., Cyburt et al. 2016, and references therein). Given that a helium atom has a mass of $\sim 4 \times m_{\rm p}$ and two free electrons, a quasar's Eddington luminosity will be a factor $1/(1 - Y/2) \approx 1.14$ higher, and thus, the Salpeter time will be correspondingly shortened to $t_{\rm Sal} \approx \epsilon \, 395$ Myr (see, also, Worseck et al. 2021). As noted by Mayer & Bonoli (2019), considering a plasma with higher metallicity has little impact on the mass growth timescale.

The radiative efficiency is a crucial quantity to determine the early growth of SMBHs. For individual quasars, ϵ will cover a range of values depending on different parameters such as black hole spin (e.g., Reynolds 2014, 2021; Capellupo et al. 2016) or optical depth of the accretion disk (e.g., Narayan & Yi 1995; Sadowski et al. 2014). For instance, Trakhtenbrot et al. (2017a) compared the expected emission of a thin accretion disk with the observed luminosities and black hole masses of 20 $z \sim 6$ quasars and obtained radiative efficiencies in the range $0.03 \lesssim \epsilon \lesssim 0.3$.

Following the bulk of the literature on $z \gtrsim 6$ quasars, here we assume a *universal* and constant value of $\epsilon = 0.1$. This is consistent with $\epsilon = 0.06$ calculated for a radiatively efficient, Shakura & Sunyaev thin-disk accretion model (with an upper limit of $\epsilon \lesssim 0.3$ for a maximally rotating Kerr black hole; e.g., Thorne 1974) and with constraints derived from the comparison between the total mass in SMBHs observed in the local universe and the integrated emission of all quasars over cosmic times (the so-called Soltan argument; e.g., Soltan 1982; Shankar et al. 2009).

Figure 9 shows the growth path of black hole seeds assuming maximal accretion ($\lambda_{\rm Edd} = 1$) for the entire history of the universe ($f_{\rm duty} = 1$). Under these conditions, the black hole seeds would have to have masses of $4 M_\odot \lesssim M_{\rm seed} \lesssim 2.7 \times 10^4 M_\odot$ at $z = 30$ to grow to the observed mass distribution at $z \gtrsim 6$ (see, e.g., Sassano et al. 2021, for a discussion on the redshifts of black hole seeds formation). In the following, we will briefly summarize the different scenarios that have been proposed to explain the formation of seeds with such masses. For a more complete overview on the topic, we direct the interested reader to the several excellent reviews on this topic from Volonteri (2010), Latif & Ferrara (2016), Inayoshi et al. (2020), Greene et al. (2020), and Trakhtenbrot (2020).

The *light-seeds* (with masses of up to a few hundred solar masses) scenario assumes that black hole progenitors are remnants of PopIII stars. These first stars are believed to form at $z \gtrsim 20$, when the limited cooling ability of the primordial gas leads to inefficient fragmentation, resulting in a top-heavy initial mass function with masses in the range 10–1000 $M_\odot$ (Abel et al. 2002; Karlsson et al. 2013; Hirano et al. 2014). While PopIII stars with masses 140–260 $M_\odot$ will explode as pair-instability supernovae and leave no remnants, those with masses $40-140 \, M_\odot$ and $>260 \, M_\odot$ will collapse into black holes containing at least half of the progenitor mass (e.g., Fryer et al. 2001; Heger et al. 2003). These *light-seeds* are expected to form in the highest peaks of the primordial density field and, thus, will cluster in the cores of the most-massive halos at high redshift (e.g., Madau & Rees 2001; Volonteri et al. 2003).

However, as shown by Figure 9, it is unattainable that these PopIII remnants could grow to $\gtrsim 10^9 \, M_\odot$ by $z \gtrsim 6.5$. Even considering that, for their entire life (i.e., $f_{\rm duty} = 1$), they accrete gas at a rate close to the Eddington limit and with low values of $\epsilon \lesssim 0.1$ (Haiman & Loeb 2001; Tanaka & Haiman 2009). Such conditions are unlikely to be met in the early universe. Strong feedback from the progenitor stars, from supernovae, and from the accretion onto the black hole seeds is expected to act within the shallow gravitational potential wells of the first galaxies, reducing the available gas for accretion (e.g., Mori et al. 2002; Johnson & Bromm 2007; Pelupessy et al. 2007).

These requirements can be relaxed with short episodes of moderately super-Eddington accretion (e.g., Madau et al. 2014; Lupi et al. 2016; Pacucci et al. 2017; Jiang et al. 2019). Or, if the gas can efficiently lose angular momentum, even with hyper-Eddington accretion (e.g., Volonteri & Rees 2005; Tanaka & Haiman 2009; Inayoshi et al. 2016). Such accretion events would accelerate the growth in mass of, initially, small black hole seeds by orders of magnitude within a few million years. We stress that while our data shows Eddington ratios of $\lambda_{\rm Edd} \lesssim 1$ for all quasars with black hole masses derived from the Mg II line (see Section 4.3), it does not rule out such a scenario. It does, however, put some constraints on it. If the first quasars do violate the Eddington limit, our results imply that this should only happen mildly, and/or at earlier cosmic

[27] Note that all quasars in Wang et al. (2021a) are part of our *full sample*.

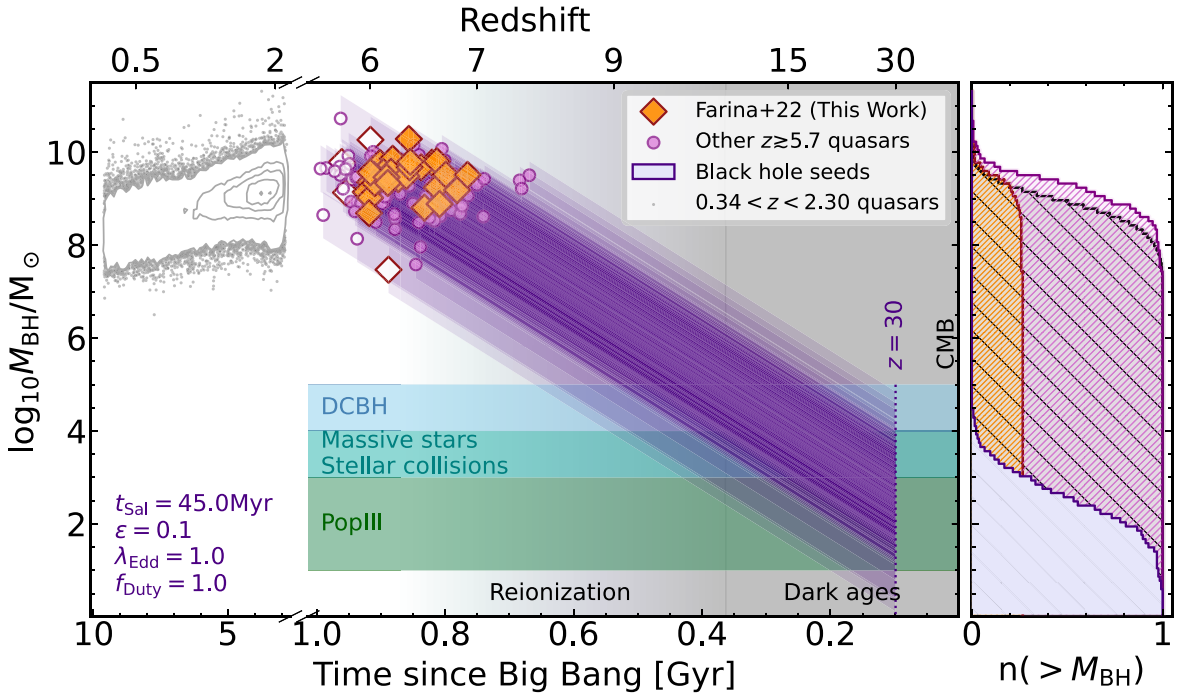

Figure 9. Evolutionary tracks of black hole seeds (purple lines) to reach the observed quasar masses at $z \sim 6$ (orange diamonds and pink circles). These are calculated using Equation (5) with parameters: $f_{\rm duty} = 1$, $\epsilon = 0.1$, $\lambda_{\rm Edd} = 1$, and $t_{\rm Sal} = 45$ Myr. Mass ranges for different black hole seed formation scenarios are indicated by shaded regions. For the sake of comparison, gray contours and points indicate the location of $1.3 < z < 2.3$ SDSS DR7 quasars (Shen et al. 2011). In the right panel, we show the cumulative distributions of observed black holes (orange and pink for the $z \sim 6$ quasars, and black for the $0.34 < z < 2.30$ quasars) and expectations for the considered evolutionary pathway starting at $z = 30$ (purple).

times, and/or for a short period of time, and/or in an highly obscured phase (e.g., Kelly & Shen 2013).

Alternatively, the necessity of a rapid and continuous accretion could be mitigated if the progenitors of the first quasars are born directly as more-massive seeds. One scenario to form such massive seeds is through stellar collisions. It has been proposed that the first episodes of efficient star formation are able to foster the formation of very compact nuclear star clusters in metal-poor proto-galaxies. In these environments, direct collisions can occur on timescales shorter than the lifetime of massive stars (Portegies Zwart & McMillan 2002; Portegies Zwart et al. 2004) and can lead to the formation of a supermassive star that could potentially leave a black hole remnant with a mass in the range $\sim 10^2$–$10^4\,M_\odot$ (Devecchi & Volonteri 2009).

Finally, it has also been suggested that even more-massive seeds can form at $z \lesssim 15$ through the direct monolithic collapse of low angular momentum massive gas clouds, resulting in supermassive stars that will promptly end their life in black holes with masses around $\sim 10^4$–$10^5\,M_\odot$ (Oh & Haiman 2002; Koushiappas et al. 2004; Begelman et al. 2006; Lodato & Natarajan 2006; Mayer et al. 2010; Mayer & Bonoli 2019). Several studies have investigated the (rare) physical conditions necessary for the formation of these so-called direct collapse black holes (DCBH; e.g., Visbal et al. 2014; Habouzit et al. 2016; Woods et al. 2019). For instance, it has been proposed that fragmentation (which would deter the formation of massive seeds) can be prevented by the dissociation of H_2 molecules (the main cooling channel in the young universe) by a strong Lyman–Werner radiation field (e.g., Bromm & Loeb 2003; Latif et al. 2015; Luo et al. 2020). The necessary radiation could originate from nearby highly star-forming galaxies (e.g., Regan et al. 2017) or from heated gas and shocks induced by gas-rich major mergers (e.g., Mayer et al. 2010), which could simultaneously facilitate the black hole growth, triggering $\gtrsim 1000 M_\odot\,{\rm yr}^{-1}$ gas inflows (e.g., Mayer & Bonoli 2019).

It is important to note that the limits on the mass of the black hole seeds set by our sample are strongly influenced by the choice of the physical parameters used in Equation (5). For example, the tension between the short formation time and the high mass of the quasar black holes can be eased if we consider that the presence of primordial helium can shorten the Salpeter time to $t_{\rm Sal} \approx \epsilon\, 395$ Myr and that the radiative efficiency calculated for a Shakura & Sunyaev thin disk is $\epsilon = 0.06$[28] (Shakura & Sunyaev 1973; see the top panel of Figure 15 in Appendix C). On the other hand, if we can also take into account that the median observed Eddington ratio of $z > 5.7$ quasars is $\lambda_{\rm Edd} \sim 0.47$ (see Section 5.1) and that clustering measurements suggest a duty cycle of $f_{\rm duty} = 0.03 - 0.60$ for bright $z \sim 4$ quasars (e.g., Shen et al. 2007; White et al. 2008), implying $f_{\rm duty} \sim 0.9$ at $z \sim 6$ (e.g., Shankar et al. 2010). Using these values, Equation (5) predicts that black hole seeds need to have masses as high as $\sim 10^5\,M_\odot$ at $z = 30$ (see the bottom panel of Figure 15 in Appendix C).

5.4. The Earliest Supermassive Black Holes and Their Hosts

For all quasars in our X-shooter/ALMA sample, submillimeter ALMA data has been collected (see Venemans et al. 2017b, 2019; Decarli et al. 2018, 2019a; Bañados et al. 2019; Eilers et al. 2020; Venemans et al. 2020; Neeleman et al. 2021; Walter et al. 2022, for details). These observations revealed bright [C II] 158 μm line emission in 34 out of 38 quasars, with luminosities typically in the

[28] Even lower values of $\epsilon \sim 0.008$–0.010 (below the range allowed by the thin-disk model) have been derived by Davies et al. (2019) from the impact of the ionizing flux of two $z > 7$ quasars on the surrounding neutral IGM.

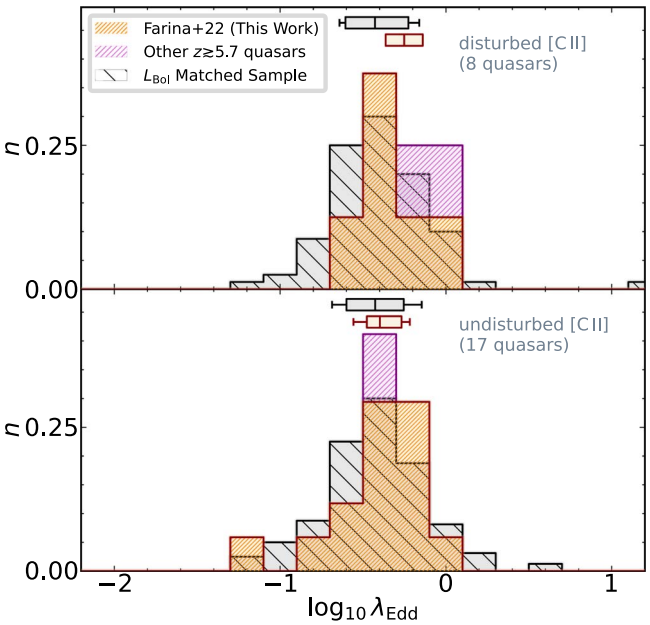

Figure 10. Logarithmic Eddington ratio distributions of the quasars observed at $<0\farcs25$ resolution with ALMA by Neeleman et al. (2021). Host galaxies that show disturbed and undisturbed [C II] 158 μm morphologies are shown in the upper and lower panels, respectively. For the sake of comparison, the Eddington ratios of the luminosity-matched samples are also shown in black. However, note that no information on the hosts is taken into account for the selection of the $z\sim0.3-2.3$ quasars. The box plots at the top of each panel mark the median values of the various distributions. High-redshift quasars residing in galaxies with a disturbed morphology have a median Eddington ratio higher than those in undisturbed hosts. However, the two distribution do not differ enough to suggest differences between their parent populations. The color code is the same as in Figure 6.

range of 10^9–$10^{10}\,L_\odot$. The data also revealed the presence of large quantities of dust with masses of 10^7–$10^9\,M_\odot$ (as derived from the far-IR, FIR, luminosities ranging from $\sim0.3\times10^{11}\,L_\odot$ to $\sim13\times10^{13}\,L_\odot$[29]; e.g., Venemans et al. 2018). In addition, using $<0\farcs25$ (corresponding to <1.4 kpc at $z=6$) ALMA imaging of the [C II] 158 μm line emission of quasar host galaxies, Neeleman et al. (2021) inferred dynamical masses ($M_{\rm Dyn}$) of the order of ~1–$10\times10^{10}\,M_\odot$. The authors also reported that $\sim30\%$ of hosts show a disturbed [C II] 158 μm morphology, possibly due to a recent merger or interaction with close companions (see also Decarli et al. 2017, 2019a, 2019b; Willott et al. 2017; Bañados et al. 2019; Mazzucchelli et al. 2019; Neeleman et al. 2019; Venemans et al. 2019; Meyer et al. 2022b). In what follows, we examine these properties in light of our comprehensive analysis of the proprieties of the black holes in the first quasars.

5.4.1. Merger Signatures and Quasar Activity

If gravitational interactions between gas-rich galaxies are able to induce strong gas inflows (e.g., Barnes & Hernquist 1991, 1996) that trigger quasar activity (e.g., Di Matteo et al. 2005; Hopkins & Quataert 2010), then host galaxies with a disturbed morphology should naively have, on average, higher accretion rates. Indeed, merger signatures are expected to be detectable for $\lesssim2.4\times(1+z)^{-2}$ Gyr (Snyder et al. 2017; Lupi et al. 2022), a time much longer than current constraints on $z\sim6$ quasar lifetimes ($t_{\rm Q}\sim10^6$ yr, based on the measurements of their proximity zones; e.g., Eilers et al. 2017, 2021; Davies et al. 2020; Morey et al. 2021; see also Khrykin et al. 2019; Worseck et al. 2021). Even when considering that the gas perturbed by the merger event may take several dynamical times ($t_{\rm dyn}\sim4\times10^6$ yr for the typical host in our sample) to funnel down to the central regions of a galaxy (e.g., Solanes et al. 2018), the ensuing peak of quasar activity can be delayed by $\gtrsim$100 Myr (e.g., Di Matteo et al. 2005).

Figure 10 shows the logarithmic distribution of the Eddington ratios divided into disturbed and undisturbed morphology of the host galaxy, as classified by Neeleman et al. (2021). Galaxies with a disturbed morphology harbor black holes accreting at a median Eddington ratio of $\lambda_{\rm Edd}=0.56^{+0.09}_{-0.10}$. At first glance, this appears to be higher than the remaining sample (with a median Eddington ratio of $\lambda_{\rm Edd}=0.40^{+0.07}_{-0.02}$). However, a Student's t-test (Student 1908) on the two samples returns a p-value ~0.15. Thus, the two median values are not statistically different ($\sim1.4\sigma$).

This suggests that the growth of a $z\sim6$ black hole is not strongly affected by merger events, or that the peak of black hole activity may occur during an obscured phase (e.g., Di Matteo et al. 2012; Dubois et al. 2013; Trebitsch et al. 2019; Davies et al. 2019). It is worth noting that these findings echo results from deep HST/WFC3 observations of the hosts of bright ($L_{\rm bol}\gtrsim4\times10^{46}\,{\rm erg\,s^{-1}}$) and massive ($M_{\rm BH}\gtrsim3\times10^8\,M_\odot$) quasars at $z\sim2$. Indeed, these investigations also revealed merger features in $\sim25\%$ of the cases and no clear link between accretion rates and disturbed stellar morphologies (e.g., Mechtley et al. 2016; Marian et al. 2019). However, the importance of merger in triggering the black hole activity will become more relevant at later cosmic times ($z<0.2$; e.g., Marian et al. 2020).

5.4.2. The Black Hole-to-galaxy Mass Ratio

Despite similarities in accretion and host galaxy properties across redshifts, it has been noted since the first resolved detection of the CO emission of a $z>6$ quasar host galaxy (SDSS J1148+5251 at $z=6.42$; Walter et al. 2003, 2004) that, when compared to local measurements of the $M_{\rm BH}$–$M_{\rm Bulge}$ relation (e.g., Häring & Rix 2004; Kormendy & Ho 2013; Graham 2016; de Nicola et al. 2019), the black holes of the first quasars are over-massive relative to their hosts.

This was recently confirmed by Neeleman et al. (2021) with a large sample of bright quasars, using the black hole masses estimated in this work. In Figure 11, we further reinforce these findings by complementing their results with all available estimates of dynamical masses of $z\gtrsim5.7$ hosts from the literature (Willott et al. 2015, 2017; Izumi et al. 2018, 2019, 2021; Pensabene et al. 2020). For unresolved observations (Willott et al. 2013; Mazzucchelli et al. 2017; Decarli et al. 2018; Yang et al. 2019b; Eilers et al. 2020; Andika et al. 2020; Wang et al. 2021a; Khusanova et al. 2022), we additionally include estimates of the host galaxy masses by using the relations between $M_{\rm Dyn}$ and FWHM and size of the [C II] 158 μm emitting region (where published) provided by Neeleman et al. (2021).

The median $M_{\rm BH}/M_{\rm Dyn}$ ratio of the 52 quasars with available [C II] 158 μm data is ~0.038. This is a factor of $\gtrsim10\times$ larger than the median $M_{\rm BH}/M_{\rm Bulge}$ ratio of the 66 local galaxies with precise black hole and bulge masses derived by Savorgnan

[29] The FIR luminosities of $z\sim6$ quasars are typically calculated assuming that the dust spectral energy distribution is described by a modified blackbody with temperature $T_{\rm dust}=47$ K and an emissivity index $\beta=1.6$ (e.g., Beelen et al. 2006; Leipski et al. 2014; Venemans et al. 2016)

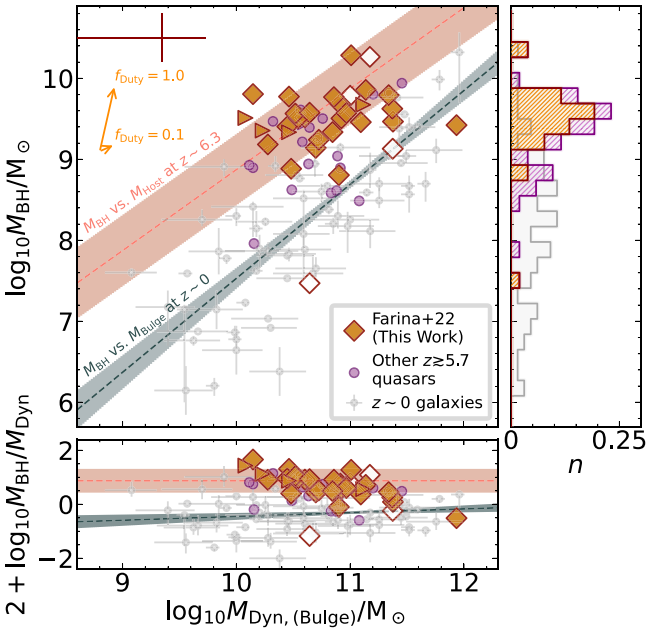

Figure 11. Relation between the dynamical mass of the host galaxies and the mass of the central black holes of the $z\gtrsim5.7$ quasars for the X–shooter/ALMA sample (orange diamonds, with right pointing orange triangles indicating lower limits; see also Neeleman et al. 2021) and for other studies (violet circles). The typical error (including systematics) is shown as a cross in the top-left corner. For comparison, the best fit of the relation between M_{BH} and M_{Bulge} derived by Kormendy & Ho (2013) is shown as a gray dashed line. The extrapolation of the M_{BH}/M_{Host} ratio evolution derived by Decarli et al. (2010b) for $z\sim6.3$ (the median redshift of the quasar sample) is shown as an orange dashed line. Light-gray points are data for 66 local galaxies derived by Savorgnan et al. (2016). The bottom panel highlights the differences with respect to the local relation by re-scaling the y-axis by a factor of 100. Histograms in the right panel show the black hole mass distributions for local galaxies (in gray) and for high-redshift quasars (in orange and pink).

et al. (2016). The M_{BH}/M_{Dyn} ratios of $z\gtrsim5.7$ quasars are broadly consistent with the $z\sim6.3$ (the median redshifts of the considered quasars) extrapolation of the M_{BH}–M_{Host} evolution presented by Decarli et al. (2010b; see also Peng et al. 2006; Merloni et al. 2010).

Note that these comparisons are based on the working assumptions that dynamical masses and bulge (or stellar) masses are comparable (but see, e.g., Lupi et al. 2019) and that biases due to the sample selection function are negligible (but see, e.g., Lauer et al. 2007). While the direct detection of the stellar light of high-redshift quasars with JWST will quantify the consequences of the first assumption (e.g., Marshall et al. 2021), we can already (partially) estimate the impact of the latter. If we split the sample into two bins of bolometric luminosity, both containing the same number of objects, we observe that quasars with $L_{bol}>1.4\times10^{47}$ erg s^{-1} have a median M_{BH}–M_{Dyn} ratio of ∼0.056, which is a factor of $\sim2\times$ higher than the median value for the remainder of the sample ($M_{BH}/M_{Dyn}\sim0.025$). While this indicates that fainter quasars also lie, on average, above the local M_{BH}–M_{Bulge} relation, the lower mass ratio observed in the fainter quasar bin suggests that selection biases may indeed play a major role in shaping the observed evolution of the relation (e.g., Willott et al. 2017; Izumi et al. 2021, and Marshall et al. 2020b for results from cosmological hydrodynamical simulations).

5.5. The First Black Holes and Their Gas Reservoirs

Our X–shooter /ALMA sample largely overlaps (20 out of 38 targets) with the REQUIEM survey, a VLT/MUSE survey of high-redshift quasars presented by Farina et al. (2019; see also Farina et al. 2017 and Drake et al. 2019). This study probed the extended Lyα emission surrounding $z\sim6$ quasars on scales of several kiloparsecs. While these halos are routinely detected around $z\gtrsim2$ quasars (e.g., Borisova et al. 2016; Arrigoni Battaia et al. 2019; Cai et al. 2019; Farina et al. 2019; Drake et al. 2020; Fossati et al. 2021), the physical mechanisms that power their observed emission remain uncertain. The currently favored scenarios include a combination of emission from collisionally excited gas and recombination radiation produced after quasar photoionization, and/or scattering of Lyα photons from the BLR (e.g., Hennawi & Prochaska 2013; Arrigoni Battaia et al. 2015; Farina et al. 2017; Cantalupo 2017; Cantalupo et al. 2019; Costa et al. 2022). Nonetheless, all of these mechanisms require the presence of large amounts of cool ($T<10^4$ K) gas. Thus, the detection of Lyα nebulae around $z\gtrsim6$ quasars is an indication of the presence of large (possibly $\gtrsim10^{10}\,M_{\odot}$) gas reservoirs that are able to simultaneously sustain the intense star formation rates of the hosts and feed the black hole.[30]

Bearing in mind that obscuration, variations in the quasar activity, the presence of additional sources of ionizing radiation, and the specific density distribution of the emitting material can each influence the intensity of Lyα emission, we will assume, for the sake of simplicity, that the brightest Lyα nebulae trace the most-massive gas reservoirs. Given that inflow of cold gas is expected to be the main driver of the early and rapid growth of the first quasars (e.g., Di Matteo et al. 2012; Dubois et al. 2013), one can expect that the most-massive and highly accreting quasars are surrounded by the most luminous Lyα nebulae.

In Figure 12, we plot M_{BH} and λ_{Edd} as a function of the luminosity of the Lyα halo ($L_{Ly\alpha}^{Halo}$). If we split the sample into two bins at a halo luminosity of $L_{Ly\alpha}^{Halo}=10^{43}$ erg s^{-1} (a limit set by the typical depth of the VLT/MUSE observations in Farina et al. 2019), we observe no major difference in the median black hole masses ($M_{BH}=3.1^{+1.3}_{-0.9}\times10^9\,M_{\odot}$ and $3.1^{+0.7}_{-1.3}\times10^9\,M_{\odot}$, for faint and bright halos, respectively). We see a mild (but low significance, i.e., ∼0.7σ obtained from a Student's t-test on the two samples) increase in the median Eddington ratio with halo luminosity ($\lambda_{Edd}=0.45^{+0.08}_{-0.07}$ for faint halos and $0.62^{+0.28}_{-0.08}$ for bright halos). While the absence of correlation between the cool gas reservoirs and black hole properties might seem surprising, we stress that both the REQUIEM and the X–shooter /ALMA surveys preferentially target UV-bright quasars (see Section 2). Thus, we have biased our study to a narrow Eddington ratio and black hole mass range, with only three quasars that have $M_{BH}<5\times10^8\,M_{\odot}$. A sample of faint quasars with reliable black hole mass estimates and a sensitive investigation of the extended emission would be necessary to further test for the presence of correlations.

5.5.1. Are the First Black Holes and Their Dark Matter Halos Linked?

The presence of a correlation between M_{BH} and the mass of the dark matter halo host has been a matter of discussion since

[30] We remind the reader that the minimum timescale for cold gas in the halo to reach the black hole is the freefall time, estimated to be ≳50 Myr.

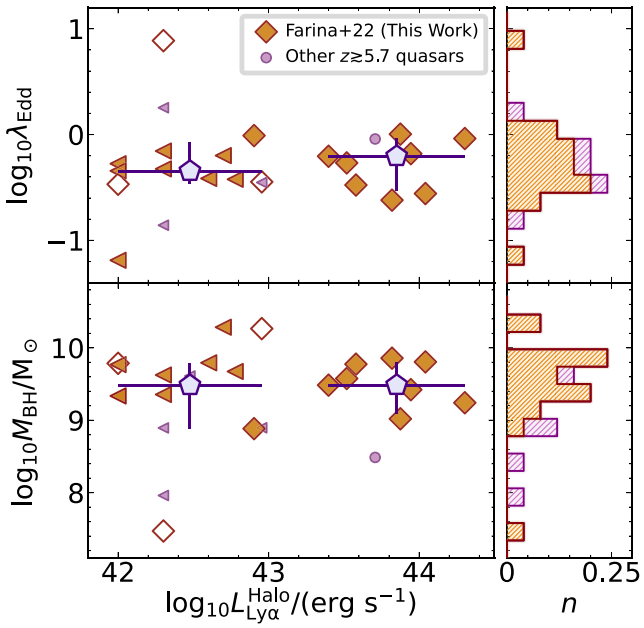

Figure 12. Black hole masses (bottom) and Eddington ratios (top) of quasars from the X–shooter /ALMA sample (20 targets) and from the literature (five targets) as a function of total *Lyα* luminosity of the extended halo. The color code of the points is the same as in Figure 5, and left pointing triangles indicate upper limits on the Lyα halo luminosities. Median values calculated after splitting the sample at a halo luminosity of 10^{43} erg s^{-1} are shown as blue pentagons. The 16th and 84th percentiles of the distribution are shown as error bars along the *y*-axis. Error bars along the *x*-axis indicate the luminosity range covered by each bin. Histograms in the right panel show the distribution of black hole masses and Eddington ratios considered.

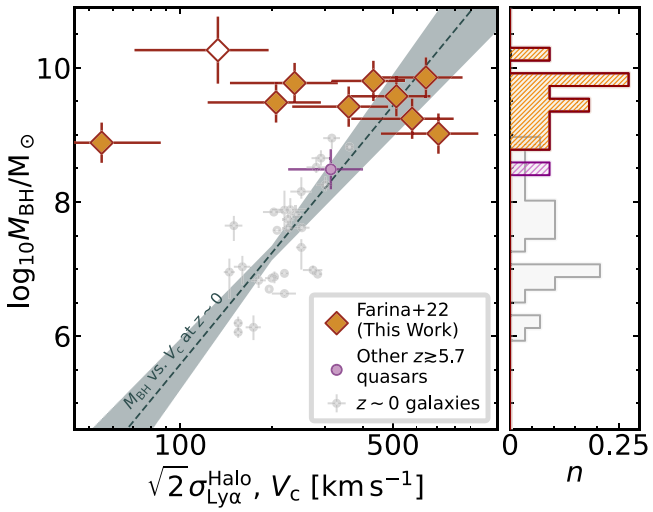

Figure 13. Distribution of $z \gtrsim 5.7$ quasars in the circular velocity vs. black hole mass plane. Circular velocities are derived from the 1D velocity dispersion of the Lyα halos considering $V_c = \sqrt{2}\,\sigma_{Ly\alpha}^{Halo}$. Black hole masses and circular velocities for local galaxies are taken from the review of Kormendy & Ho (2013; gray points). The gray dashed line is the best fit to the $z \sim 0$ data following the procedure in Volonteri et al. (2011). Histograms in the right panel show the distribution of black hole masses of the high-redshift and local samples. The color code is the same as in Figure 11.

it has been first proposed by Ferrarese (2002). Given the smaller scatter of this relation, it has been argued that it is more fundamental than relations with other host galaxy properties (e.g., Baes et al. 2003; Marasco et al. 2021). However, the level of the scatter including different galaxy populations and the strength of the correlation has been put into question by several studies (e.g., Kormendy & Bender 2011; Kormendy & Ho 2013; Sabra et al. 2015). Volonteri et al. (2011) proposed that the relation between SMBHs and dark matter halos should be tighter at early cosmic times, when the growth is expected to be dominated by the merger history of the host galaxy (see Section 5.3). Dynamical measurements of the mass of dark matter halos (M_h) of single galaxies commonly rely on globular cluster kinematics and/or spatially resolved H I rotation curves. Thus, testing this prediction at high redshift is observationally challenging (e.g., Sun et al. 2013). And currently there are no direct measurements of the circular velocity (V_c) of the halo of $z \gtrsim 6$ quasars (for indirect estimates see, e.g., Shimasaku & Izumi 2019).

However, we can obtain a coarse estimate of V_c under the assumption that the extended Lyα emission traces gas in gravitational motion within the dark matter halo. Using this, we can derive the circular velocity from the kinematic information of the Lyα extended emission, considering $V_c = \sqrt{2}\ \sigma_{Ly\alpha}^{Halo}$ (where $\sigma_{Ly\alpha}^{Halo}$ is the measured 1D rms velocity dispersion of the halo; e.g., Tormen et al. 1997). This is supported by simulations showing that in massive high-redshift halos, the dark matter component dominates the kinematics at scales larger than ∼10 kpc (Costa et al. 2015). It is also supported by observations of the quiescent kinematics of the extended Lyα emission (e.g., Arrigoni Battaia et al. 2019; Farina et al. 2019; Drake et al. 2022; Lau et al. 2022) and, more in general, of the gas residing in the CGM of quasar (e.g., Prochaska & Hennawi 2009; Lau et al. 2018), with large velocity dispersions (>200 km s^{-1}), potentially associated with outflows, observed only in the closest regions to the quasar hosts (e.g., Guo et al. 2020).

In Figure 13, we compare our rough estimates of the velocity dispersion with those of local galaxies, as presented in Kormendy & Ho (2013). Despite the large scatter, most of the quasars sit on the high velocity–high mass extrapolation of the best fit of the local relation (see Volonteri et al. 2011, for details), especially when bearing in mind that our sample is highly biased toward massive objects. In general, the observed velocities are consistent with gravitational motions within a dark matter halo with masses $M_{DM} \gtrsim 10^{12.5}\,M_\odot$. The first quasars are indeed expected to reside in such massive halos. Indeed, the number density of $M_{1450} < -26$ mag quasars (the typical quasar part of the REQUIEM survey), $\phi(M_{1450} < -26\ \mathrm{mag}) \sim 7 \times 10^{-10}$ cMpc^{-3} (using the estimates of Matsuoka et al. 2018b), matches the integral of the $z \sim 6.3$ halo mass function from Behroozi et al. (2013) at a mass of $M_{DM} \sim 10^{12.8}\,M_\odot$, if we assume an high duty cycle of $f_{duty} = 0.9$ (see Section 5.3 and, e.g., Shankar et al. 2010). The tentative results are, thus, that the Lyα emitting gas in the CGM is bound by gravitation and that local relation holds out to high redshifts.

The onset of this relation at early cosmic time supports a scenario where the rapid formation of the first quasars happens in the rarest peaks of the initial distribution of density fluctuations, meaning that the quasars are hosted by the most-massive dark matter halos at that time (e.g., Volonteri 2012), although these halos may evolve at later times into less extreme systems (e.g., Angulo et al. 2012; Fanidakis et al. 2013; Tenneti et al. 2018).

There are, however, several potential systematics associated with our approach. For one, resonant scattering could lead to a

strong modification of the spectral shape of the Lyα line (e.g., Dijkstra 2017; Costa et al. 2022), making the determination of the true gas kinematics less reliable. This would imply that measurements of the circular velocity from the Lyα extended emission are an overestimate of the true kinematics (up to a factor $\sim$1.5$\times$; e.g., Costa et al. 2022), and thus that the black holes in $z\sim6$ quasars are over-massive with respect to their dark matter halos. Detection of nonresonant line emission from the CGM (e.g., Cantalupo et al. 2019; Guo et al. 2020) with JWST will be able to mitigate these systematics. In addition, the presence of companion galaxies at small separations from the quasar hosts may perturb the gas. This may be the case for the largest outlier in Figure 13: the quasar J0305–3150 at $z\sim6.6$ with a peculiarly narrow extended emission (Farina et al. 2019). The presence of a close-by companion located in the same direction of the halo may suggest that the Lyα line is not tracing the kinematics of the halo, but rather the gas perturbed by the close interaction (Farina et al. 2017).

6. Summary and Conclusions

We present black hole masses and Eddington ratios obtained from deep (typically 2 hr per target) near–IR X–shooter spectroscopy of 38 bright quasars at $5.78<z<7.54$. Our data are complemented by ALMA observations of the [C II] 158 μm emission (providing information on the host galaxies) and VLT/MUSE sensitive searches of the extended Lyα emission (providing insight into the cool gas reservoirs). This is the second paper in a series aimed at inferring the general properties of bright quasars during the epoch of reionization. In Paper I, we investigated the properties of the quasar BLRs, showing an increase in the blueshift of the C IV emission lines with respect to low-redshift quasar samples. Here, we calculate accurate black hole masses and Eddington ratios derived primarily from the Mg II broad emission line. After including data from the literature, we compiled a sample of 38 + 97 quasars at $5.7\lesssim z\lesssim7.6$. The main results from the study of this large sample of bright quasars are:

(i)—High-redshift quasars are powered by massive ($M_{\rm BH}\gtrsim10^8\,M_\odot$), strongly accreting black holes (with a median Eddington ratio of $\lambda_{\rm Edd}=0.48$). While $z\gtrsim5.7$ quasars sit in a similar locus in the bolometric luminosity versus black hole mass plane as a luminosity-matched sample of $z\lesssim2.3$ quasars, their accretion rates are, on average, $\sim$0.2 dex larger. The data also tentatively suggests a mild evolution of the median accretion rate from $z\sim6$ to $z\sim7$.

(ii)—Only three quasars show $\lambda_{\rm Edd}\gg1$. However, all of them have black hole masses derived from the C IV broad emission line. We interpret this as caused by the larger intrinsic uncertainties associated with this line, instead of owing to underlying physical processes. Thus, we have no strong evidence of a significant population of quasars accreting at super-Eddington.

(iii)—When compared with local studies, the black holes appear to be over-massive with respect to their host galaxy masses derived from the [C II] emission line. There is no evidence for changing accretion behavior with a more or less perturbed morphology, for example, caused by a merger of the host galaxy.

(iv)—The extent of the reservoirs of cool ($T\sim10^4$ K) gas within the halo of the quasars does not correlate with the accretion rate of the $10^9\,M_\odot\lesssim M_{\rm BH}\lesssim10^{10}\,M_\odot$ central black holes.

Given these findings, we can speculate on the fate of the first quasars. The first SMBHs appear to already be as massive as the most-massive quasars at $z\sim0.3$–2.3, more than 2 Gyr later (see Figure 5). It seems that the rapid black hole growth required at early times (shown in Figure 9) is strongly reduced for the remainder of the universe's history. Instead, the host galaxy needs to continue forming stars to grow its mass and move toward the local $M_{\rm BH}$–$M_{\rm Dyn}$ relation (see Figure 11). Such stellar mass growth can be sustained by the cool gas reservoirs discussed in Section 5.5 (e.g., Walter et al. 2020).

In Figure 11, we illustrate the evolution of the typical quasar in our sample. It has a black hole mass of $3\times10^9\,M_\odot$, an accretion rate of $\lambda_{\rm Edd}=0.48$, and a host galaxy mass of $7\times10^{10}\,M_\odot$ with a dust-obscured star formation rate of $\sim220\,M_\odot\,{\rm yr}^{-1}$. This quasar would move across the $M_{\rm BH}$—$M_{\rm Dyn}$ plane as indicated by the larger orange arrow, if we assume that its growth continues uninterrupted ($f_{\rm duty}=1.0$) for 100 Myr (roughly corresponding to the depletion timescale for star formation). Under these conditions, the SMBH will overgrow its host galaxy even further, moving the quasar away from the local relation. Given that other accretion properties of the quasar population appear to be constant with redshift, this implies that the duty cycle of quasars needs to drastically evolve. For instance, if the duty cycle is reduced to $f_{\rm duty}\lesssim0.1$ (indicated by the shorter orange arrow), the relative growth in mass of the black hole would be smaller than that of the host, pushing the quasar in the direction of the local relation (e.g., Trakhtenbrot et al. 2011).

This study showcases the critical role of combining data from different wavelengths and instruments to derive constraints on the physical properties of the first SMBHs. Systematic uncertainties described in this work could be conceivably reduced in the near future. JWST (Gardner et al. 2006) will provide precise black hole mass and Eddington ratio estimates via rest-frame optical investigation of the first quasars. Complementarily, Euclid is expected to push quasar searches to fainter objects and higher redshifts (e.g., Euclid Collaboration et al. 2019), reducing the impact of selection biases.

E.P.F. is grateful to V. Springel and M. Strauss for the hospitality at MPA and at Princeton University while writing this manuscript. It is a pleasure to thank M. Strauss, J. Green, and M. Neeleman for discussion, comments, and suggestions that helped improving this paper. E.P.F., F.W., M.O., R.A.M., and S.E.I.B. acknowledge funding through the ERC Advanced grant 740246 (*Cosmic Gas*). A.C.E., T.A.G., and F.W. acknowledge support by NASA through the NASA Hubble Fellowship grants (Nos. HF2-51434, HF2-51480, and HF2-51448, respectively) awarded by the Space Telescope Science Institute, which is operated by the Association of Universities for Research in Astronomy, Inc., for NASA, under contract NAS5-26555. J.F.H. acknowledges support from the National Science Foundation under grant No. 1816006. J.T.S. and J.F.H. acknowledge funding through the ERC European Research Council (ERC) under the European Union's Horizon 2020 research and innovation program (grant agreement No. 885301). B.T. acknowledges support from the Israel Science Foundation (grant No. 1849/19) and from the European Research Council (ERC) under the European Union's Horizon 2020 research and innovation program (grant agreement No. 950533). A.B.D. acknowledges support from the UK Science and Technology Facilities Council (STFC) under grant ST/V000624/1. E.P.F. is supported by the international Gemini

Observatory, a program of NSF's NOIRLab, which is managed by the Association of Universities for Research in Astronomy (AURA) under a cooperative agreement with the National Science Foundation, on behalf of the Gemini partnership of Argentina, Brazil, Canada, Chile, the Republic of Korea, and the United States of America.

Based on observations made with ESO Telescopes at the La Silla or Paranal Observatories under program ID(s): 60.A-9418 (A), 084.A-0360(A), 084.A-0390(A), 085.A-0299(A), 086.A-0162(A), 087.A-0890(A), 088.A-0897(A), 089.A-0814(A), 091.C-0934(B), 093.A-0707(A), 096.A-0095(A), 096.A-0418 (A), 096.A-0418(B), 097.B-1070(A), 098.B-0537(A), 0100.A-0625(A), 0100.A-0898(A), 0101.B-0272(A), 0102.A-0154(A), and 286.A-5025(A).

Software: ASTROPY (Astropy Collaboration et al. 2013, 2018), IPYTHON (Perez & Granger 2007), MATPLOTLIB (Hunter 2007), NUMPY (van der Walt et al. 2011; Harris et al. 2020), PYPEIT (Prochaska et al. 2019a, 2019b, 2020), PYTHON (van Rossum & Drake 1995, 2009), SCIPY (Virtanen et al. 2020), and SCULPTOR (Schindler 2022).

Appendix A
The Small Black Hole of J2229+1457

The $z = 6.15$ quasar J2229+1457 appears as an outlier in Figure 5. This is the faintest quasar of the X–shooter /ALMA sample, with a bolometric luminosity of 2.9×10^{46} erg s^{-1} and a C IV–based black hole mass of only $3 \times 10^7\,M_\odot$. For comparison, similarly faint high-redshift quasars typically have black hole masses at least 1 order of magnitude more massive (see, e.g., Willott et al. 2010b; Onoue et al. 2019). This could imply that this quasar is accreting at a rate higher than Eddington, with $\lambda_{\rm Edd} \sim 7.7$ (see Table 4).

The low mass estimate originates from the shape of the C IV line, which consists of a narrow (driving the measured relatively small $\mathrm{FWHM_{CIV}} \sim 900$ km s^{-1}) and a broad distinct component (see Figure 3, row 4, panel 3). Unfortunately, the quasar's redshift puts the Mg II line in a spectral region strongly affected by telluric absorption. Therefore, the Mg II measurements should be taken with caution. Eilers et al. (2020) measured an $\mathrm{FWHM_{MgII}} = (5469 \pm 439)$ km s^{-1} from the X–shooter spectrum of this object, resulting in a black hole mass estimate of $M_{\rm BH} \sim 1.7 \times 10^9\,M_\odot$ (and an Eddington ratio of $\lambda_{\rm Edd} \sim 0.1$). Willott et al. (2010b) deduced $\mathrm{FWHM_{MgII}} = (1440 \pm 330)$ km s^{-1}, $M_{\rm BH} \sim 1.4 \times 10^8\,M_\odot$, and $\lambda_{\rm Edd} \sim 1.6$. from their measurements on low-resolution ($R \sim 520$) Gemini/NIRI spectroscopy.

Super-Eddington accretion episodes are often invoked to explain the rapid mass buildup of the first SMBHs (e.g., Volonteri & Rees 2005; see also Section 5.3 for details), and this object could be an example of such accretion, especially considering that this is a potentially *young* quasar (Eilers et al. 2017). However, the large uncertainties on C IV–based black hole masses (of the order of ∼0.5 dex; see Section 4.2) do not allow us to derive solid conclusions based on this single object.

Appendix B
Comparison with Shen et al.

Shen et al. (2019) presented black hole masses and Eddington ratios for a sample of 50 quasars at $z > 5.7$. Data have been gathered with GNIRS on Gemini-North, which has a spectral resolution of $R \sim 650$ (i.e., a factor ∼10× lower than X–shooter). There are five quasars in common between ours and the Shen et al. (2019) sample: P007+04, J0842+1218, J1044−0125, J1148+0702, and J2310+1855. While the overlap is small, it is worth investigating if any significant discrepancy arises due to the different S/Ns, resolutions, and fitting techniques. Figure 14 summarizes the comparison. Our measurements of the line FWHMs are on average ∼130 km s^{-1} (for Mg II) and ∼610 km s^{-1} (for C IV) smaller than that measured by Shen et al. (2019). The corresponding black hole masses are thus marginally larger but consistent within the uncertainties.

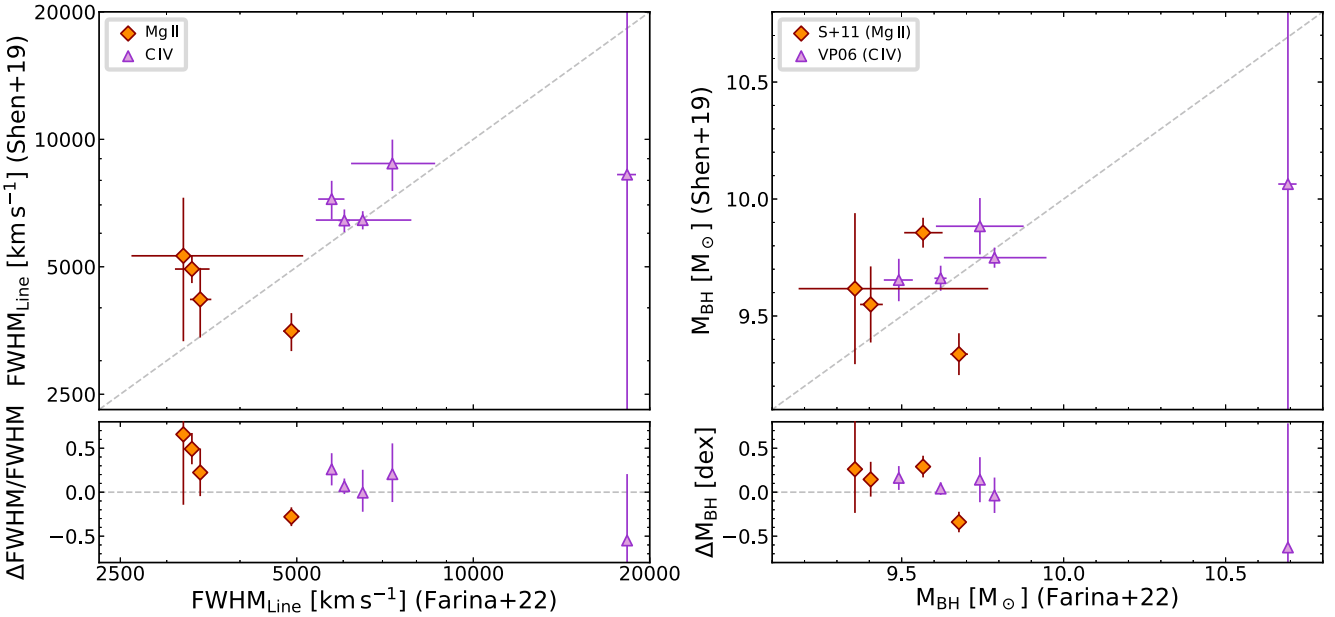

Figure 14. Comparison of FWHM measurements of the Mg II (orange diamonds) and C IV (purple triangles) lines (left panel) and black hole mass estimates (right panel) for the five quasars in common between our X–shooter sample and that of Shen et al. (2019). The relative differences between two measurements are showed in the bottom panels.

Appendix C
Supermassive Black Holes Seeds with Different Parameters

In Figure 15 we show the different paths for the black hole seed from redshift $z = 30$ to the observed masses at $z \sim 6$–7. In the following examples, we plug into Equation (5) a Salpeter time of $t_{\rm Sal} \approx \epsilon\, 395$ Myr (estimated considering the presence of primordial helium) and a radiative efficiency of $\epsilon = 0.06$. The two panels show two different cases: the top panel shows maximally accreting black holes ($\lambda_{\rm Edd} \sim 1.0$) for the entire history of the universe ($f_{\rm duty} = 1.0$); and the bottom panel shows a more conservative scenario with $\lambda_{\rm Edd} \sim 0.48$ (the median value observed for $z \sim 6$ quasars) and a duty cycle of $f_{\rm duty} = 0.9$.

Appendix D
Quasars with Mg II–based Black Hole Masses

In Table 5 we provide a summary of Mg II black hole mass estimates for $z \gtrsim 5.7$ quasars from the literature. All measurements are converted to the cosmology used in this paper. Unless otherwise specified, the iron pseudo-continuum has been fitted using the Vestergaard & Wilkes (2001) template.

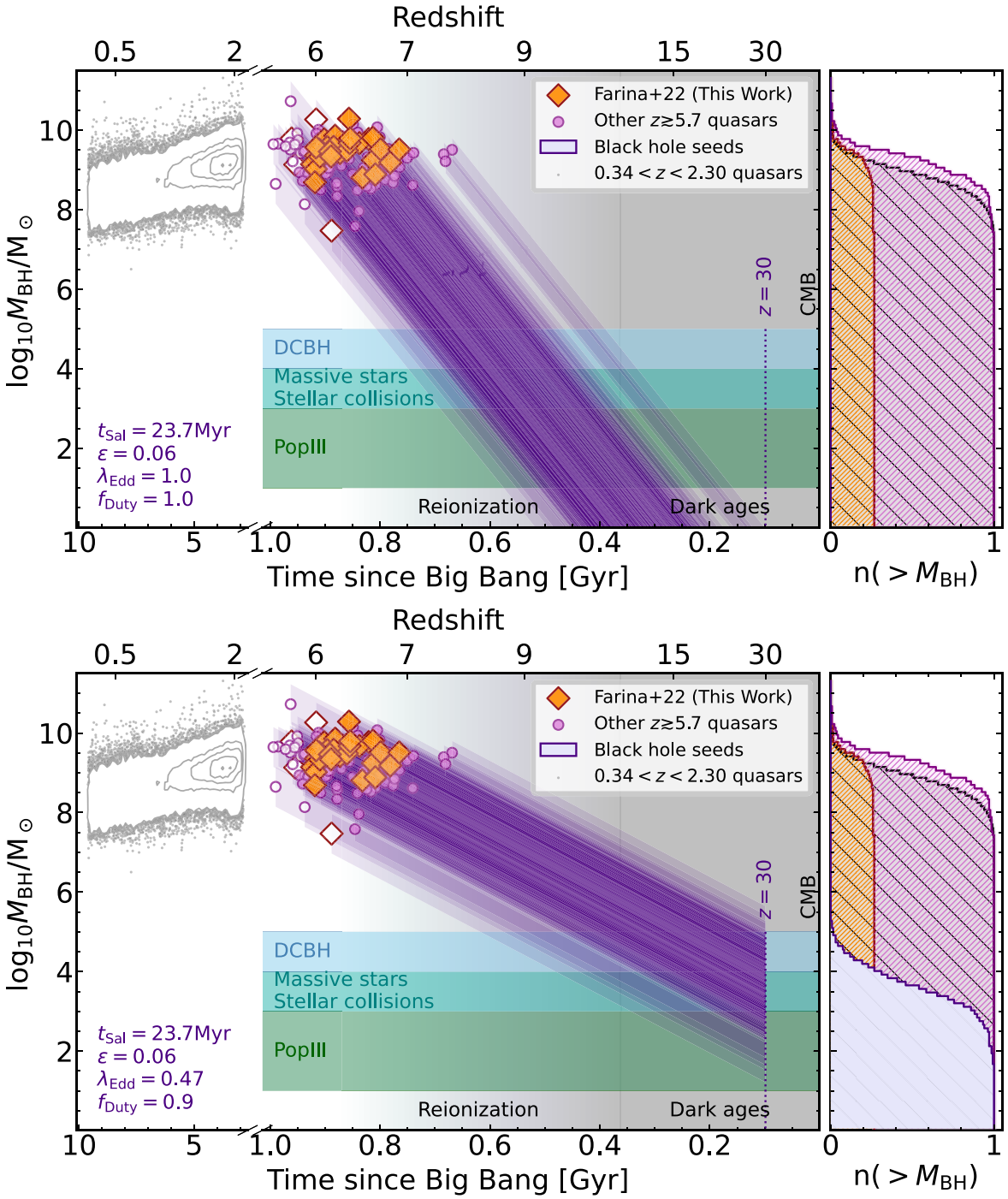

Figure 15. Same as Figure 9 but for different black hole growth parameters.

Table 5
List of Quasars with Mg II–based Black Hole Masses

ID	R.A. (J2000)	Decl. (J2000)	z_{sys}	z_{sys} Method	M_{1450} (mag)	FWHM$_{MgII}$ (km s^{-1})	3000 Å $L_{\lambda,3000Å}$ (10^{46} erg s^{-1})	L_{bol} (10^{46} erg s^{-1})	M_{BH}^{S+11} (10^9 $M_\odot$)	λ_{Edd}^{S+11}	Ref.
J0008−0626	00:08:25.77	−06:26:04.6	5.929 ± 0.006	C III]	−26.32	2279^{+274}_{-274}	$2.07^{+0.01}_{-0.01}$	10.68	0.78	1.09	Shen et al. (2019)
J0020−3653	00:20:31.47	−36:53:41.8	6.834 ± 0.0004	Mg II	−26.92	3800^{+360}_{-360}	$2.62^{+0.05}_{-0.05}$	13.49	2.51	0.43	Reed et al. (2019)
J0024+3913	00:24:29.77	+39:13:19.0	6.621 ± 0.002	[CII] 158 μm	−25.65	1783^{+38}_{-38}	$1.69^{+0.15}_{-0.15}$	8.70	0.42	1.65	Yang et al. (2021)
P007+04	00:28:06.56	+04:57:25.7	6.0015 ± 0.0002	[CII] 158 μm	−26.51	3203^{+1925}_{-591}	$3.91^{+0.13}_{-0.16}$	20.13	2.27	0.70	Farina et al. (2022)
J0033−0125	00:33:11.40	−01:25:24.9	6.019 ±0.007	Mg II	−25.14	6762^{+6808}_{-6808}	$0.63^{+0.01}_{-0.01}$	3.24	3.28	0.08	Shen et al. (2019)
J0038−1527	00:38:36.10	−15:27:23.6	7.034 ±0.0003	[CII] 158 μm	−27.13	3102^{+45}_{-45}	$4.62^{+0.19}_{-0.19}$	23.79	2.37	0.80	Yang et al. (2021)
P011+09	00:45:33.57	+09:01:57.0	6.4694 ±0.0025	[CII] 158 μm	−25.87	2238^{+744}_{-373}	$1.60^{+0.03}_{-0.03}$	8.22	0.64	1.02	Farina et al. (2022)

Note. No iron pseudo-continuum has been subtracted in the estimates from Chehade et al. (2018). Measures from Wang et al. (2021a), Andika et al. (2020), and Matsuoka et al. (2019) have been derived from a combination of the Vestergaard & Wilkes (2001) and the Tsuzuki et al. (2006) iron templates, while those from Willott et al. (2010b) from the McLure & Dunlop (2004) one. This table is available in its entirety in machine-readable format. Only a portion is shown here for guidance regarding its form and content.

Reference. Andika et al. (2020), Chehade et al. (2018), De Rosa et al. (2011), Farina al. (2022) , Matsuoka et al. (2019), Mazzucchelli et al. (2017), Onoue et al. (2019), Reed et al. (2019), Shen et al. (2019), Wang et al. (2021a), Willott et al. (2010b), and Yang et al. (2021)

(This table is available in its entirety in machine-readable form.)

ORCID iDs

Emanuele Paolo Farina https://orcid.org/0000-0002-6822-2254
Jan-Torge Schindler https://orcid.org/0000-0002-4544-8242
Fabian Walter https://orcid.org/0000-0003-4793-7880
Eduardo Bañados https://orcid.org/0000-0002-2931-7824
Frederick B. Davies https://orcid.org/0000-0003-0821-3644
Roberto Decarli https://orcid.org/0000-0002-2662-8803
Anna-Christina Eilers https://orcid.org/0000-0003-2895-6218
Xiaohui Fan https://orcid.org/0000-0003-3310-0131
Joseph F. Hennawi https://orcid.org/0000-0002-7054-4332
Chiara Mazzucchelli https://orcid.org/0000-0002-5941-5214
Romain A. Meyer https://orcid.org/0000-0001-5492-4522
Benny Trakhtenbrot https://orcid.org/0000-0002-3683-7297
Marta Volonteri https://orcid.org/0000-0002-3216-1322
Feige Wang https://orcid.org/0000-0002-7633-431X
Gábor Worseck https://orcid.org/0000-0003-0960-3580
Jinyi Yang https://orcid.org/0000-0001-5287-4242
Thales A. Gutcke https://orcid.org/0000-0001-6179-7701
Bram P. Venemans https://orcid.org/0000-0001-9024-8322
Sarah E. I. Bosman https://orcid.org/0000-0001-8582-7012
Tiago Costa https://orcid.org/0000-0002-6748-2900
Gisella De Rosa https://orcid.org/0000-0003-3242-7052
Alyssa B. Drake https://orcid.org/0000-0002-0174-3362
Masafusa Onoue https://orcid.org/0000-0003-2984-6803

References

Abel, T., Bryan, G. L., & Norman, M. L. 2002, Sci, 295, 93
Abramowicz, M. A., Czerny, B., Lasota, J. P., & Szuszkiewicz, E. 1988, ApJ, 332, 646
Ai, Y., Fabian, A. C., Fan, X., et al. 2017, MNRAS, 470, 1587
Allen, J. T., Hewett, P. C., Maddox, N., Richards, G. T., & Belokurov, V. 2011, MNRAS, 410, 860
Andika, I. T., Jahnke, K., Onoue, M., et al. 2020, ApJ, 903, 34
Angulo, R. E., Springel, V., White, S. D. M., et al. 2012, MNRAS, 425, 2722
Arrigoni Battaia, F., Hennawi, J. F., Prochaska, J. X., et al. 2019, MNRAS, 482, 3162
Arrigoni Battaia, F., Hennawi, J. F., Prochaska, J. X., & Cantalupo, S. 2015, ApJ, 809, 163
Astropy Collaboration, Price-Whelan, A. M., Sipőcz, A. M., et al. 2018, AJ, 156, 123
Astropy Collaboration, Robitaille, T. P., Tollerud, E. J., et al. 2013, A&A, 558, A33
Baes, M., Buyle, P., Hau, G. K. T., & Dejonghe, H. 2003, MNRAS, 341, L44
Bañados, E., Connor, T., Stern, D., et al. 2018a, ApJL, 856, L25
Bañados, E., Mazzucchelli, C., Momjian, E., et al. 2021, ApJ, 909, 80
Bañados, E., Novak, M., Neeleman, M., et al. 2019, ApJL, 881, L23
Bañados, E., Venemans, B. P., Decarli, R., et al. 2016, ApJS, 227, 11
Bañados, E., Venemans, B. P., Mazzucchelli, C., et al. 2018b, Natur, 553, 473
Bañados, E., Venemans, B. P., Morganson, E., et al. 2014, AJ, 148, 14
Barnes, J. E., & Hernquist, L. 1996, ApJ, 471, 115
Barnes, J. E., & Hernquist, L. E. 1991, ApJL, 370, L65
Baskin, A., & Laor, A. 2005, MNRAS, 356, 1029
Beelen, A., Cox, P., Benford, D. J., et al. 2006, ApJ, 642, 694
Begelman, M. C., Volonteri, M., & Rees, M. J. 2006, MNRAS, 370, 289
Behroozi, P. S., Wechsler, R. H., & Conroy, C. 2013, ApJ, 770, 57
Bennert, V. N., Auger, M. W., Treu, T., Woo, J.-H., & Malkan, M. A. 2011, ApJ, 742, 107
Bentz, M. C., Denney, K. D., Grier, C. J., et al. 2013, ApJ, 767, 149
Bentz, M. C., Peterson, B. M., Netzer, H., Pogge, R. W., & Vestergaard, M. 2009, ApJ, 697, 160
Bentz, M. C., Peterson, B. M., Pogge, R. W., Vestergaard, M., & Onken, C. A. 2006, ApJ, 644, 133
Bischetti, M., Feruglio, C., D'Odorico, V., et al. 2022, Natur, 605, 244
Bonning, E. W., Shields, G. A., & Salviander, S. 2007, ApJL, 666, L13
Borisova, E., Cantalupo, S., Lilly, S. J., et al. 2016, ApJ, 831, 39
Brightman, M., Silverman, J. D., Mainieri, V., et al. 2013, MNRAS, 433, 2485
Bromm, V., & Loeb, A. 2003, ApJ, 596, 34
Cai, Z., Cantalupo, S., Prochaska, J. X., et al. 2019, ApJS, 245, 23
Calderone, G., Boutsia, K., Cristiani, S., et al. 2019, ApJ, 887, 268
Cantalupo, S. 2017, in Gas Accretion onto Galaxies, Astrophysics and Space Science Library, Vol. 430, ed. A. Fox & R. Davé (Cham: Springer), 195
Cantalupo, S., Pezzulli, G., Lilly, S. J., et al. 2019, MNRAS, 483, 5188
Capellupo, D. M., Netzer, H., Lira, P., Trakhtenbrot, B., & Mejía-Restrepo, J. 2016, MNRAS, 460, 212
Chehade, B., Carnall, A. C., Shanks, T., et al. 2018, MNRAS, 478, 1649
Clough, S. A., Iacono, M. J., & Moncet, J.-L. 2014, LBLRTM: Line-By-Line Radiative Transfer Model, Astrophysics Source Code Library, ascl:1405.001
Clough, S. A., Shephard, M. W., Mlawer, E. J., et al. 2005, JQSRT, 91, 233
Coatman, L., Hewett, P. C., Banerji, M., et al. 2017, MNRAS, 465, 2120
Coatman, L., Hewett, P. C., Banerji, M., & Richards, G. T. 2016, MNRAS, 461, 647
Connor, T., Bañados, E., Mazzucchelli, C., et al. 2020, ApJ, 900, 189
Connor, T., Bañados, E., Stern, D., et al. 2019, ApJ, 887, 171
Connor, T., Bañados, E., Stern, D., et al. 2021a, ApJ, 911, 120
Connor, T., Stern, D., Bañados, E., & Mazzucchelli, C. 2021b, ApJL, 922, L24
Costa, T., Arrigoni Battaia, F., Farina, E. P., et al. 2022, MNRAS, 517, 1767
Costa, T., Sijacki, D., & Haehnelt, M. G. 2015, MNRAS, 448, L30
Cyburt, R. H., Fields, B. D., Olive, K. A., & Yeh, T.-H. 2016, RvMP, 88, 015004
Davies, F. B., Hennawi, J. F., Bañados, E., et al. 2018, ApJ, 864, 143
Davies, F. B., Hennawi, J. F., & Eilers, A.-C. 2019, ApJL, 884, L19
Davies, F. B., Hennawi, J. F., & Eilers, A.-C. 2020, MNRAS, 493, 1330
de Nicola, S., Marconi, A., & Longo, G. 2019, MNRAS, 490, 600
De Rosa, G., Decarli, R., Walter, F., et al. 2011, ApJ, 739, 56
De Rosa, G., Fausnaugh, M. M., Grier, C. J., et al. 2018, ApJ, 866, 133
De Rosa, G., Peterson, B. M., Ely, J., et al. 2015, ApJ, 806, 128
De Rosa, G., Venemans, B. P., Decarli, R., et al. 2014, ApJ, 790, 145
Decarli, R., Dotti, M., Bañados, E., et al. 2019a, ApJ, 880, 157
Decarli, R., Falomo, R., Treves, A., et al. 2010a, MNRAS, 402, 2441
Decarli, R., Falomo, R., Treves, A., et al. 2010b, MNRAS, 402, 2453
Decarli, R., Mignoli, M., Gilli, R., et al. 2019b, A&A, 631, L10
Decarli, R., Pensabene, A., Venemans, B., et al. 2022, A&A, 662, A60
Decarli, R., Walter, F., Venemans, B. P., et al. 2017, Natur, 545, 457
Decarli, R., Walter, F., Venemans, B. P., et al. 2018, ApJ, 854, 97
Denney, K. D., Peterson, B. M., Dietrich, M., Vestergaard, M., & Bentz, M. C. 2009, ApJ, 692, 246
Devecchi, B., & Volonteri, M. 2009, ApJ, 694, 302
Di Matteo, T., Khandai, N., DeGraf, C., et al. 2012, ApJL, 745, L29
Di Matteo, T., Springel, V., & Hernquist, L. 2005, Natur, 433, 604
Dietrich, M., Hamann, F., Appenzeller, I., & Vestergaard, M. 2003, ApJ, 596, 817
Dijkstra, M. 2017, arXiv:1704.03416
Ding, X., Silverman, J., Treu, T., et al. 2020, ApJ, 888, 37
Drake, A. B., Farina, E. P., Neeleman, M., et al. 2019, ApJ, 881, 131
Drake, A. B., Neeleman, M., Venemans, B. P., et al. 2022, ApJ, 929, 86
Drake, A. B., Walter, F., Novak, M., et al. 2020, ApJ, 902, 37
Dressler, A. 1989, in IAU Symp. 134, Active Galactic Nuclei, ed. D. E. Osterbrock & J. S. Miller (Dordrecht: Kluwer), 217
Dubois, Y., Pichon, C., Devriendt, J., et al. 2013, MNRAS, 428, 2885
Eddington, A. S. 1926, The Internal Constitution of the Stars (Cambridge: Cambridge Univ. Press)
Eilers, A.-C., Davies, F. B., Hennawi, J. F., et al. 2017, ApJ, 840, 24
Eilers, A.-C., Hennawi, J. F., Davies, F. B., & Simcoe, R. A. 2021, ApJ, 917, 38
Eilers, A.-C., Hennawi, J. F., Decarli, R., et al. 2020, ApJ, 900, 37
Euclid Collaboration, Barnett, R., Warren, S. J., et al. 2019, A&A, 631, A85
Fan, X., Narayanan, V. K., Lupton, R. H., et al. 2001, AJ, 122, 2833
Fan, X., Strauss, M. A., Becker, R. H., et al. 2006, AJ, 132, 117
Fan, X., Strauss, M. A., Schneider, D. P., et al. 2003, AJ, 125, 1649
Fan, X., Wang, F., Yang, J., et al. 2019, ApJL, 870, L11
Fan, X., White, R. L., Davis, M., et al. 2000, AJ, 120, 1167
Fanali, R., Caccianiga, A., Severgnini, P., et al. 2013, MNRAS, 433, 648
Fanidakis, N., Macciò, A. V., Baugh, C. M., Lacey, C. G., & Frenk, C. S. 2013, MNRAS, 436, 315
Farina, E. P., Arrigoni-Battaia, F., Costa, T., et al. 2019, ApJ, 887, 196
Farina, E. P., Venemans, B. P., Decarli, R., et al. 2017, ApJ, 848, 78
Fasano, G., & Franceschini, A. 1987, MNRAS, 225, 155

Ferrarese, L. 2002, ApJ, 578, 90
Ferrarese, L., & Merritt, D. 2000, ApJL, 539, L9
Fossati, M., Fumagalli, M., Lofthouse, E. K., et al. 2021, MNRAS, 503, 3044
Fryer, C. L., Woosley, S. E., & Heger, A. 2001, ApJ, 550, 372
Galeev, A. A., Rosner, R., & Vaiana, G. S. 1979, ApJ, 229, 318
Gallerani, S., Maiolino, R., Juarez, Y., et al. 2010, A&A, 523, A85
Gardner, J. P., Mather, J. C., Clampin, M., et al. 2006, SSRv, 123, 485
Gebhardt, K., Bender, R., Bower, G., et al. 2000, ApJL, 539, L13
Graham, A. W. 2016, in Galactic Bulges, Astrophysics and Space Science Library, Vol. 418, ed. E. Laurikainen, R. F. Peletier, & D. A. Gadotti (Cham: Springer), 263
GRAVITY Collaboration, Amorim, A., Brandner, W., et al. 2020, A&A, 643, A154
GRAVITY Collaboration, Sturm, E., Dexter, J., et al. 2018, Natur, 563, 657
Greene, J. E., Strader, J., & Ho, L. C. 2020, ARA&A, 58, 257
Grier, C. J., Shen, Y., Horne, K., et al. 2019, ApJ, 887, 38
Guo, Y., Maiolino, R., Jiang, L., et al. 2020, ApJ, 898, 26
Haardt, F., & Maraschi, L. 1991, ApJL, 380, L51
Habouzit, M., Volonteri, M., Latif, M., Dubois, Y., & Peirani, S. 2016, MNRAS, 463, 529
Haiman, Z., & Loeb, A. 2001, ApJ, 552, 459
Häring, N., & Rix, H.-W. 2004, ApJL, 604, L89
Harris, C. R., Millman, K. J., van der Walt, S. J., et al. 2020, Natur, 585, 357
Heger, A., Fryer, C. L., Woosley, S. E., Langer, N., & Hartmann, D. H. 2003, ApJ, 591, 288
Hennawi, J. F., & Prochaska, J. X. 2013, ApJ, 766, 58
Hewett, P. C., & Wild, V. 2010, MNRAS, 405, 2302
Hirano, S., Hosokawa, T., Yoshida, N., et al. 2014, ApJ, 781, 60
Homayouni, Y., Trump, J. R., Grier, C. J., et al. 2020, ApJ, 901, 55
Hopkins, P. F., & Quataert, E. 2010, MNRAS, 407, 1529
Horne, K. 1986, PASP, 98, 609
Hunter, J. D. 2007, CSE, 9, 90
Inayoshi, K., Haiman, Z., & Ostriker, J. P. 2016, MNRAS, 459, 3738
Inayoshi, K., Visbal, E., & Haiman, Z. 2020, ARA&A, 58, 27
Izumi, T., Matsuoka, Y., Fujimoto, S., et al. 2021, ApJ, 914, 36
Izumi, T., Onoue, M., Matsuoka, Y., et al. 2019, PASJ, 71, 111
Izumi, T., Onoue, M., Shirakata, H., et al. 2018, PASJ, 70, 36
Jahnke, K., & Macciò, A. V. 2011, ApJ, 734, 92
Jiang, L., Fan, X., Annis, J., et al. 2008, AJ, 135, 1057
Jiang, L., McGreer, I. D., Fan, X., et al. 2015, AJ, 149, 188
Jiang, L., McGreer, I. D., Fan, X., et al. 2016, ApJ, 833, 222
Jiang, Y.-F., Stone, J. M., & Davis, S. W. 2019, ApJ, 880, 67
Johnson, J. L., & Bromm, V. 2007, MNRAS, 374, 1557
Just, D. W., Brandt, W. N., Shemmer, O., et al. 2007, ApJ, 665, 1004
Karlsson, T., Bromm, V., & Bland-Hawthorn, J. 2013, RvMP, 85, 809
Kashikawa, N., Ishizaki, Y., Willott, C. J., et al. 2015, ApJ, 798, 28
Kaspi, S., Brandt, W. N., Maoz, D., et al. 2007, ApJ, 659, 997
Kaspi, S., Brandt, W. N., Maoz, D., et al. 2021, ApJ, 915, 129
Kaspi, S., Maoz, D., Netzer, H., et al. 2005, ApJ, 629, 61
Kaspi, S., Smith, P. S., Netzer, H., et al. 2000, ApJ, 533, 631
Kelly, B. C., & Shen, Y. 2013, ApJ, 764, 45
Kelson, D. D. 2003, PASP, 115, 688
Khorunzhev, G. A., Meshcheryakov, A. V., Medvedev, P. S., et al. 2021, AstL, 47, 123
Khrykin, I. S., Hennawi, J. F., & Worseck, G. 2019, MNRAS, 484, 3897
Khusanova, Y., Bañados, E., Mazzucchelli, C., et al. 2022, A&A, 664, A39
Knigge, C., Scaringi, S., Goad, M. R., & Cottis, C. E. 2008, MNRAS, 386, 1426
Kolmogorov, A. 1933, Inst. Ital. Attuari, Giorn, 4, 83
Kormendy, J., & Bender, R. 2011, Natur, 469, 377
Kormendy, J., & Gebhardt, K. 2001, in AIP Conf. Ser. 586, 20th Texas Symp. on Relativistic Astrophysics, ed. J. C. Wheeler & H. Martel (Melville, NY: AIP), 363
Kormendy, J., & Ho, L. C. 2013, ARA&A, 51, 511
Kormendy, J., & Richstone, D. 1995, ARA&A, 33, 581
Koushiappas, S. M., Bullock, J. S., & Dekel, A. 2004, MNRAS, 354, 292
Kubota, A., & Done, C. 2019, MNRAS, 489, 524
Kulkarni, G., Worseck, G., & Hennawi, J. F. 2019, MNRAS, 488, 1035
Lai, S., Bian, F., Onken, C. A., et al. 2022, MNRAS, 513, 1801
Latif, M. A., Bovino, S., Grassi, T., Schleicher, D. R. G., & Spaans, M. 2015, MNRAS, 446, 3163
Latif, M. A., & Ferrara, A. 2016, PASA, 33, e051
Lau, M. W., Hamann, F., Gillette, J., et al. 2022, MNRAS, 515, 1624
Lau, M. W., Prochaska, J. X., & Hennawi, J. F. 2018, ApJ, 857, 126
Lauer, T. R., Tremaine, S., Richstone, D., & Faber, S. M. 2007, ApJ, 670, 249
Leipski, C., Meisenheimer, K., Walter, F., et al. 2014, ApJ, 785, 154
Li, J., Venemans, B. P., Walter, F., et al. 2022, ApJ, 930, 27
Lira, P., Kaspi, S., Netzer, H., et al. 2018, ApJ, 865, 56
Lodato, G., & Natarajan, P. 2006, MNRAS, 371, 1813
Luo, Y., Shlosman, I., Nagamine, K., & Fang, T. 2020, MNRAS, 492, 4917
Lupi, A., Haardt, F., Dotti, M., et al. 2016, MNRAS, 456, 2993
Lupi, A., Volonteri, M., Decarli, R., et al. 2019, MNRAS, 488, 4004
Lupi, A., Volonteri, M., Decarli, R., Bovino, S., & Silk, J. 2022, MNRAS, 510, 5760
Lynden-Bell, D. 1969, Natur, 223, 690
Madau, P., Haardt, F., & Dotti, M. 2014, ApJL, 784, L38
Madau, P., & Rees, M. J. 2001, ApJL, 551, L27
Maddox, N., Hewett, P. C., Warren, S. J., & Croom, S. M. 2008, MNRAS, 386, 1605
Malmquist, K. G. 1922, MeLuF, 100, 1
Malmquist, K. G. 1925, MeLuF, 106, 1
Marasco, A., Cresci, G., Posti, L., et al. 2021, MNRAS, 507, 4274
Marconi, A., & Hunt, L. K. 2003, ApJL, 589, L21
Marian, V., Jahnke, K., Andika, I., et al. 2020, ApJ, 904, 79
Marian, V., Jahnke, K., Mechtley, M., et al. 2019, ApJ, 882, 141
Marshall, M. A., Mechtley, M., Windhorst, R. A., et al. 2020a, ApJ, 900, 21
Marshall, M. A., Ni, Y., Di Matteo, T., et al. 2020b, MNRAS, 499, 3819
Marshall, M. A., Wyithe, J. S. B., Windhorst, R. A., et al. 2021, MNRAS, 506, 1209
Marziani, P., del Olmo, A., Martínez-Carballo, M. A., et al. 2019, A&A, 627, A88
Marziani, P., & Sulentic, J. W. 2012, NewAR, 56, 49
Matsuoka, Y., Iwasawa, K., Onoue, M., et al. 2022, ApJS, 259, 18
Matsuoka, Y., Onoue, M., Kashikawa, N., et al. 2016, ApJ, 828, 26
Matsuoka, Y., Onoue, M., Kashikawa, N., et al. 2018a, PASJ, 70, S35
Matsuoka, Y., Onoue, M., Kashikawa, N., et al. 2019, ApJL, 872, L2
Matsuoka, Y., Strauss, M. A., Kashikawa, N., et al. 2018b, ApJ, 869, 150
Mayer, L., & Bonoli, S. 2019, RPPh, 82, 016901
Mayer, L., Kazantzidis, S., Escala, A., & Callegari, S. 2010, Natur, 466, 1082
Mazzucchelli, C., Bañados, E., Venemans, B. P., et al. 2017, ApJ, 849, 91
Mazzucchelli, C., Decarli, R., Farina, E. P., et al. 2019, ApJ, 881, 163
McConnell, N. J., & Ma, C.-P. 2013, ApJ, 764, 184
McLure, R. J., & Dunlop, J. S. 2002, MNRAS, 331, 795
McLure, R. J., & Dunlop, J. S. 2004, MNRAS, 352, 1390
Mechtley, M., Jahnke, K., Windhorst, R. A., et al. 2016, ApJ, 830, 156
Mechtley, M., Windhorst, R. A., Ryan, R. E., et al. 2012, ApJL, 756, L38
Medvedev, P., Gilfanov, M., Sazonov, S., Schartel, N., & Sunyaev, R. 2021, MNRAS, 504, 576
Medvedev, P., Sazonov, S., Gilfanov, M., et al. 2020, MNRAS, 497, 1842
Mejía-Restrepo, J. E., Trakhtenbrot, B., Lira, P., & Netzer, H. 2018, MNRAS, 478, 1929
Merloni, A., Bongiorno, A., Bolzonella, M., et al. 2010, ApJ, 708, 137
Meyer, R. A., Bosman, S. E. I., & Ellis, R. S. 2019, MNRAS, 487, 3305
Meyer, R. A., Decarli, R., Walter, F., et al. 2022b, ApJ, 927, 141
Meyer, R. A., Walter, F., Cicone, C., et al. 2022a, ApJ, 927, 152
Moehler, S., Modigliani, A., Freudling, W., et al. 2014, A&A, 568, A9
Moretti, A., Ballo, L., Braito, V., et al. 2014, A&A, 563, A46
Morey, K. A., Eilers, A.-C., Davies, F. B., Hennawi, J. F., & Simcoe, R. A. 2021, ApJ, 921, 88
Mori, M., Ferrara, A., & Madau, P. 2002, ApJ, 571, 40
Mortlock, D. J., Patel, M., Warren, S. J., et al. 2009, A&A, 505, 97
Mortlock, D. J., Warren, S. J., Venemans, B. P., et al. 2011, Natur, 474, 616
Nanni, R., Gilli, R., Vignali, C., et al. 2018, A&A, 614, A121
Nanni, R., Vignali, C., Gilli, R., Moretti, A., & Brandt, W. N. 2017, A&A, 603, A128
Narayan, R., & Yi, I. 1995, ApJ, 452, 710
Neeleman, M., Bañados, E., Walter, F., et al. 2019, ApJ, 882, 10
Neeleman, M., Novak, M., Venemans, B. P., et al. 2021, ApJ, 911, 141
Novak, M., Bañados, E., Decarli, R., et al. 2019, ApJ, 881, 63
Novak, M., Venemans, B. P., Walter, F., et al. 2020, ApJ, 904, 131
Oh, S. P., & Haiman, Z. 2002, ApJ, 569, 558
Oke, J. B. 1974, ApJS, 27, 21
Oke, J. B., & Gunn, J. E. 1983, ApJ, 266, 713
Onoue, M., Bañados, E., Mazzucchelli, C., et al. 2020, ApJ, 898, 105
Onoue, M., Kashikawa, N., Matsuoka, Y., et al. 2019, ApJ, 880, 77
Onoue, M., Matsuoka, Y., Kashikawa, N., et al. 2021, ApJ, 919, 61
Pacucci, F., Natarajan, P., Volonteri, M., Cappelluti, N., & Urry, C. M. 2017, ApJL, 850, L42
Page, M. J., Simpson, C., Mortlock, D. J., et al. 2014, MNRAS, 440, L91
Pâris, I., Petitjean, P., Aubourg, É., et al. 2018, A&A, 613, A51
Pelupessy, F. I., Di Matteo, T., & Ciardi, B. 2007, ApJ, 665, 107
Peng, C. Y., Impey, C. D., Rix, H.-W., et al. 2006, ApJ, 649, 616

Pensabene, A., Carniani, S., Perna, M., et al. 2020, A&A, 637, A84
Pensabene, A., Decarli, R., Bañados, E., et al. 2021, A&A, 652, A66
Pensabene, A., van der Werf, P., Decarli, R., et al. 2022, A&A, 667, A9
Perez, F., & Granger, B. E. 2007, CSE, 9, 21
Peterson, B. M., Ferrarese, L., Gilbert, K. M., et al. 2004, ApJ, 613, 682
Planck Collaboration, Aghanim, N., Akrami, Y., et al. 2020, A&A, 641, A1
Pons, E., McMahon, R. G., Banerji, M., & Reed, S. L. 2020, MNRAS, 491, 3884
Pons, E., McMahon, R. G., Simcoe, R. A., et al. 2019, MNRAS, 484, 5142
Portegies Zwart, S. F., Baumgardt, H., Hut, P., Makino, J., & McMillan, S. L. W. 2004, Natur, 428, 724
Portegies Zwart, S. F., & McMillan, S. L. W. 2002, ApJ, 576, 899
Prochaska, J. X., Hennawi, J., Cooke, R., et al. 2019a, PypeIt: Python spectroscopic data reduction pipeline, Astrophysics Source Code Library, ascl:1911.004
Prochaska, J. X., Hennawi, J., Cooke, R., et al. 2019b, pypeit/PypeIt: Releasing for DOI, v0.11.0.1, Zenodo, doi:10.5281/zenodo.3506873
Prochaska, J. X., & Hennawi, J. F. 2009, ApJ, 690, 1558
Prochaska, J. X., Hennawi, J. F., Westfall, K. B., et al. 2020, JOSS, 5, 2308
Reed, S. L., Banerji, M., Becker, G. D., et al. 2019, MNRAS, 487, 1874
Regan, J. A., Visbal, E., Wise, J. H., et al. 2017, NatAs, 1, 0075
Reynolds, C. S. 2014, SSRv, 183, 277
Reynolds, C. S. 2021, ARA&A, 59, 117
Richards, G. T., Kruczek, N. E., Gallagher, S. C., et al. 2011, AJ, 141, 167
Richards, G. T., Lacy, M., Storrie-Lombardi, L. J., et al. 2006a, ApJS, 166, 470
Richards, G. T., Strauss, M. A., Fan, X., et al. 2006b, AJ, 131, 2766
Richards, G. T., Vanden Berk, D. E., Reichard, T. A., et al. 2002, AJ, 124, 1
Richstone, D., Ajhar, E. A., Bender, R., et al. 1998, Natur, 385, A14
Risaliti, G., Young, M., & Elvis, M. 2009, ApJL, 700, L6
Rojas-Ruiz, S., Bañados, E., Neeleman, M., et al. 2021, ApJ, 920, 150
Rousselot, P., Lidman, C., Cuby, J. G., Moreels, G., & Monnet, G. 2000, A&A, 354, 1134
Runnoe, J. C., Brotherton, M. S., & Shang, Z. 2012, MNRAS, 422, 478
Sabra, B. M., Saliba, C., Abi Akl, M., & Chahine, G. 2015, ApJ, 803, 5
Salpeter, E. E. 1964, ApJ, 140, 796
Sassano, F., Schneider, R., Valiante, R., et al. 2021, MNRAS, 506, 613
Savorgnan, G. A. D., Graham, A. W., Marconi, A., & Sani, E. 2016, ApJ, 817, 21
Schindler, J.-T. 2022, Sculptor: Interactive modeling of astronomical spectra, Astrophysics Source Code Library, ascl:2202.018
Schindler, J.-T., Fan, X., McGreer, I. D., et al. 2017, ApJ, 851, 13
Schindler, J.-T., Fan, X., McGreer, I. D., et al. 2018, ApJ, 863, 144
Schindler, J.-T., Fan, X., McGreer, I. D., et al. 2019, ApJ, 871, 258
Schindler, J.-T., Farina, E. P., Bañados, E., et al. 2020, ApJ, 905, 51
Schmidt, M. 1963, Natur, 197, 1040
Schulze, A., & Wisotzki, L. 2011, A&A, 535, A87
Schulze, A., & Wisotzki, L. 2014, MNRAS, 438, 3422
Shakura, N. I., & Sunyaev, R. A. 1973, A&A, 500, 33
Shankar, F., Crocce, M., Miralda-Escudé, J., Fosalba, P., & Weinberg, D. H. 2010, ApJ, 718, 231
Shankar, F., Weinberg, D. H., & Miralda-Escudé, J. 2009, ApJ, 690, 20
Shao, Y., Wang, R., Carilli, C. L., et al. 2019, ApJ, 876, 99
Shemmer, O., Brandt, W. N., Netzer, H., Maiolino, R., & Kaspi, S. 2008, ApJ, 682, 81
Shen, X., Hopkins, P. F., Faucher-Giguère, C.-A., et al. 2020, MNRAS, 495, 3252
Shen, Y. 2013, BASI, 41, 61
Shen, Y., Greene, J. E., Ho, L. C., et al. 2015, ApJ, 805, 96
Shen, Y., & Liu, X. 2012, ApJ, 753, 125
Shen, Y., Richards, G. T., Strauss, M. A., et al. 2011, ApJS, 194, 45
Shen, Y., Strauss, M. A., Oguri, M., et al. 2007, AJ, 133, 2222
Shen, Y., Wu, J., Jiang, L., et al. 2019, ApJ, 873, 35
Shimasaku, K., & Izumi, T. 2019, ApJL, 872, L29
Silk, J., & Rees, M. J. 1998, A&A, 331, L1
Sądowski, A. 2009, ApJS, 183, 171
Sądowski, A. 2011, PhD thesis, Polish Academy of Sciences
Sądowski, A., Narayan, R., McKinney, J. C., & Tchekhovskoy, A. 2014, MNRAS, 439, 503
Smirnov, N. V. 1948, The Annals of Mathematical Statistics, 19, 279
Snyder, G. F., Lotz, J. M., Rodriguez-Gomez, V., et al. 2017, MNRAS, 468, 207
Solanes, J. M., Perea, J. D., & Valentí-Rojas, G. 2018, A&A, 614, A66
Soltan, A. 1982, MNRAS, 200, 115
Student 1908, Biometrika, 6, 1
Suh, H., Civano, F., Trakhtenbrot, B., et al. 2020, ApJ, 889, 32
Sun, A.-L., Greene, J. E., Impellizzeri, C. M. V., et al. 2013, ApJ, 778, 47
Sun, M., Trump, J. R., Shen, Y., et al. 2015, ApJ, 811, 42
Svensson, R., & Zdziarski, A. A. 1994, ApJ, 436, 599
Tanaka, T., & Haiman, Z. 2009, ApJ, 696, 1798
Targett, T. A., Dunlop, J. S., & McLure, R. J. 2012, MNRAS, 420, 3621
Tenneti, A., Di Matteo, T., Croft, R., Garcia, T., & Feng, Y. 2018, MNRAS, 474, 597
Thorne, K. S. 1974, ApJ, 191, 507
Tormen, G., Bouchet, F. R., & White, S. D. M. 1997, MNRAS, 286, 865
Trakhtenbrot, B. 2021, in IAU Conf. Proc. 356, Nuclear Activity in Galaxies Across Cosmic Time, ed. M. Pović et al. (Cambridge: Cambridge Univ. Press), 261
Trakhtenbrot, B., & Netzer, H. 2012, MNRAS, 427, 3081
Trakhtenbrot, B., Netzer, H., Lira, P., & Shemmer, O. 2011, ApJ, 730, 7
Trakhtenbrot, B., Ricci, C., Koss, M. J., et al. 2017b, MNRAS, 470, 800
Trakhtenbrot, B., Urry, C. M., Civano, F., et al. 2015, Sci, 349, 168
Trakhtenbrot, B., Volonteri, M., & Natarajan, P. 2017a, ApJL, 836, L1
Trebitsch, M., Volonteri, M., & Dubois, Y. 2019, MNRAS, 487, 819
Tremaine, S., Gebhardt, K., Bender, R., et al. 2002, ApJ, 574, 740
Tsuzuki, Y., Kawara, K., Yoshii, Y., et al. 2006, ApJ, 650, 57
van der Walt, S., Colbert, S. C., & Varoquaux, G. 2011, CSE, 13, 22
van Dokkum, P. G. 2001, PASP, 113, 1420
van Rossum, G., & Drake, F. L. 1995, Python Tutorial (Amsterdam: Centrum voor Wiskunde en Informatica Amsterdam)
van Rossum, G., & Drake, F. L. 2009, Python 3 Reference Manual (Scotts Valley, CA: CreateSpace)
Vanden Berk, D. E., Richards, G. T., Bauer, A., et al. 2001, AJ, 122, 549
Venemans, B. P., Bañados, E., Decarli, R., et al. 2015, ApJL, 801, L11
Venemans, B. P., Decarli, R., Walter, F., et al. 2018, ApJ, 866, 159
Venemans, B. P., Findlay, J. R., Sutherland, W. J., et al. 2013, ApJ, 779, 24
Venemans, B. P., McMahon, R. G., Warren, S. J., et al. 2007, MNRAS, 376, L76
Venemans, B. P., Neeleman, M., Walter, F., et al. 2019, ApJL, 874, L30
Venemans, B. P., Walter, F., Decarli, R., et al. 2017a, ApJ, 845, 154
Venemans, B. P., Walter, F., Decarli, R., et al. 2017b, ApJ, 837, 146
Venemans, B. P., Walter, F., Neeleman, M., et al. 2020, ApJ, 904, 130
Venemans, B. P., Walter, F., Zschaechner, L., et al. 2016, ApJ, 816, 37
Vernet, J., Dekker, H., D'Odorico, S., et al. 2011, A&A, 536, A105
Vestergaard, M., & Osmer, P. S. 2009, ApJ, 699, 800
Vestergaard, M., & Peterson, B. M. 2006, ApJ, 641, 689
Vestergaard, M., & Wilkes, B. J. 2001, ApJS, 134, 1
Virtanen, P., Gommers, R., Oliphant, T. E., et al. 2020, NatMe, 17, 261
Visbal, E., Haiman, Z., & Bryan, G. L. 2014, MNRAS, 445, 1056
Vito, F., Brandt, W. N., Bauer, F. E., et al. 2019, A&A, 630, A118
Volonteri, M. 2010, A&ARv, 18, 279
Volonteri, M. 2012, Sci, 337, 544
Volonteri, M., Haardt, F., & Madau, P. 2003, ApJ, 582, 559
Volonteri, M., Natarajan, P., & Gültekin, K. 2011, ApJ, 737, 50
Volonteri, M., & Rees, M. J. 2005, ApJ, 633, 624
Wagenveld, J. D., Saxena, A., Duncan, K. J., Röttgering, H. J. A., & Zhang, M. 2022, A&A, 660, A22
Walter, F., Bertoldi, F., Carilli, C., et al. 2003, Natur, 424, 406
Walter, F., Carilli, C., Bertoldi, F., et al. 2004, ApJL, 615, L17
Walter, F., Carilli, C., Neeleman, M., et al. 2020, ApJ, 902, 111
Walter, F., Neeleman, M., Decarli, R., et al. 2022, ApJ, 927, 21
Walter, F., Riechers, D., Novak, M., et al. 2018, ApJL, 869, L22
Wang, F., Davies, F. B., Yang, J., et al. 2020a, ApJ, 896, 23
Wang, F., Fan, X., Yang, J., et al. 2017, ApJ, 839, 27
Wang, F., Wang, R., Fan, X., et al. 2019a, ApJ, 880, 2
Wang, F., Wu, X.-B., Fan, X., et al. 2016a, ApJ, 819, 24
Wang, F., Yang, J., Fan, X., et al. 2019b, ApJ, 884, 30
Wang, F., Yang, J., Fan, X., et al. 2021a, ApJL, 907, L1
Wang, R., Shao, Y., Carilli, C. L., et al. 2019c, ApJ, 887, 40
Wang, R., Wagg, J., Carilli, C. L., et al. 2011a, ApJL, 739, L34
Wang, R., Wagg, J., Carilli, C. L., et al. 2011b, AJ, 142, 101
Wang, R., Wagg, J., Carilli, C. L., et al. 2013, ApJ, 773, 44
Wang, R., Wu, X.-B., Neri, R., et al. 2016b, ApJ, 830, 53
Wang, S., Jiang, L., Shen, Y., et al. 2021b, ApJ, 925, 121
Wang, S., Shen, Y., Jiang, L., et al. 2020b, ApJ, 903, 51
Watarai, K.-y., Fukue, J., Takeuchi, M., & Mineshige, S. 2000, PASJ, 52, 133
Wenzl, L., Schindler, J.-T., Fan, X., et al. 2021, AJ, 162, 72
White, M., Martini, P., & Cohn, J. D. 2008, MNRAS, 390, 1179
Willott, C. J., Albert, L., Arzoumanian, D., et al. 2010b, AJ, 140, 546
Willott, C. J., Bergeron, J., & Omont, A. 2015, ApJ, 801, 123
Willott, C. J., Bergeron, J., & Omont, A. 2017, ApJ, 850, 108
Willott, C. J., Delorme, P., Omont, A., et al. 2007, AJ, 134, 2435

Willott, C. J., Delorme, P., Reylé, C., et al. 2010a, AJ, 139, 906
Willott, C. J., Omont, A., & Bergeron, J. 2013, ApJ, 770, 13
Woo, J.-H. 2008, AJ, 135, 1849
Woo, J.-H., Le, H. A. N., Karouzos, M., et al. 2018, ApJ, 859, 138
Woods, T. E., Agarwal, B., Bromm, V., et al. 2019, PASA, 36, e027
Worseck, G., Khrykin, I. S., Hennawi, J. F., Prochaska, J. X., & Farina, E. P. 2021, MNRAS, 505, 5084
Worseck, G., & Prochaska, J. X. 2011, ApJ, 728, 23
Wu, X.-B., Wang, F., Fan, X., et al. 2015, Natur, 518, 512
Yang, J., Venemans, B., Wang, F., et al. 2019b, ApJ, 880, 153
Yang, J., Wang, F., Fan, X., et al. 2019a, AJ, 157, 236
Yang, J., Wang, F., Fan, X., et al. 2020, ApJL, 897, L14
Yang, J., Wang, F., Fan, X., et al. 2021, ApJ, 923, 262
York, D. G., Adelman, J., Anderson, J. E. J., et al. 2000, AJ, 120, 1579
Zel'dovich, Y. B., & Novikov, I. D. 1964, SPhD, 9, 246
Zuo, W., Wu, X.-B., Fan, X., et al. 2020, ApJ, 896, 40